MICROCOPY RESOLUTION TEST CHART

JPY

②

AFOSR·TR· 8 7 - 0 7 6 8

Final Technical Report

Grant No. AFOSR-81-0170

FEASIBILITY STUDIES OF OPTICAL PROCESSING

OF IMAGE BANDWIDTH COMPRESSION SCHEMES

Submitted to:

Approved for public release;
distribution unlimited.

Air Force Office of Scientific Research
Bolling Air Force Base
Washington, D.C. 20332-6448

DTIC
ELECTE
JUN 1 5 1987
D

Submitted by:

B. R. Hunt
Department of Electrical and Computer
Engineering
University of Arizona
Tucson, Arizona 85721

May 15, 1987

REPORT DOCUMENTATION PAGE

1a. REPORT SECURITY CLASSIFICATION Unclassified		1b. RESTRICTIVE MARKINGS	
2a. SECURITY CLASSIFICATION AUTHORITY		3. DISTRIBUTION / AVAILABILITY OF REPORT Unlimited	
2b. DECLASSIFICATION / DOWNGRADING SCHEDULE			
4. PERFORMING ORGANIZATION REPORT NUMBER(S)		5. MONITORING ORGANIZATION REPORT NUMBER(S) AFOSR·TR· 87 - 0768	
6a. NAME OF PERFORMING ORGANIZATION Dept. Electrical & Computer Eng. College of Engineering & Mines	6b. OFFICE SYMBOL (If applicable)	7a. NAME OF MONITORING ORGANIZATION AFOSR	
6c. ADDRESS (City, State, and ZIP Code) University of Arizona Tucson, Arizona 85721		7b. ADDRESS (City, State, and ZIP Code) Bldg 410 Bolling AFB DC 20332-6448	
8a. NAME OF FUNDING / SPONSORING ORGANIZATION AFOSR, Bolling AFB	8b. OFFICE SYMBOL (If applicable) NE	9. PROCUREMENT INSTRUMENT IDENTIFICATION NUMBER AFOSR·81-0170	
8c. ADDRESS (City, State, and ZIP Code) Bolling Air Force Base Washington, D. C. 20332-6448		10. SOURCE OF FUNDING NUMBERS	

	10. SOURCE OF FUNDING NUMBERS		
PROGRAM ELEMENT NO 61102F	PROJECT NO 2305	TASK NO B1	WORK UNIT ACCESSION NO

11. TITLE (Include Security Classification)

Feasibility Studies of Optical Processing of Image Bandwidth Compression Schemes

12. PERSONAL AUTHOR(S)
B. R. Hunt

13a. TYPE OF REPORT Final	13b. TIME COVERED FROM 3/15/81 TO 9/30/85	14. DATE OF REPORT (Year, Month, Day) May 15, 1987	15. PAGE COUNT 203

16. SUPPLEMENTARY NOTATION

17.	COSATI CODES		18. SUBJECT TERMS (Continue on reverse if necessary and identify by block number)
FIELD	GROUP	SUB-GROUP	

19. ABSTRACT (Continue on reverse if necessary and identify by block number)

One portion of this work involves further development of the interpulated differential pulse code modulation Rescursive(IDPCM) image data compression method. The goal of this work is to make the Recursive-IDPCM more efficient without increasing the coding complexity by adaptive schemes.

The details of adaptive schemes are discussed. Several algoriths of subimage activity classification are proposed and evaluated. Optimum quantizers are designed according to data sources to minimize quanitization error. Difference datat are quantized adaptively based on the objective measure of subimage activity at each recursion. The result of the computer simulation demonstrates a high compression ration with a good subjective reconstructed image fidelity without drastically increasing computation time overthat required for Recursive-IDPCM has been achieved.

Another portion pertains to using a shift-and-add algorithm to lesson the effect of atmospheric distortion. It is shown theoretically that shift-and-add processing may preserve diffraction-limited information in the resulting image, both in the point

20. DISTRIBUTION / AVAILABILITY OF ABSTRACT ☐ UNCLASSIFIED/UNLIMITED ☒ SAME AS RPT. ☐ DTIC USERS	21. ABSTRACT SECURITY CLASSIFICATION UNCLASSIFIED	
22a. NAME OF RESPONSIBLE INDIVIDUAL LTC CARTER	22b. TELEPHONE (Include Area Code) (202) 767-4933	22c. OFFICE SYMBOL NE

source and extended object cases, and the probability of ghost peaks in the cases of an object consisting of two point sources is discussed. Also, a convergence rate for the shift-and-add algorithm is established and simulation results are presented.

ARIDPCM

3

ADAPTIVE DIGITAL IMAGE DATA COMPRESSION

BY RECURSIVE IDPCM

by

Deng Yuan Fu

A Thesis Submitted to the Faculty of the

DEPARTMENT OF ELECTRICAL AND COMPUTER ENGINEERING

In Partial Fulfillment of the Requirements
For the Degree of

MASTER OF SCIENCE
WITH A MAJOR IN ELECTRICAL ENGINEERING

In the Graduate College

THE UNIVERSITY OF ARIZONA

1 9 8 5

STATEMENT BY AUTHOR

This thesis has been submitted in partial fulfillment of requirements for an advanced degree at The University of Arizona and is deposited in the University of Arizona to be made available to borrowers under rules of the Library.

Brief quotations from this thesis are allowable without special permission, provided that accurate acknowledgment of source is made. Requests for permission for extended quotation from or reproduction of this manuscript in whole or in part may be granted by the head of the major department or the Dean of the Graduate College when in his or her judgment the proposed use of the material is in the interests of scholarship. In all other instances, however, permission must be obtained from the author.

SIGNED: _Deng Yuan Fu_

APPROVAL BY THESIS DIRECTOR

This thesis has been approved on the date shown below:

B. R. HUNT	Date
Professor of Electrical and Computer Engineering	

ACKNOWLEDGMENTS

TABLE OF CONTENTS

LIST OF ILLUSTRATIONS

LIST OF ILLUSTRATIONS -- <u>Continued</u>

LIST OF ILLUSTRATIONS -- <u>Continued</u>

LIST OF TABLES

ABSTRACT

This work involves further development of the Recursive-IDPCM image data compression method. The goal of this work is to make the Recursive-IDPCM more efficient without increasing the coding complexity by adaptive schemes.

The details of adaptive schemes are discussed. Several algorithms of subimage activity classification are proposed and evaluated. Optimum quantizers are designed according to data sources to minimize quantization error. Difference data are quantized adaptively based on the objective measure of subimage activity at each recursion. The result of the computer simulation demonstrates a high compression ratio with a good subjective reconstructed image fidelity without drastically increasing computation time over that required for Recursive-IDPCM has been achieved.

CHAPTER 1

INTRODUCTION

With the continuing growth of modern communication technology, the demand for image transmission and storage is increasing rapidly. Limitations on bandwidth for transmitting image data over digital communication channels have led researchers to look for efficient and feasible methods to compress image data under a given amount of distortion. Before discussing various data compression algorithms, it is necessary to examine how image data can be compressed.

The key point is that a large amount of redundancy exists in a uniformly sampled image. This redundancy can be explored both in the frequency and spatial domain. Removing, or at least reducing the redundant information from the original image, is the goal of data compression. Figure 1 contains the cosine transform of a 32 by 32 image. It can be seen that the energy in the transform domain tends to be clustered into a relatively small number of transform samples in the low-frequency region. To achieve data compression, transform samples of low magnitude can be discarded, or coarsely quantized in a digital transmission

1

INTRODUCTION

This is the final report for the Grant Year 1984-1985 on Grant Number AFOSR-81-0170. During this year two pieces of research were concluded under sponsorship of the Grant. The two research activities are included as two separate divisions of this research report. The research activities are as follows:

1. Adaptive Recursive Interpolated DPCM for image data compression (ARIDPCM). A consistent theme in the research supported under Grant Number AFOSR under Grant AFOSR-81-0170 has been novel methods of image data compression that are suitable for implementation by optical processing. Initial investigations led to the IDPCM method of image data compression. Subsequent modifications to the IDPCM algorithm were investigated, and led to the improvement of the algorithm for both image quality and decreased bit rate. The ARIDPCM version of the algorithm is the most powerful form yet developed. The ARIDPCM algorithm was fully demonstrated in a M.Sc. thesis by Mr. Eng Yuan Fu. This thesis is included as the section of this report entitled "ARIDPCM."

2. Deblurring images through turbulent atmosphere. A common problem in astronomy is the imaging of astronomical objects through the turbulence caused by microscale fluctuations of the atmosphere. The microscale fluctuations limit the resolution of any object by ground-based telescope, the phenomenon of stars "twinkling" being the most commonly

1

observed form of this degradation. This problem also has military significance in limiting the ground-based observation of satellites in earth orbit. As concerns about SDI arise, the observation of Soviet satellites becomes more important, and this observation is limited by atmospheric turbulence. Research has been conducted under Grant Number AFOSR-81-0170 to study the ability to use techniques such as optical and digital computation in removing the blur from astronomical images caused by turbulence. This research culminated in a Ph.D. thesis by Dr. Karen West. This thesis is included as the section of this report entitled "Correcting Images for Atmospheric Turbulence."

TECHNOLOGY TRANSFER

We are pleased to report that the work sponsored as ARIDPCM has had immediate transfer to a major government activity. The ARIDPCM method has been utilized in a prototype system built by a contractor for a special study. The success of this prototype has led to the designation of ARIDPCM as a standard format for a special system. This special system, the contractor, the sponsorship, and all details of the study are classified, and Special Access Requirements apply to the detailed information. However, AFOSR sponsorship of Grant Number AFOSR-81-0170 are essential to the successful transfer of this research into a problem of national significance and need.
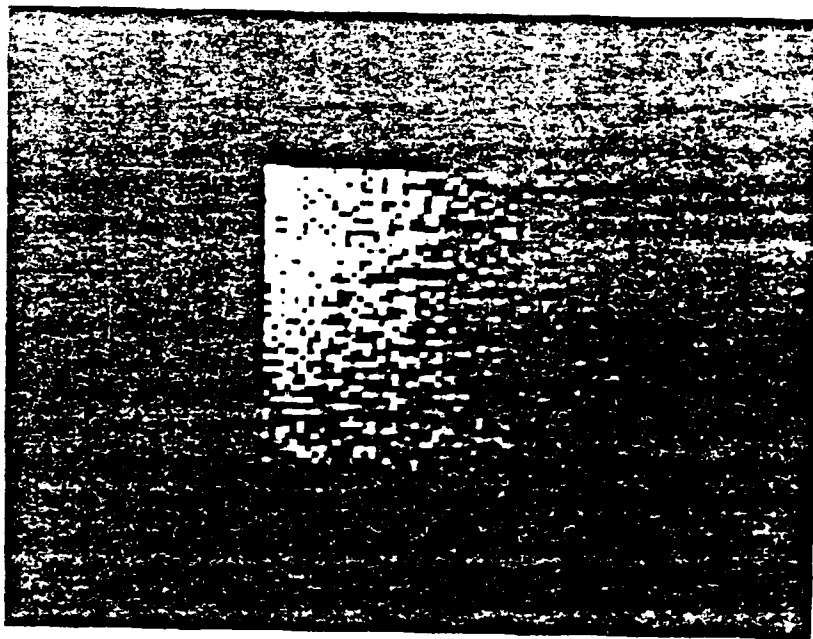
Figure 1.   Cosine transform logarithm magnitude display of 32 x 32 girl image, 32 x 32 coefficients.

Figure 2.   32 x 32 Girl image.

system, without serious loss of resolution. In the spatial domain, a large number of pixels possesses low inter-pixel variance, or equivalently, they are said to be highly correlated. As a result, the adjacent-sample difference has a much smaller variance than the original signal. This fact is exploited in redundancy-removal for image data.

1.1 Concepts of Data Compression

We recall the definition of an image element or pixel, a digital image gray level $P(i,j)$ which has been discretized both in spatial coordinates and in intensity. Thus the image may be considered as a matrix whose row and column index is a point in the image and the corresponding matrix element value identifies the gray level at that point, i.e., the pixel value.

Two related concepts necessary to the understanding of this thesis are the bit-rate and the compression ratio. A basic problem in image data compression is to achieve the minimum possible distortion for a given compression rate, or equivalently, to achieve a given acceptable level of distortion with the least possible compression rate. The compression is characterized by bit rate, and it is specified as the number of bits per pixel, BPP. Then the compression ratio is defined as

$$R = \frac{\text{Average bit rate of the original image data}}{\text{Average bit rate of the compressed data}}$$

(1)

It is further necessary to define an objective and a subjective image fidelity measure.

The distortion can be specified either by an objective measure as the root-mean-square error, RMSE, or by a subjective measure such as the mean opinion score, which is given by human observers [1]. The RMSE is used as an objective measure of the performance of data compression methods in this thesis, and it is defined as

$$RMSE = \sqrt{\sum_{i=1}^{N} \sum_{j=1}^{N} \frac{(P_{ij} - \hat{P}_{ij})^2}{P_{ij}^2}}$$

(2)

where P_{ij} is the original pixel, $\hat{P}_{ij}$ is the reconstructed pixel, and N is an original square image size.

1.2 IDPCM and Its Variants

As mentioned above, many successful methods of data compression have been developed both in the transform and the spatial domains in recent years [2]. Among data compression techniques in the spatial domain, extensive efforts have been concentrated on the Differential Pulse Code Modulation (DPCM) system [3]. The DPCM method is particularly attractive because of its simple design and its rapid speed of operation, which has made its use in real-time data compression of television signals possible.

5

But its major drawbacks have been also pointed out in [4]: (1) it is sensitive to variances in image statistics, (2) it is highly sensitive to channel error, and (3) it becomes complex to implement when other models are used such as two-dimensional autoregressive moving average models, and other stochastic models.

In 1977 the Interpolated Differential Pulse Code Modulation IDPCM data compression method was proposed by Hunt [5] as a further development of the DPCM method. Although there are some similarities between the two methods, IDPCM is different in two major ways: 1. it is non-causal, and 2. a low-frequency version of the original image is obtained by an interpolation operation, which will be introduced in the following section. Since then, the IDPCM method has been further improved. One is a modified IDPCM algorithm called Recursive-IDPCM [6], and another is the Adaptive Recursive-IDPCM, which will be explained in the following sections.

A high data compression ratio and a low RMSE have been obtained by the Recursive-IDPCM method. However, in real world images the statistical properties of image data vary from one to another, and even within a single image, some regions may not be redundant (and therefore not compressible), and other regions may be very redundant. It is desirable to perform data compression by perfectly

matching the activity of the data source. This naturally leads to the development of an adaptive Recursive-IDPCM method. To apply an adaptive scheme, several problems have to be solved. A suitable measure of image activity must be obtained, adaptive quantization must be achieved, and the image must be optimally partitioned. The approaches to solving the above problems are examined in this thesis, and once they are solved, the goal of the Adaptive Recursive-IDPCM data compression method is to achieve a high compression ratio with a good subjective reconstructed image fidelity without drastically increasing computation time over that required for Recursive IDPCM.

CHAPTER 2

INTERPOLATED DPCM AND RECURSIVE
INTERPOLATED-DPCM

Before discussing the Adaptive Recursive-IDPCM
method, it is necessary to introduce the IDPCM and the
Recursive IDPCM methods.

2.1 IDPCM

The IDPCM data compression method was developed by
Hunt, as an optical analogy to DPCM. The IDPCM has some
similarity to DPCM, but rather than being based on
prediction of future pixel values, it uses interpolation.
The basic idea of IDPCM is to interpolate a subsampled image
in order to generate a low-frequency version image of the
original, and to quantize the difference between low- and
high-frequency information in a smaller number of bits than
the bits required for quantizing the entire pixel value.
For example, if we subsample an image by skipping 8 pixels
in vertical and horizontal directions, the low-frequency
version image in Figure 3 only requires 1.6% of the bits in
its original image. For the difference image in Figure 4,
its histogram depicted in Figure 5 shows that most of the
difference values are distributed in a very narrow region

7

Figure 3. Low-frequency version of the original image.

Figure 4. The difference image between the low-frequency version and the original. -- All values are offset by 128 for display.
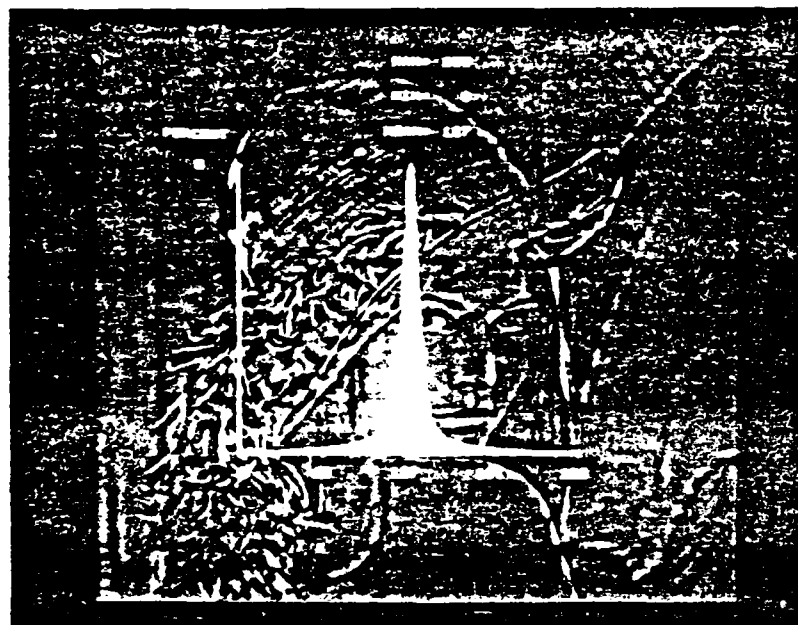
Figure 5. The histogram of difference image which is offset
by 128 for display.

around the origin. These difference values can thus be
quantized in a smaller number of bits to achieve data
compression.

In the IDPCM method [5], the low-frequency version
of the original image is obtained by the convolution

$$\hat{P}_{ij} = \sum_{rs} \bar{P}(r,s)h[(i-r),(j-s)] \qquad (3)$$

where h is the point-spread-function of the interpolator.
The image $\bar{P}$ is constructed from the subsampled image by
inserting zeroes in place of the missing samples to make the
image N x N. The difference image between low- and
high-frequency $d(i,j) = P(i,j) - \hat{P}(i,j)$ is then quantized.
The properties of $\hat{P}$ depend on the interpolation function, h.

The interpolative representation based on
minimization of the ensemble mean square interpolation error
was derived by Jain [14]. However, this minimization is
only for stationary data. For a two-dimensional signal P_{ij},
$i,j = 0,1...N+1$ such that

$$E(P_{ij}) = 0$$

$$E(P_{i+n,j+m}P_{ij}) = \rho^n \rho^m$$

The mean square error ε_{ij} of the interpolated value is
minimized if

$$\varepsilon_{ij} = P_{ij} - \frac{6}{2(1-62)}(U_{i+1,j-1} - U_{i-1,j} - U_{i,j-1} - U_{i,j-1})$$

(5)

It is known that a large number of real world image data does not possess stationarity. Of course some methods of estimating non-stationary data could be employed to optimize the interpolator, but they might not be feasible for a real-time compression system. Therefore, some kind of approximation has to be adopted. In the IDPCM method, the point-spread-function h is approximated by a bilinear interpolator kernel. For example, a 7 x 7 bilinear kernel is illustrated in Figure 6.

The IDPCM operation is described as follows:

1. The original image is subsampled at every fourth line and every fourth pixel, to create a subsampled image. Each subsample is quantized in 3 bits with a uniform quantizer, the maximum and minimum quantization level being the maximum and minimum of the original image.

2. Zeros are inserted into the missing data values in the subsampled image to give an image of the original size. This image is then convolved with a 7 x 7 bilinear interpolator kernel which is described in Figure 6.

3. The interpolated image is subtracted from the original, and the differences are quantized in N_D bits.

1/16	1/8	11/32	1/4	11/32	1/8	1/16
1/8	7/32	7/16	2/4	7/16	7/32	1/8
11/32	7/16	3/8	3/4	3/8	7/16	11/32
1/4	2/4	3/4	1	3/4	2/4	1/4
11/32	7/16	3/8	3/4	3/8	7/16	11/32
1/8	7/32	7/16	2/4	7/16	7/32	1/8
1/16	1/8	11/32	1/4	11/32	1/8	1/16

Figure 6.   7 x 7 Bilinear kernel.

The quantization rule is a tapered quantizer based on the Laplacian probability density [7], which was found to be applicable to the method of IDPCM.

4. The subsamples and the quantized differences are then used to reconstruct the image.

The major attractive features of the IDPCM method are:

1. It is well suited for hardware implementation.

2. It achieves a high data compression ratio.

3. It is less sensitive to channel error than the DPCM system. In the DPCM method, because the prediction is based on the previous values, a channel error will affect not only the current prediction accuracy but also all future prediction accuracy. However, in the IDPCM system, channel error can only affect the accuracy of pixels within an interpolation kernel and usually only one pixel's accuracy because a large amount of the transmitted data is differences.

4. Since the IDPCM is a non-causal operation, it may be operated in parallel.

Since the introduction of this method, several developments to the IDPCM data compression method have been achieved, as discussed below.

2.2 Recursive IDPCM

A significant improvement of IDPCM, called Recursive IDPCM, was achieved by Hunt and Cao [6]. One-dimensional Recursive-IDPCM is drawn in Figure 7 and discussed as follows.

In Figure 7 the pixel values $P(n-2)$ and $P(n+2)$ are subsamples. They are quantized in 6 bits and are used to interpolate the middle point $\bar{c}$. Then the difference between the interpolated value $\bar{c}$ and the original value C, $\bar{c}C$, is quantized to calculate $c'\bar{c}$. The reconstructed middle point value which is the sum of the quantized difference $c'\bar{c}$ and the interpolated value $\bar{c}$ together with subsamples $P(n-2)$ and $P(n+2)$ is used to interpolate the pixel values at points n-1 and n+1, which are b and d. The differences $b'\bar{b}$ and $d'\bar{d}$ are also quantized. The difference $\bar{c}c'$ is defined as the first set of difference, and the $b'\bar{b}$ and $d'\bar{d}$ are the second set of differences. It is obvious that the second set of differences is calculated by the reconstructed value c' and subsamples A and E; therefore, they will be smaller than the first set of difference. This implies that the required number of quantization bits will be reduced.

In the two-dimensional case the low-frequency version of the original image, rather than being obtained by one time convolution, is accomplished by performing the interpolation recursively. The recursive process is:
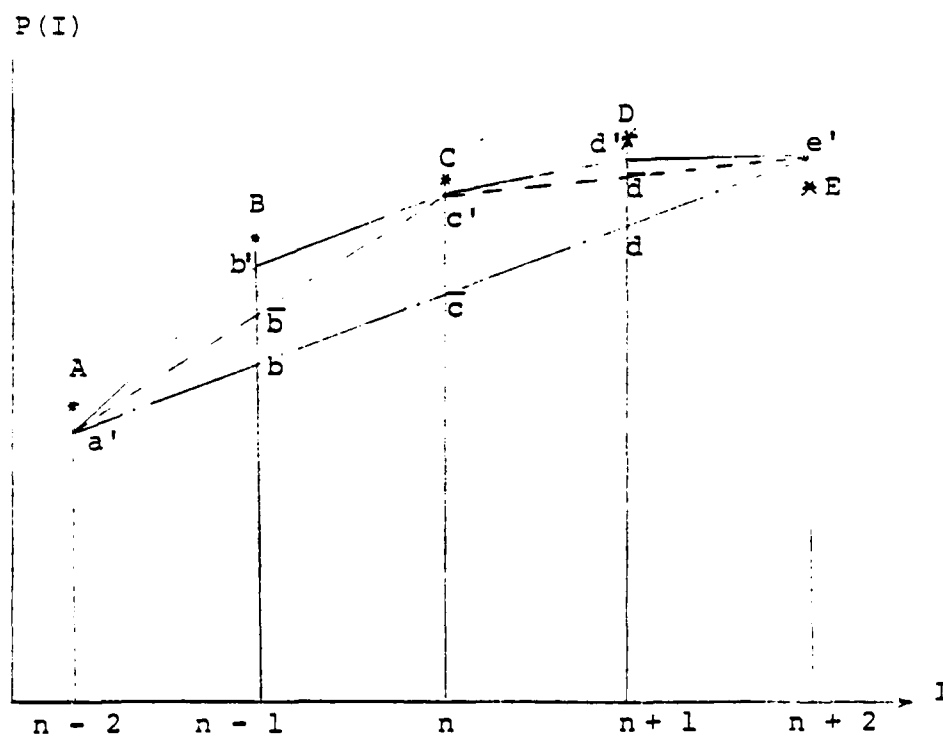
Figure 7.   One-dimensional Recursive-IDPCM.

(1) subsample the original image (e.g., subsample the image skipping 3 pixels both in vertical and horizontal directions) and quantize the subimage at 6 bits (the original image pixel values are quantized in 8 bits, but usually human eyes can only distinguish 32-64 gray levels, 6 bits are sufficient); (2) insert zeros into the subsampled image to double its size and then convolve the obtained image with a 3 x 3 bilinear kernel; (3) subtract the interpolated values from their corresponding original pixel values and quantize this first set of differences (the above process is shown in Figure 8); and (4) the sum of the quantized differences and the interpolated values together with the previous 64 by 64 subsamples form a finer subsample image, 128 by 128. The above process is repeated until reaching the original image size, 512 by 512. During this process, the size of a subsample image increases from 64 x 64, to 128 x 128, to 256 x 256. By the recursive scheme, the subsamples come closer and closer, and the differences between high- and low-frequency versions will become successively smaller. Finally only the first subsample image and all sets of quantized differences need to be transmitted. For low variant data, the second set of differences could be assigned no quantization bits. This omission of the last set and possibly the next to the last set of difference values can save a substantial number of bits.

512 x 512

64 x 64

128 x 128

a.

b.

c.

. pixel
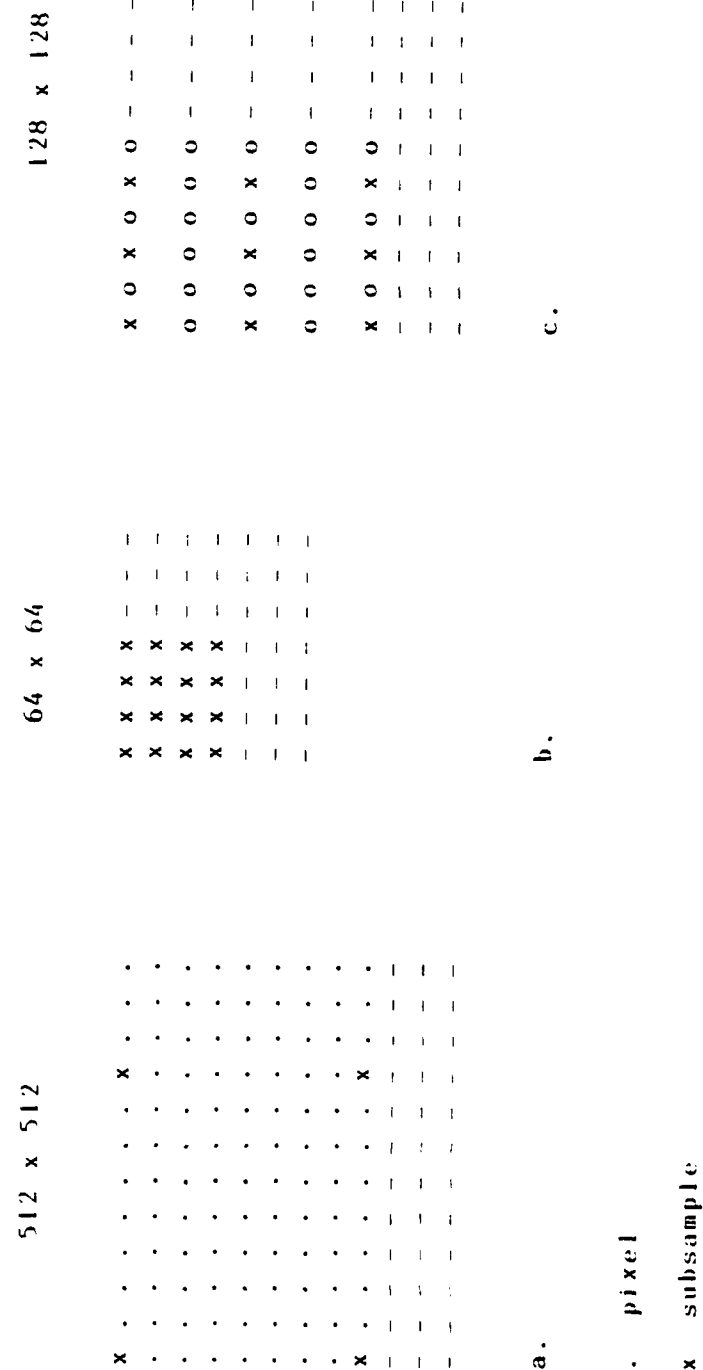
x subsample

Figure 8. Two-dimensional Recursive-IDPCM. -- (a) Original image; (b) Subsample image; and (c) Insert zeros into the subsample image and convolve with a 3 x 3 bilinear kernel.

In principle, the above process can be repeated many times depending on the subsample's density, and every recursion will reduce the interpolated interval by half. Therefore, the recursive process has a property that every recursion can reduce the bit rate. The bit assignment of the Recursive-IDPCM between subsamples are shown in Figure 9. The overall bit requirement for a reconstructed image is

$$\text{Total bits} = 6 \times (N/m)^2 + 3N_{D1}(N/m)^2 + [12(N_{D2})(N/m)^2] \tag{6}$$

where

N = original image size

M = number of pixels by which subsamples are separated

N_{D1} = number of bits for quantizing the first set differences

N_{D2} = number of bits for quantizing the second set differences

RIDPCM is a very efficient data compression method which has achieved a bit rate below 0.4 and mean-square error below 0.2%. Also it is a very simple algorithm to be implemented for a real-time data compression system.

However, this method is used to compress an entire image without regard to the amount of detail in any particular area of an image. A further improvement is to

```
6  0  2  0  3  0  2  0  6        6  0  0  3  0  0  3  0  0  6

0  0  0  0  0  0  0  0  0        0  0  0  0  0  0  0  0  0  0

2  0  2  0  2  0  2  0  2        0  0  0  0  0  0  0  0  0  0

0  0  0  0  0  0  0  0  0        3  0  0  3  0  0  3  0  0  3

3  0  2  0  3  0  2  0  3        0  0  0  0  0  0  0  0  0  0

0  0  0  0  0  0  0  0  0        0  0  0  0  0  0  0  0  0  0

2  0  2  0  2  0  2  0  2        3  0  0  3  0  0  3  0  0  3

0  0  0  0  0  0  0  0  0        0  0  0  0  0  0  0  0  0  0

6  0  2  0  3  0  2  0  6        0  0  0  0  0  0  0  0  0  0

                                 6  0  0  3  0  0  3  0  0  6
```

a.   b.

Figure 9.   Bit assignment for one interpolation kernel. --
            (a) Bit assignment for subsamples skipping 8
            pixels; and (b) Bit assignment for subsamples
            skipping 9 pixels.

make Recursive IDPCM adaptive, which will be presented in the following sections.

CHAPTER 3

ADAPTIVE RECURSIVE-IDPCM METHOD

In most present image data transmission systems, the sampling rate is set on the basis of the fastest expected response from the data source and not on the basis of the quiescent or normal value. The main advantage of an adaptive data compression system is its ability to increase the compression efficiency to a maximum for the specified data with tolerable loss of information. The approach of the adaptive Recursive-IDPCM method is to divide an image into subimages where a high bit rate is required to quantize relatively complex subimages but a low bit rate is sufficient for relatively simple subimages. To match the sampling rate and the quantization level to the subimage data activity or complexity would require an activity classifier. The statistics of each class of subimages is calculated for designing proper quantizers. The subimage classification, the quantizer design, and the subimage size are discussed in the following sections.

3.1 Subimage Classification

Subimages are classified by level of activity. According to human visual acuity, three levels of activity

21

are suggested [8]: high detail, low detail, and average detail. The high detail subimages are defined as neighborhoods of sharp gray-level transitions and low-detail subimages as neighborhoods of smooth gray-level transitions. The subimage activity is measured by statistical image information, and three approaches are proposed. Here, we define high detail as class 1, average detail as class 2, and low detail as class 3.

Subimage Classification by Calculating Sample Variance

Generally, simple descriptions of the waveform are provided by the quantities [9]

$$\mu_x = 1/N \sum_{n=1}^{N} X(n), \quad \sigma_x^2 = 1/(N-1) \sum_{n=1}^{N} (X(n) - \mu_x)^2 \tag{7}$$

called, respectively, the sample mean and sample variance. The quantity σ_x, the square root of the sample variance, is called the standard deviation. For two-dimensional image data, the sample mean and sample variance are defined as

$$\mu_{ij} = (1/n^2) \sum_{k=1}^{n} \sum_{L=1}^{n} P_{i+k, j+1}$$

$$\sigma_{ij}^2 = 1/(n-1)^2 \sum_{K=1}^{n} \sum_{L=1}^{n} (P_{i+k, j+1} - \mu_{ij})^2 \tag{8}$$

where n is the size of square subimages and P is a pixel value. The classification of subimage activity is performed by comparing σ_{ij} with a previously defined thresholds (e.g., T1 = 30, T2 = 15.0, T3 = 0.0)

$$\text{Subimage Activity} \begin{cases} \text{high detail} & T1 \leq \sigma_{ij} \\ \text{average detail} & T2 \leq \sigma_{ij} < T1 \\ \text{low detail} & T3 \leq \sigma_{ij} < T2 \end{cases}$$

Figures 10, 11 and 12 show the results of the classification of subimage activity. By this method, the quantitative measure basically agree with the subjective measure. Most detailed regions such as the girl's eyes, the feather, and sharp edges were classified into class one, and most flat regions, like the background, the girl's shoulder, etc., were classified into class three. But this classification method has the following problems. In some cases there is a wrong classification on sharp edges between dark and bright regions. For example, if we assume that the subimages have the type of patterns in Figure 14, the variances of these subimages are relatively small. In other words, these subimages will be classified into class 2 or class 3. Usually this type of subimages are on sharp edges between dark and bright regions. Figure 15 is the reconstructed image of the Adaptive Recursive-IDPCM, and the subimage classification is based on Equation 8. When this image is
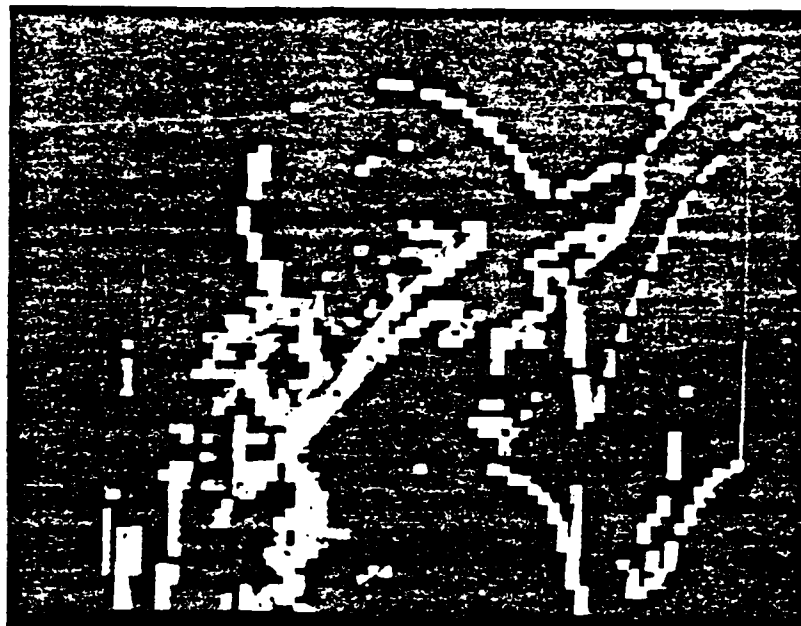
Figure 10. Subimage classification by subimage variance, high detail.
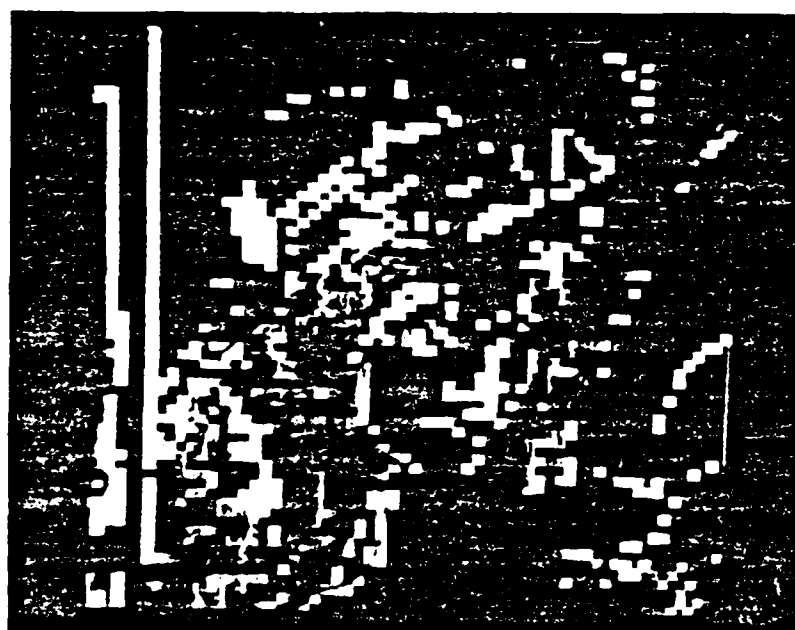
Figure 11. Subimage classification by subimage variance, average detail.

Figure 12. Subimage classification by subimage variance, low detail.

Figure 13. Original image.
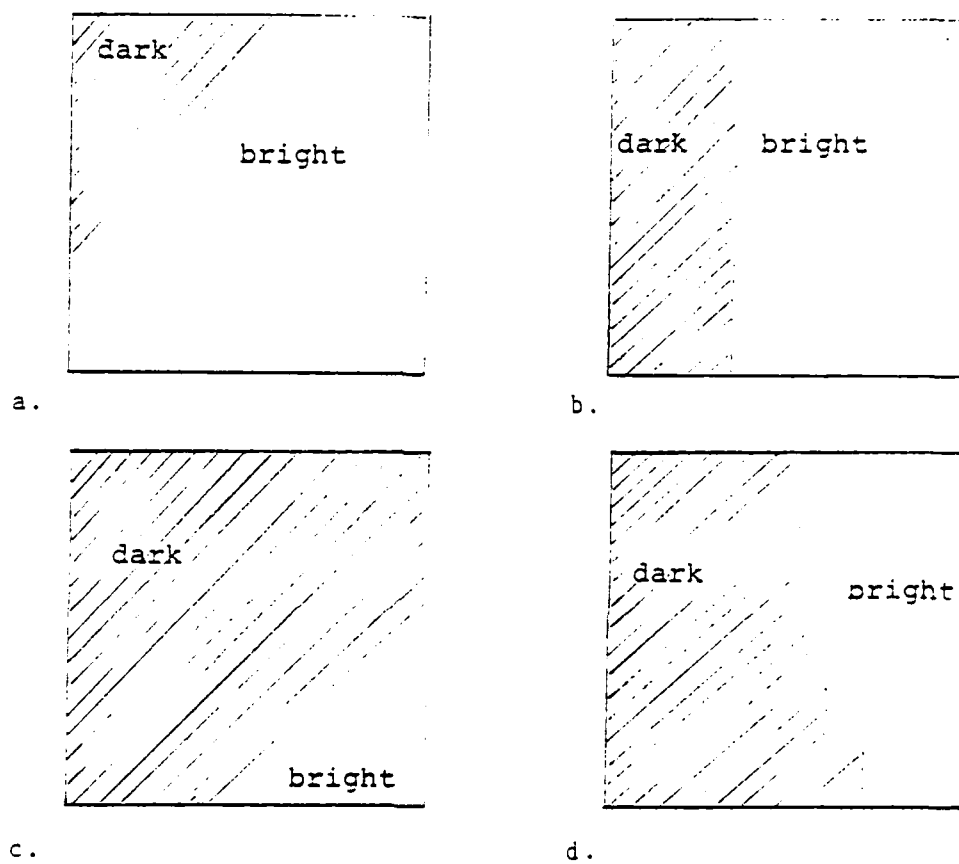
Figure 14. Subimages on sharp edges.

enlarged. Figure 16, we can see that the sharp edge between the girl's shoulder and the dark background was badly reconstructed. This is because the subimages covering this edge were not correctly classified. As a result, insufficient bit rate was assigned to those subimages. Since the distortion along sharp edges is particularly sensitive to human eyes, the above classification is not satisfactory. The second problem is that the calculation of σ_{ij} cannot be done concurrently during the recursive process. This will cost much more machine time than the Recursive IDPCM; therefore, this approach is not desirable for real-time implementation. The third problem is that the information of each subimage activity has to be transmitted to the receiver. This will cost some bits.

Subimage Classification Based on the Variance of Differences

The subimage activity can be associated with the statistical property of the differences between interpolated and original values. This is possible because the interpolation error will be small when neighboring pixels have low variance or will be large when neighboring pixels have large variance. Now define the sample mean and sample variance of difference data as

28

Figure 15.   Adaptive-Recursive-IDPCM, BPP = 0.30106; MSE = 0.01374 (subimage classification according to the variance of subimage pixel values).

Figure 16.   Enlargement of Figure 15.

$$\begin{cases} \mu_{ij} = 1/n^2 \sum_K \sum_L (d_{i+k,j+1}) \\ \\ \alpha^2_{ij} = 1/(n-1)^2 \sum_K \sum_L (kd_{i+k,j+1} - \mu_{ij})^2 \end{cases} \qquad (9)$$

where

$$\begin{cases} k,L \ (0,2,4\ldots n-1) \\ K \neq L = 0 \\ i,j = (1,\ n+1,\ 2n+1\ldots,N+1) \\ n \qquad \text{subimage size} \end{cases}$$

In Figure 5, the histogram of difference data has a Laplace distribution and is around the origin; therefore, the sample mean is approximately equal to zero

and $$\begin{cases} \mu_{ij} = 0 \\ \\ \alpha^2_{ij} = 1/(n-1)^2 \qquad (d_{i+k,j+1})^2 \end{cases} \qquad (10)$$

The α_{ij} is used to represent the activity of subimages,

$$\text{The activity of subimages} \begin{cases} \text{high detail} & T1 < \alpha_{ij} \\ \text{average detail} & T2 \leq \alpha_{ij} \leq T1 \\ \text{low detail} & \alpha_{ij} \leq T2 \end{cases}$$

This approach has a satisfactory performance of subimage classification. In Figure 17, class one subimages, we can see that most sharp edges, the detailed regions such as the girl's eyes and the feather, are classified. In Figure 18, class three, most of the flat regions are also classified,
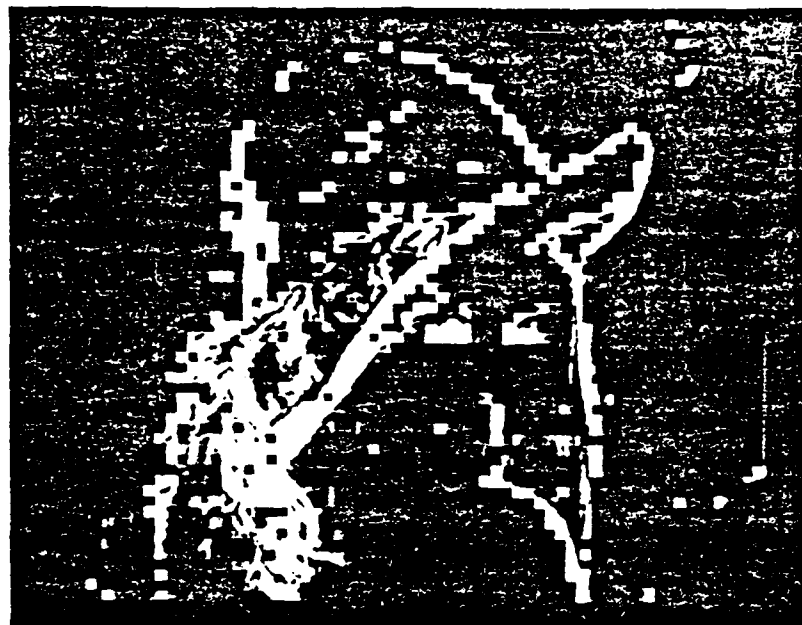
Figure 17. Subimage classification by variance of differ-
ences, high detail.

Figure 18. Subimage classification by variance of differ-
ences, low detail.
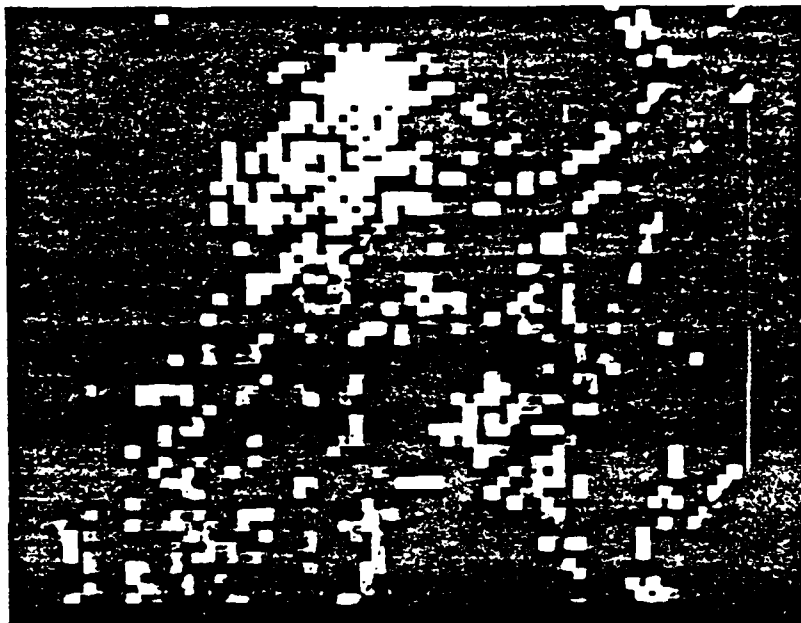
Figure 19. Subimage classification by variance of differences, average detail.

and in Figure 19 is class 2, in between classes 1 and 3. By Equation 10, the patterns in Figure 14 will not be classified into the class of low detail because the error of interpolation is large.

Another important advantage of this approach should be pointed out. Since the difference data contains the information of the subimage activity and they are to be transmitted, it is not necessary to transmit the extra bits for indexing each subimage activity. Thus, a slight bit reduction could be obtained.

Multiplication and square root operations require much longer machine time than addition and logic operations. Unfortunately the above algorithm has brought a large amount of multiplication operations, which is opposite to the goal of a real-time data compression system. A desirable feature of a data compression method is to have not only a high compression ratio but also a fast operation. This demand leads to our third approach to the subimage classification.

Subimage Classification by the Absolute Values of Differences

As mentioned above, addition and logic operations are preferred for subimage classification. Gimlett [10] suggested that "the weighted sum of the absolute values of the transform coefficients, defined herein as the activity index, is proposed as an objective measure of scene business

"for adaptive transform image coding. This idea is adopted into the spatial domain.

The measure of subimage activity is defined as

$$a_{ij} = \ln \frac{1}{K} \sum_{k} \sum_{l} d_{i-k,j-l} \quad \begin{cases} k,l(0,2,4\ldots,n-2) \\ -k \neq l = 0 \end{cases}$$

$$(12)$$

where n is a subimage size, d_{ij} is difference. This algorithm performs the classification also very well, and the results, Figures 20, 21 and 22, also match our subjective measure. Compared with the second approach, the machine time is reduced about one/third. Hence the third approach is considered a successful method to objectively measure the subimage activity, and a_{ij} will be used to classify the activity of subimages,

$$\text{The activity of subimages} \begin{cases} \text{high detail} & a_{ij} > T1 \\ \text{average detail} & T2 \le a_{ij} \le T1 \\ \text{low detail} & T2 > a_{ij} \end{cases}$$

3.2 Optimal Quantization

After the interpolation, the differences will pass through a quantizer. The quantized differences then will be transmitted. A quantizer is a device whose output can have only a limited number of possible values. Each input either analog or digital signal is forced to one of the allowable output values. The input range is divided into a number of
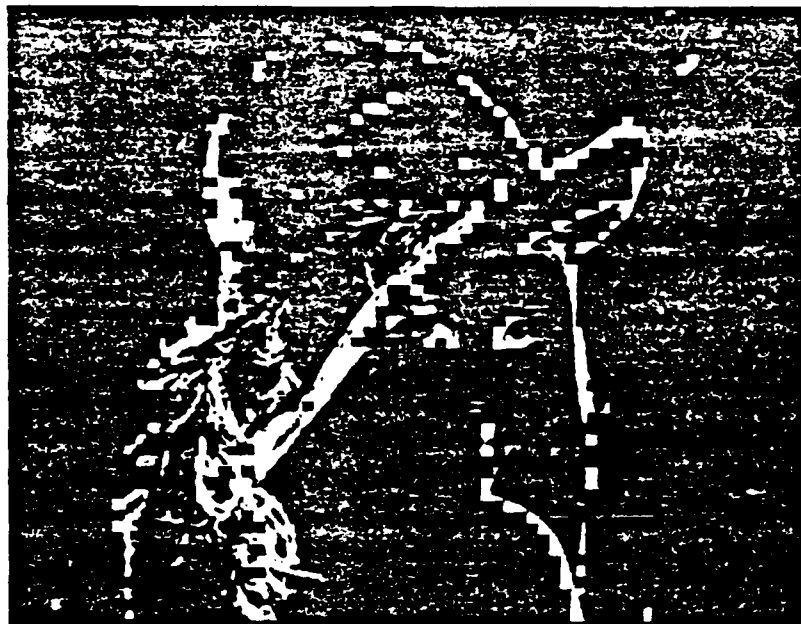
Figure 20. Subimage classification by the absolute value of differences, high detail.

Figure 21. Classification by absolute value of differences, average detail.

Figure 22. Classification by absolute value of differences, low detail.

bins equally as illustrated in Figure 23. If an input falls into the kth bin, the output is the value Q_k corresponding to the center of the Kth bin so that each input is rounded off to the center of the bin into which it falls. A uniform quantizer has all its bin widths equal. Nonuniform quantizers allow different bins to have different widths.

In the Adaptive Recursive-IDPCM data compression system, the quantization strategy is to choose the quantizer levels Q_i so that they minimize the mean-square-error. This error is given by

$$e_q = \sum_{i=1}^{n} \int_{X}^{X_{i+1}} (X - Q_i)^2 P(x) dx \qquad (14)$$

where $x_1 < x_2 < \ldots < x_{n+1}$ and $Q_1 < Q_2 < Q_3 \ldots < Q_n$ are decision boundaries and the quantizer output levels, respectively, and $P(x)$ is a probability density function of differences. Considering Figure 24, the histogram of the differences, let $F(x)$ represents the number of differences which have values equal to x_i, then the density function $P(x_i)$ is equal to

$$P(x_i) = \lim_{\Delta X \to 0} \frac{F(X_i < X < X_i < \Delta X)}{\Delta X} \qquad (15)$$

If we choose $\Delta X = 1$ (because values of subsamples are integers), $F(x)$ is approximately equal to the probability density function $P(x)$.

quantizer input range

x_0 x_1 x_2 x_3 x_4

bin 1   bin 2   bin 3   bin 4

Q_1 Q_2 Q_3 Q_4

quantizer output levels
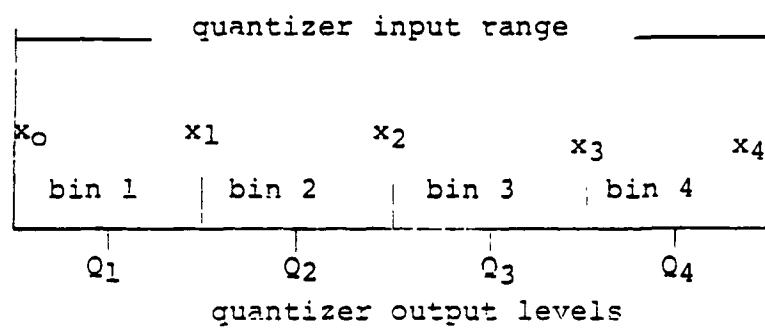
Figure 23. Uniform quantizer.
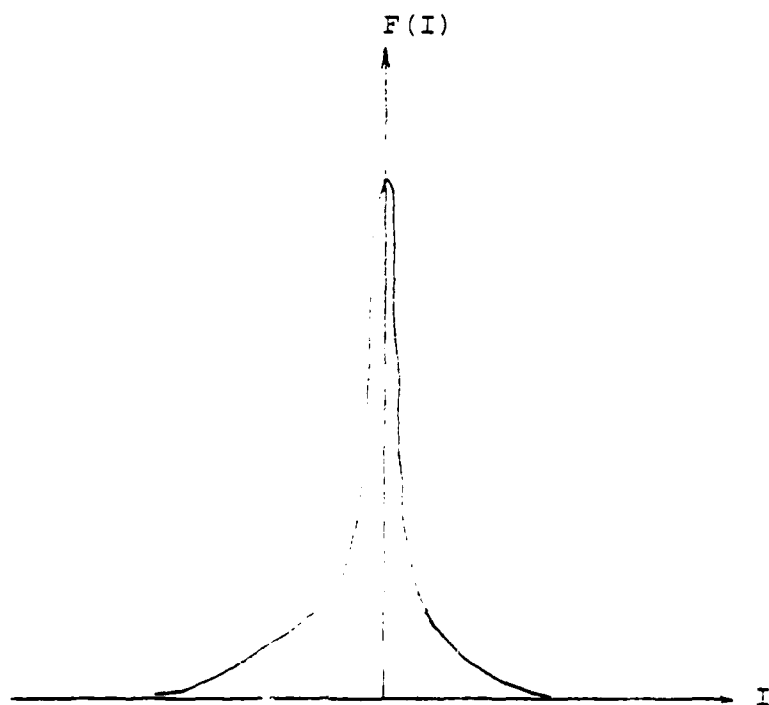
Figure 24. Histogram of the differences.

Taking a partial derivative of Equation 14 with respect to Q_i gives

$$\frac{\partial e_q}{\partial Q_i} = -2 \int_{X_i}^{X_{i+1}} (X - Q_i)P(x)dx = 0 \qquad (16)$$

$$Q_i = \frac{\int_{X_i}^{X_{i+1}} XP(X)dx}{\int_{X_i}^{X_{i+1}} P(X)dx} \qquad (17)$$

In order to solve two unknown variables Q_i and X_i, we also take a partial derivative of Equation 14 with respect to X_i

$$\frac{\partial e_q}{\partial X_i} = \frac{\partial}{\partial X_i}\left\{ \int_{X_{i-1}}^{X_i} (X - Q_{i-1})^2 P(x)dx + \int_{X_i}^{X_{i+1}} (X - a_i)^2 P(x) \right\} = 0,$$

and as a result

$$(X_i - Q_{i-1})^2 P(x) - (X_i - Q_i)^2 P(x) = 0 \qquad (18)$$

$$X_i - Q_{i=1} = Q_i - X_i \qquad (19)$$

From simultaneous Equations 17 and 19

$$\begin{cases} Q_i = \dfrac{\int_{X_i}^{X_{i+1}} X\,(X)dx}{\int_{X_i}^{X_{i+1}} P(X)dx} & (20) \\[20pt] X_i - Q_{i-1} = Q_i - X_i & (21) \end{cases}$$

optimum quantizer output levels are determined. Figure 25 shows a half range of 3 bits quantizer input and output.

3.3 Adaptive Recursive-IDPCM Process

The equations of the Adaptive-Recursive-IDPCM are

$$
\text{interpolation}
\begin{cases}
\overline{P}_{ij} = 1/4(p_{ij + n/2, \ i + n/2} + \\[6pt]
\qquad P_{i - n/2, \ j - n/2} + \\[6pt]
\qquad P_{i - n/2, \ j + n/2} + P_{i + n/2, \ j - n/2}) \\[6pt]
\qquad \text{when on interlaced field} \qquad (22) \\[18pt]
\overline{P}_{ij} = 1/2(P_{i, \ j + n/2} + P_{i, \ j - n/2})
\end{cases}
$$

when on scan lines

quantization $\qquad d_{ij} = Z(P_{ij} - \overline{P}_{ij})$ $\qquad\qquad\qquad$ (23)

reconstruction $\quad \hat{P}_{ij} = \overline{P}_{ij} + d_{ij}$ $\qquad\qquad\qquad$ (24)

where n is the number of pixels by which subsamples are separated. In Adaptive Recursive-IDPCM, the subimage size is selected equal to the number of pixels by which the original image is sampled. Figure 26 shows a case in which there is a 8:1 subsampling of image pixels along the
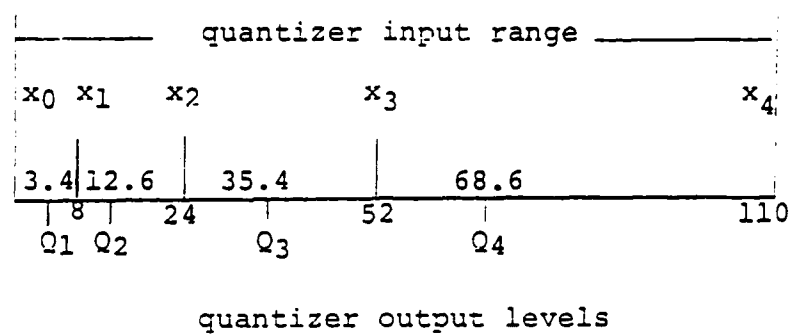
Figure 25.   Non-uniform quantizer.

```
    *  .  .  .  o  .  .  .  *  -  -  -
    .  .  .  .  .  .  .  .  .  -  -  -
    .  .  .  .  .  .  .  .  .  -  -  -
    .  .  .  .  .  .  .  .  .  -  -  -
Scan Lines  o  .  .  .  o  .  .  .  o  -  -  --        Interlaced
    .  .  .  .  .  .  .  .  .  -  -  -               Fields
    .  .  .  .  .  .  .  .  .  -  -  -
    .  .  .  .  .  .  .  .  .  -  -  -
    *  .  .  .  o  .  .  .  *  -  -  -
```
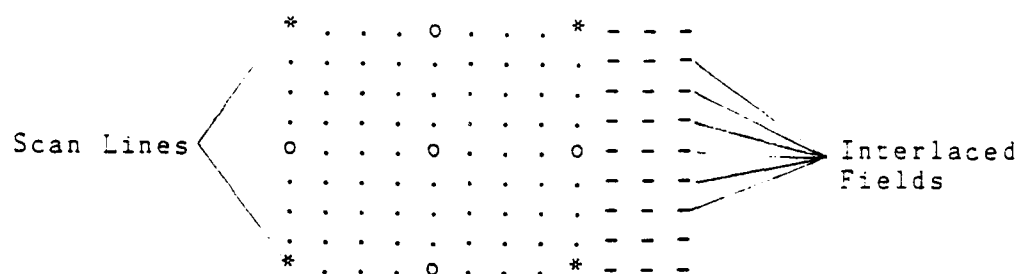
* = subsamples to be transmitted
. = position of original pixels
O = interpolated pixels

Figure 26. First set of interpolation of an 8 x 8 pixels
            subimage.

```
    *  .  +  .  o  .  +  .  *  -  -  -
    .  .  .  .  .  .  .  .  .  -  -  -
    +  .  +  .  +  .  +  .  +  -  -  -
    .  .  .  .  .  .  .  .  .  -  -  -
Scan Lines  o  .  +  .  o  .  +  .  o  -  -        Interlaced
    .  .  .  .  .  .  .  .  .  -  -  -               Fields
    +  .  +  .  +  .  +  .  +  -  -  -
    .  .  .  .  .  .  .  .  .  -  -  -
    *  .  +  .  o  .  +  .  *  -  -  -
```
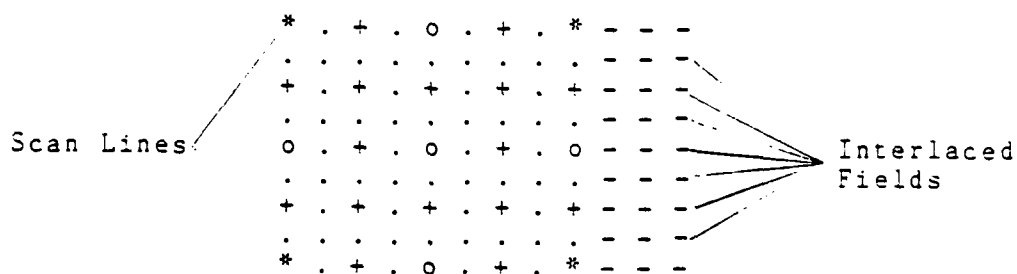
* = subsamples to be transmitted
o = first set of reconstructed pixels
+ = second set of interpolated pixels
. = position of original pixels

Figure 27. Second set of interpolation of an 8 x 8 pixels
            subimage.

line, and 8:1 subsampling of image lines. The first set of interpolation is shown by arrows.

With the above equations, the interpolation, the subimage classification, and the quantization, the adaptive data compression can be conducted in two schemes.

1. The bit rate assignment of each subimage is based on the measure of subimage activity

$$
\begin{array}{l}
\text{bit rate} \\
\text{assigned} \\
\text{to each} \\
\text{subimage}
\end{array}
\left\{
\begin{array}{l}
\left\{
\begin{array}{l}
4 \text{ bits} \Rightarrow \text{first set of differences} \quad T1 \leq C_{ij} \\
3 \text{ bits} \Rightarrow \text{second set of differences}
\end{array}
\right. \\
\left\{
\begin{array}{l}
3 \text{ bits} \Rightarrow \text{first set of differences} \quad T2 \leq C_{ij} < T1 \\
2 \text{ bits} \Rightarrow \text{second set of differences}
\end{array}
\right. \\
\left\{
\begin{array}{l}
2 \text{ bits} \Rightarrow \text{first set of differences} \quad C_{ij} < T2 \\
0 \text{ bits} \Rightarrow \text{second set of differences}
\end{array}
\right.
\end{array}
\right.
$$

$$(25)$$

where $T1 \leq C_{ij}$ indicates high detail, $T2 \leq C_{ij} < T1$, average detail; $C_{ij} < T2$, low detail, C_{ij} is equal to σ_{ij} (8), or α_{ij} (10), or β_{ij} (12), and α_{ij} and β_{ij} are calculated from the first set of differences. However the reconstructed image does not show very satisfactory quality. The problem is that those subimages classified into class 1 or class 2 were finely reconstructed (e.g., the feather, the girl's eyes, etc.); however, the subimages in the class 3 were poorly reconstructed (e.g., the hat, girl's shoulder, etc.). On the other hand, if we look at the histograms of the

second set of differences in Figures 28 and 29, we find that a large number of difference data has zero or nearly zero values. This implies that the data compression for subimages in classes 1 and 2 is still inefficient. Of course, we could adjust thresholds to classify more subimages into class 2 and fewer subimages into class 1, but the improvement would not be very notable. We noticed that in the Recursive-IDPCM method, the differences are calculated and quantized at each recursion. If we can decide the quantization level at each recursion, the data compression will be efficient. This leads to the second scheme of adaptation.

2. The differences are quantized adaptively at each recursion and bit assignment is based on Equations 10 and 12. The quantization bit assignment is shown in the following relations.

bit rate for the $\begin{cases} 4 \text{ bits} \\ 3 \text{ bits (first recursion)} \\ 0 \text{ bits} \end{cases}$ first set of difference. quantization

$$\begin{cases} T1 \le C_{ij} \\ T2 \le C_{ij} \le T1 \\ C_{ij} < T2 \end{cases} \tag{26}$$

Bit rate for the $\begin{cases} 3 \text{ bits} \\ 2 \text{ bits (second recursion)} \\ 0 \text{ bits} \end{cases}$ second set of difference quantization

$$\begin{cases} T1 \le C_{ij} \\ T2 \le C_{ij} < T1 \\ C_{ij} \le T2 \end{cases} \tag{27}$$
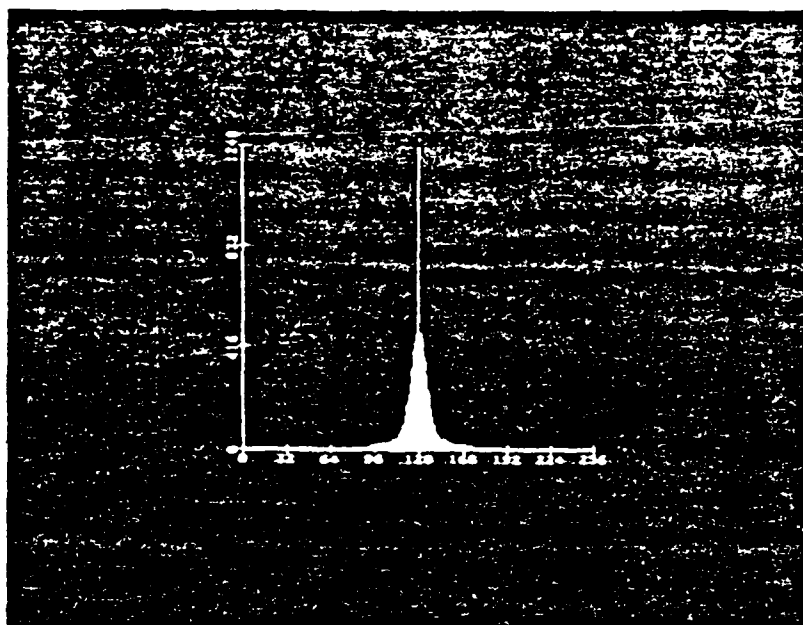
Figure 28.   Histogram of the second set of differences in class 2.
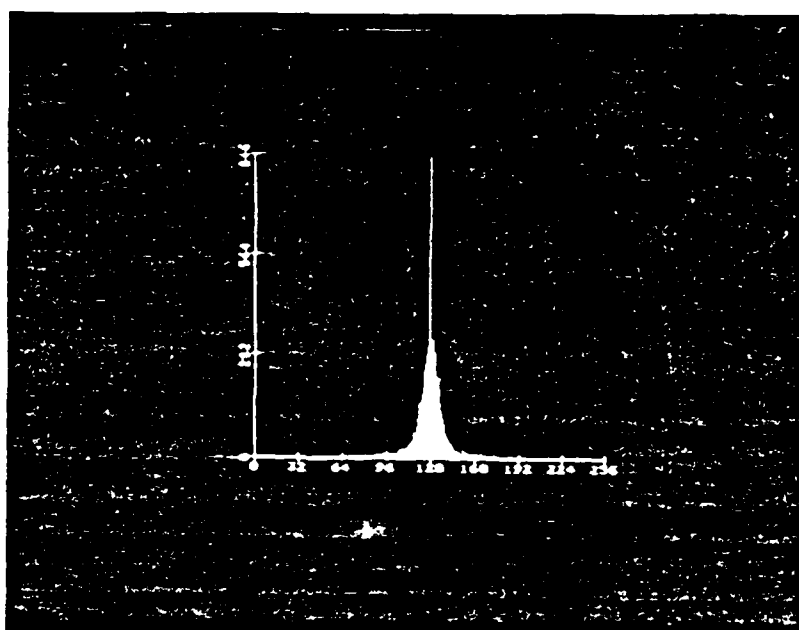
Figure 29.   Histogram of the second set of differences in class 1.

where C_{ij} can be equal to x_{ij} (10) or β_{ij} (12).

When a subimage size is 8 x 8 pixels, possible bit assignments on a subimage are shown in Figure 30. The Adaptive-Recursive-IDPCM system diagram is shown in Figure 31.

3.4 Performance of the Adaptive Recursive-IDPCM

The Adaptive Recursive-IDPCM data compression method has been simulated on the PDP 11/70-IIS image processing system in the Digital Image Analysis Laboratory. The result shows that a further improvement to the Recursive-IDPCM has been achieved. Comparing the two reconstructed images in Figures 32 and 33, it can be seen that in the reconstructed image which was compressed by Recursive-IDPCM, the detailed regions such as the girl's shoulder, the edge of the hat were jagged and her eyes, eyelash, and the feather were blurred; however, in the reconstructed image of the Adaptive Recursive IDPCM, this type of degradation is much less in evidence even with a lower bit rate than used in the Recursive-IDPCM. But in some simple regions of the reconstructed image by the Adaptive Recursive-IDPCM method, degradations are still noticeable, such as the top of the girl's hat. It is because of the not-very obvious distortion in simple regions that a large number of bits can

```
6  3  0  3  -  0  3  0  6        6  0  2  0  3  0  2  0  6
0  0  0  0  0  0  0  0  0        0  0  0  0  0  0  0  0  0
3  0  3  0  3  0  3  0  3        2  0  2  0  2  0  2  0  2
0  0  0  0  0  0  0  0  0        0  0  0  0  0  0  0  0  0
4  0  3  0  -  0  3  0  4        3  0  2  0  3  0  2  0  3
0  0  0  0  0  0  0  0  0        0  0  0  0  0  0  0  0  0
3  0  3  0  3  0  3  0  3        2  0  2  0  2  0  2  0  2
0  0  0  0  0  0  0  0  0        0  0  0  0  0  0  0  0  0
6  0  3  0  4  0  3  0  6        6  0  2  0  3  0  2  0  6


2  0  0  0  2  0  0  0  6        6  0  2  0  2  0  2  0  6
0  0  0  0  0  0  0  0  0        0  0  0  0  0  0  0  0  0
0  0  0  0  0  0  0  0  0        2  0  2  0  2  0  2  0  2
0  0  0  0  0  0  0  0  0        0  0  0  0  0  0  0  0  0
2  0  0  0  2  0  0  0  2        2  0  2  0  2  0  2  0  2
0  0  0  0  0  0  0  0  0        0  0  0  0  0  0  0  0  0
0  0  0  0  0  0  0  0  0        2  0  2  0  2  0  2  0  2
0  0  0  0  0  0  0  0  0        0  0  0  0  0  0  0  0  0
6  0  0  0  2  0  0  0  6        6  0  2  0  2  0  2  0  6
```

Figure 30. Bit assignments for an 8 x 8 subimage.
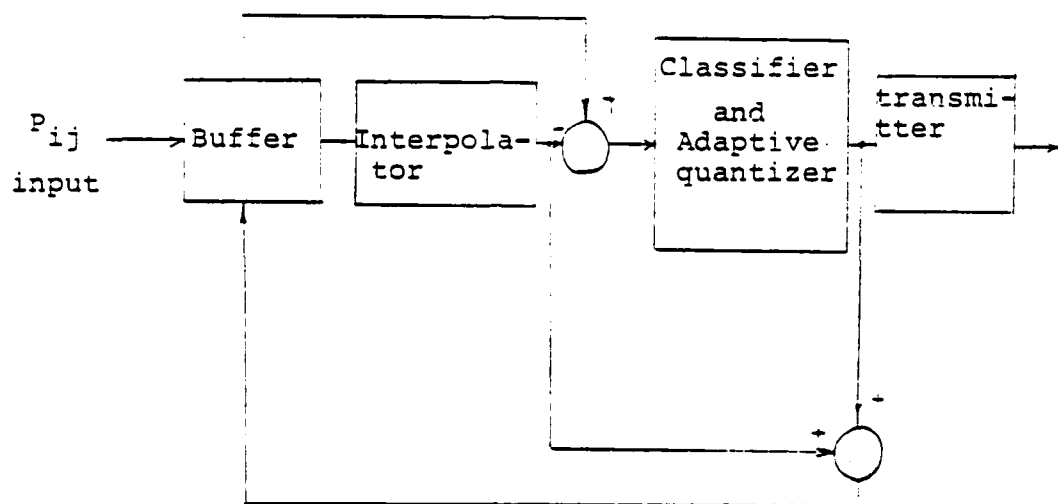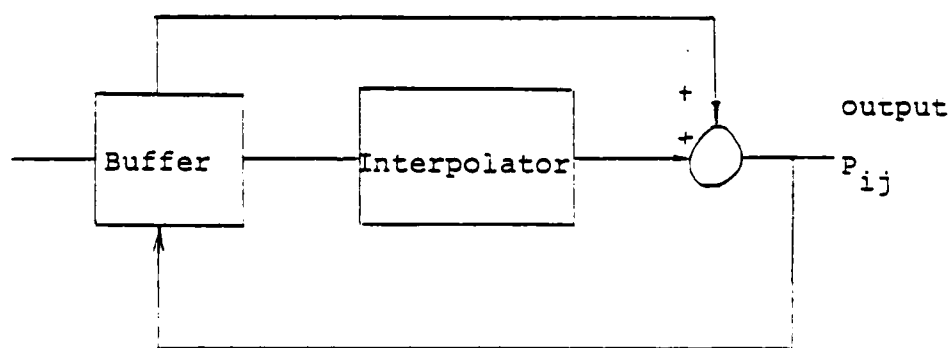
Figure 31.   Adaptive Recursive-IDPCM system block diagram.

be saved for detailed regions which are very sensitive to human eyes.

The different partition of the original image was tested by dividing an image into different sizes of subimages. The following table shows the relation between the size of subimages and the number of subimages in each class (Table 1).

The smaller the subimage size is, the larger the number of simple subimages will be because the correlation between the nearest pixels is higher. As a result, the difference values will become smaller and the bit rate for quantizing differences can be reduced. On the other hand, the overall bit rate was increased because the image had to be sampled more densely. However, a very good reconstructed image was obtained with the bit rate 0.546 (Figure 34). When the size of the subimages is too large (e.g., 16 x 16), the subject quality of the reconstructed image shown in Figure 35 is not very satisfactory, although a slight bit reduction has been obtained. This is because there is not much correlation among too coarsely subsampled pixels. For the image used in this simulation, a 8 x 8 subimage is a suitable size. Generally, the selection of optimum subimage size for adaptive data compression schemes depends on the statistics of the image data.

Table 1. Number of subimages.

Subimage Size	Three Classes of Subimage (number of subimages)		
	Low Detail	Average Detail	High Detail
16 x 16	313	372	339
8 x 8	2870	844	382
4 x 4	10,317	3241	2826

One problem which should be pointed out is that although the subjective quality of the reconstructed image has been improved by using the adaptive scheme, the objective quality represented by RMSE (2) has not been achieved. For example, in Figure 32, Recursive-IDPCM, the BPP is 0.3577 and the RMSE is 0.00818; in Figure 36, Adaptive Recursive IDPCM, the BPP is 0.3561 and the RMSE is 0.00907. For the same bit rate, the Adaptive Recursive-IDPCM has a slightly larger RMSE than the Recursive-IDPCM. But it has been pointed out [11] that quantitative measures of image fidelity which have been developed are not perfect. Therefore, our evaluation on the Adaptive Recursive-IDPCM method is based on its subjective measure.

a.

b.

Figure 3C. Recursive-IDPCM -- (a) BPP = 0.3577, MSE = 0.00818; and (b) BPP = 0.2741, MSE = 0.00830.

a.

b.

Figure 33.   Adaptive Recursive-IDPCM (a) BPP = 0.33-6, MSE = 0.0101 (subimage classification based on variance of differences); and (b) BPP = 0.3815, MSE = 0.00970 (subimage classification according to absolute value of differences).

a.

b.

Figure 34.   Adaptive Recursive-IDPCM. subimage size - - -
-- (a) BPP = 0.5462. MSE = 0.00??6?: and ? ???
= 0.6081, MSE = 0.00?64?.

a.

b.

Figure 35. Adaptive Recursive-IDPCM, subimage size 16 x 16.
-- a) BPP = 0.2364, MSE = 0.0118; and b) BPP =
0.1624, MSE = 0.01536.

a.

b.

Figure 36. Adaptive RIDPCM. -- (a) BPP = 0.3561, MSE = 0.00907 (subimage classification according to variance of differences); and (b) BPP = 0.48365, MSE = 0.009194 (subimage classification according to variance of differences).

a.

b.

Figure 37.   Adaptive Recursive-IDPCM (subimage classifica-
             tion according to absolute values of difference,
             subimage size 8 x 8). -- (a) Reconstructed
             image, BPP = 0.4907, MSE = 0.009354; and (b)
             Original image.

CHAPTER 4

COMPRESSION OF COMPUTER TOMOGRAPHIC PROJECTION
BY THE ADAPTIVE RECURSIVE-IDPCM

It has been pointed out [12] that the projection
matrix of computer tomographics contains a great deal of
redundant information. Therefore, the projection matrix is
compressible. The compression of tomographic projections
using the DPCM method has been studied [12]. In this
thesis, a new approach of compressing tomographic projec-
tions using the Adaptive Recursive-IDPCM is introduced.

A projection taken along a set of parallel rays is
called a parallel projection, two examples of which are
shown in Figure 38, and a projection along parallel rays in
a certain angle is calculated by the function

$$P_\theta(x) = \int_{-\infty}^{\infty} f(x,y)dy$$

where $f(x,y)$ represents a two-dimensional image pixel value.

A projection matrix is also depicted in Figure 39
and will be compressed. It has also been pointed out [12]
that the amount of redundancy appears to be strongly
dependent upon the angle of projection, the redundancy is
highest near the angles of 0°, 90° and 180°. Because of

58
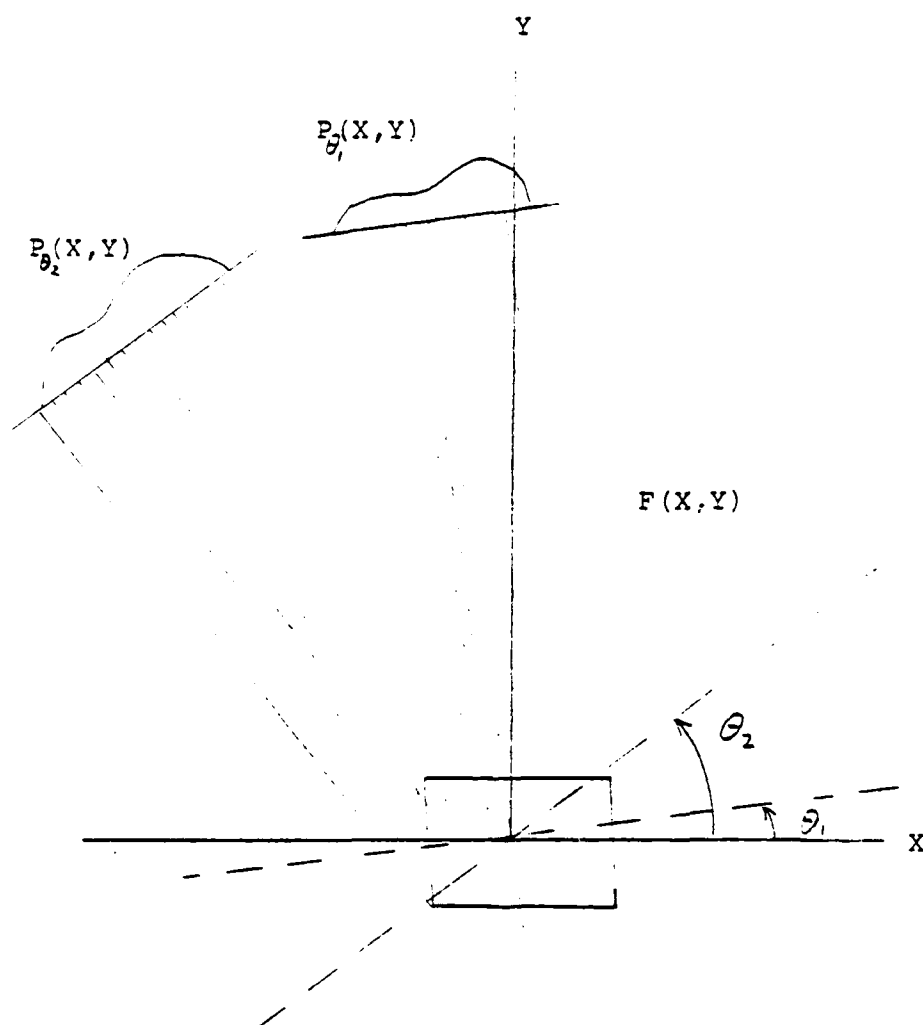
Figure 38.   Parallel projections.

Projection Angle

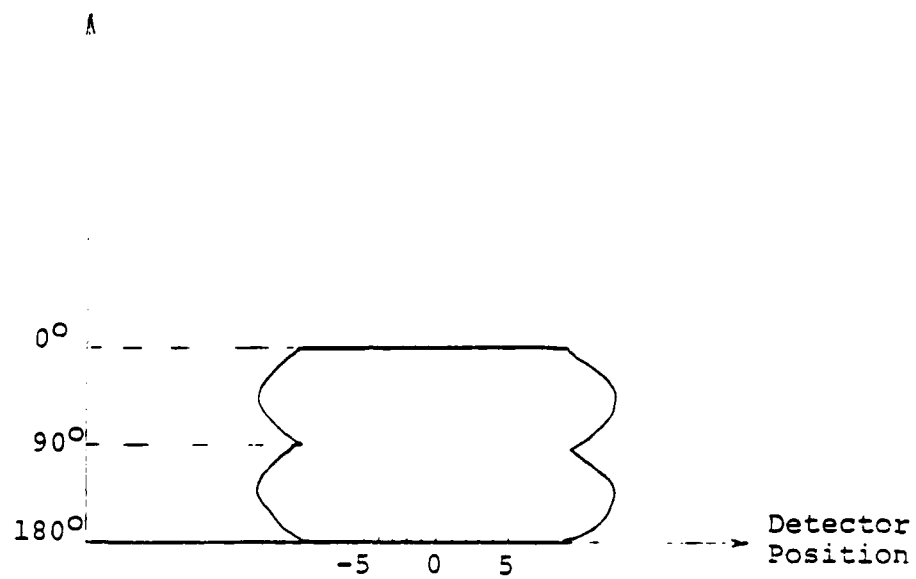0°

90°

180°

-5 0 5

Detector
Position

Figure 39. Projection matrix.

Figure 40. 128 x 128 Original image.

Figure 41. 128 x 128 Back projection without data compression.

Figure 42. Projection matrix of the image in Figure 40.

Figure 43. Reconstructed image, BPP = 3.9 bits per projection element.

63

this characteristics, an adaptive data compression scheme seems to be more suitable.

A 102 x 184 projection matrix in Figure 42 was obtained from a 128 by 128 image shown in Figure 40, and it was a 102 x 184 matrix in Figure 42. To simplify programming, the scalloped ends of the projection matrix were trimmed before encoding, producing a rectangular matrix. The obtained rectangular matrix was compressed by the Adaptive Recursive-IDPCM method discussed in Section 3.3. The methods of calculating a projection and a back projection can be found from references [12 and 13]. The reconstructed image quality in Figure 42 is improved, which can be seen by comparing the image in Figure 42, with the image in Figure 10c from the reference [12]. However, the reconstructed image even without data compression is distorted, as shown in Figure 41. As a result, the reconstructed image with data compression does not have satisfactory quality although some improvement has been achieved by using the Adaptive Recursive-IDPCM method.

CHAPTER 5

CONCLUSION

In this thesis, we have discussed the fundamentals of data compression as well as details of the Adaptive Recursive-IDPCM data compression method. In order to implement adaptive schemes, several subimage activity classification algorithms were tested, and the classification using the absolute value of difference was considered to be the best. The optimum quantizer was designed to minimize the quantization error based on the mean-square-error criterion. Especially when the differences were quantized adaptively at each recursion, the Adaptive data compression method performed more efficiently. Compared with the Recursive-IDPCM, we have seen that the subjective quality of the reconstructed image using the adaptive scheme has been notably improved. As is the case for the IDPCM system, the Adaptive Recursive-IDPCM system is also less sensitive to channel error than the DPCM system. Although the encoding and decoding complexity are slightly increased, the Adaptive Recursive-IDPCM can still be easily implemented for a real-time system.

64

It is mentioned in the introduction that image data compression methods are basically categorized into two classes. One class is data compression in the transform domain, and another class is data compression in the spatial domain. In the transform domain, many transform coding algorithms achieve high performance, small sensitivity to fluctuation in data statistics, but their hardware complexity is high. In the spatial domain, the predictive methods are generally easy to implement, but they are sensitive to data statistics. The Adaptive Recursive-IDPCM system seems to have both the advantages of predictive coding methods and of transform coding methods. Real-time implementation of the Adaptive Recursive-IDPCM method is the suggested step for future research so that this method can actually be tested.

REFERENCES

1. Nuggehally, Jayant, "Digital Coding of Waveforms," Prentice-Hall, 1984.

2. Jain, Anil K., "Image Data Compression: A Review," Proceedings of the IEEE, VOl. 69, No. 3, March 1981.

3. Netravali, Arun N., "On Quantizers for DPCM Coding of Picture Signals," IEEE Trans. Information Theory, Vol. IT-23, May 1977.

4. Netravali, Arun N., "Picture Coding: A Review," Proceedings of the IEEE, Vol. 68, No. 3, March 1980.

5. Hunt, B. R., "An Optical Analogy to DPCM Digital Image Compression," SPIE Proceedings, Vol. 119, "Applications of Digital Image Processing," pp. 85-95.

6. Z. D. Cao and B. R. Hunt, "Image Data Compression by Recursive IDPCM," to be published.

7. Berger, T., "Optimum Quantizers and Permutation Codes," IEEE Trans. Information Theory, Vol. IT-18, pp. 754-755, Nov. 1972.

8. Gonzalez, R. C. and Paul Wintz, "Digital Image Processing," Addison-Wesley Publishing Company, 1977.

9. Papoulis, A., "Probability, Random Variables, and Stochastic Processes," McGraw-Hill Book Company, 1984.

10. Gimlett, T. I., "Use of Activity Classes in Adaptive Transform Image Coding," IEEE Trans. Communication. Vol. COM-23, pp. 785-786, July 1975.

11. Pratt, W. K., "Digital Image Processing," A Wiley-Interscience Publication, 1978.

12. Hunt, B. R. and R. H. Strickland, "Feasibility Studies of Optical Processing of Image Bandwidth Compression Schemes," DIAL Annual Final Report, 1984, pp. 4-25. The University of Arizona.

13. Rosenfeld, A. and Arinash C. Kak, "Digital Picture Pro-
    cessing," Academic Press, Inc., 1982.

14. Jain, Anil K., "Image Coding via a Nearest Neighbors
    Image Model," IEEE Transactions on Communications,
    Vol. COM-23, No. 3, March 1975.

CORRECTING IMAGES FOR

ATMOSPHERIC TURBULENCE

77

AN EXTENSION TO THE ANALYSIS OF THE SHIFT-AND-ADD METHOD:

THEORY AND SIMULATION

by

Karen Frances West

_____

A Dissertation Submitted to the Faculty of the

COMMITTEE ON APPLIED MATHEMATICS

In Partial Fulfillment of the Requirements
For the Degree of

DOCTOR OF PHILOSOPHY

In the Graduate College

THE UNIVERSITY OF ARIZONA

1 9 9 5

THE UNIVERSITY OF ARIZONA
GRADUATE COLLEGE

As members of the Final Examination Committee, we certify that we have read

the dissertation prepared by _____ Karen Frances West _____

entitled _____ An Extension to the Analysis of the Shift-and-Add Method: _____

_____ Theory and Simulation _____

_____

_____

_____

and recommend that it be accepted as fulfilling the dissertation requirement

for the Degree of ____ Doctor of Philosophy _____.

_____   5-7-85
                                        Date

_____   May 7 1985.
                                        Date

_____   5|7|85
                                        Date

_____   _____
                                        Date

_____   _____
                                        Date

Final approval and acceptance of this dissertation is contingent upon the
candidate's submission of the final copy of the dissertation to the Graduate
College.

I hereby certify that I have read this dissertation prepared under my
direction and recommend that it be accepted as fulfilling the dissertation
requirement.

_____   5-7-85
Dissertation Director   Date

ACKNOWLEDGMENTS

TABLE OF CONTENTS

TABLE OF CONTENTS -- Continued

LIST OF ILLUSTRATIONS

LIST OF ILLUSTRATIONS -- <u>Continued</u>

LIST OF TABLES

ABSTRACT

The turbulent atmosphere degrades images of objects viewed
through it by introducing random amplitude and phase errors into the
optical wavefront. Various methods have been devised to obtain true
images of such objects, including the shift-and-add method, which is
examined in detail in this work.

It is shown theoretically that shift-and-add processing may
preserve diffraction-limited information in the resulting image, both
in the point source and extended object cases, and the probability of
ghost peaks in the case of an object consisting of two point sources is
discussed. Also, a convergence rate for the shift-and-add algorithm is
established and simulation results are presented. The combination of
shift-and-add processing and Wiener filtering is shown to provide
excellent image restorations.

CHAPTER 1

INTRODUCTION

Imaging through random media is a problem with applications in
a variety of disciplines. It arises in medical ultrasound imaging
where the random medium is biological tissue. It also occurs in wave
propagation through the ocean where there are inhomogeneities due to
temperature variations and the presence of biological material. In the
atmosphere, turbulence arising from temperature variations creates
random effects in images obtained through ground-based astronomy.

In each case, the resulting images have a characteristic grainy
or "speckled" appearance. This presents special difficulties in image
restoration because the degradations are random in nature, and if we
think in the context of linear systems theory, we are limited to
information about the average point spread function only. One method
developed to counter this problem, specifically for the case of
ground-based astronomy, is the shift-and-add method (Bates and Cady,
1980; Cady and Bates, 1980), which will be examined in detail in this
dissertation.

Since the degradations produced by the atmosphere are random in
nature, Chapter 2 is devoted to characterizing statistically the
intensity of an optical wave which has passed through the atmosphere.
Although the literature is by no means unanimous in its choice of an

1

appropriate probability distribution for intensity, the lognormal distribution is heavily favored, both by theorists and experimentalists, and we will present a physical model and experimental evidence to support its use.

In Chapter 3, we discuss typical modes of astronomical imaging--short exposures, long exposures, and speckle interferometry--and also review some of the major advances in obtaining more information from such images. Among the algorithms to be considered are speckle holography, Fienup's iterative algorithms, Knox-Thompson, and shift-and-add.

Since shift-and-add is such a simple and easily implemented algorithm, the question of why it works naturally occurs. This question is analyzed in detail in Chapter 4, which constitutes the major original contribution of this dissertation. We will derive the combined point spread function for atmospheric degradation and shift-and-add processing, address the probability of error or of "ghost" peaks, examine the case of extended object imaging, and determine the rate of convergence of the algorithm. Our results in this chapter indicate that the shift-and-add method applied to a series of short exposure images may allow diffraction-limited information to be preserved.

In order to test the performance of shift-and-add processing and thus verify our analytical results, we have simulated atmospheric turbulence degradations, since no real data were available. We discuss the two algorithms used for this purpose in Chapter 5. The first,

developed by McGlamery (1967b), is an algorithm which considers phase degradations only. We subsequently modified this scheme to include amplitude effects as well.

In Chapter 6, we discuss generation of degraded images by convolving a simulated undegraded image with the point spread functions computed in Chapter 5. We then apply shift-and-add processing alone and a combination of shift-and-add processing and Wiener filtering to these images, obtaining excellent restoration results. As a caution against making excessive claims for the performance of this processing, we note that the simulated images are noise-free; however, the combined theoretical results of Chapter 4 and the simulation results of Chapter 6 demonstrate that the shift-and-add method is an effective and extremely easily implemented approach to restoring images corrupted by atmospheric turbulence and perhaps, other random degradations.

1.0

2.8

2.5

3.2

2.2

3.6

2.0

1.1

1.8

1.25

1.4

1.6
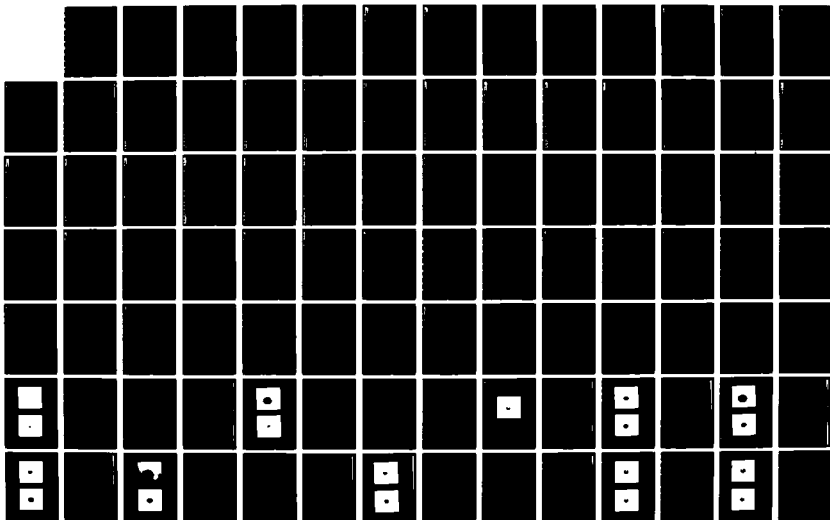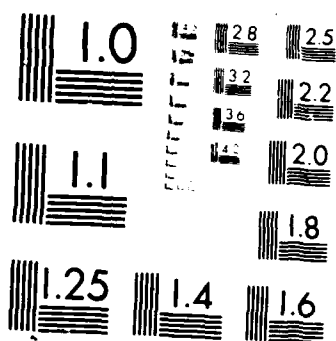
MICROCOPY RESOLUTION TEST CHART

CHAPTER 2

OPTICAL PROPAGATION THROUGH THE ATMOSPHERE

We are all familiar with the twinkling of stars as we observe
them through the earth's atmosphere. This phenomenon is due to random
phase and amplitude shifts in the optical path between the star and the
viewer's eye. These shifts are induced by atmospheric turbulence, a
condition primarily caused by temperature inhomogeneities arising from
the action of winds and from heat rising from the earth. Since
refractive index n is dependent upon temperature, these temperature
inhomogeneities give rise to regions with randomly varying refractive
index, which in turn result in the amplitude and phase shifts mentioned
above.

In ground-based astronomy, the viewer's eye is replaced by a
telescope, and because of the finite time required to record an image,
the random phase shifts produce a "speckle pattern" as the image of an
unresolved star or point source. (The term "speckle" is borrowed from
laser speckle because of similarities in appearance and in some
statistical models of the two phenomena, and it refers to a granular
structure in the image.)

Since the amplitude and phase shifts induced by the atmosphere
are random, we wish to characterize them by their statistical
properties. In particular, we want to determine the distribution of

4

intensity (or irradiance), since that is the quantity which is typically measured.

2.1 Justification of Lognormal Intensity Statistics for Speckle

We have chosen the lognormal model for intensity, as it is the one supported by the majority of the literature (Tatarski, 1961; Lawrence and Strohbehn, 1970; Korff, 1973; Fried, 1966; deWolf, 1969). However, this model is by no means unanimously agreed upon, and a good bibliography of the alternatives has been compiled by Fante (1975). Since the lognormal distribution is relatively unfamiliar, we have summarized its relevant properties in Appendix A. In this section, we will present a non-rigorous physical argument for lognormal intensity statistics and will also discuss some of the pertinent experimental evidence.

2.1.1 Physical Grounds for Lognormal Intensity Statistics

According to Strohbehn (1968), we will assume a laminar model of the turbulent atmosphere that consists of a large number N of slabs oriented perpendicular to the propagation direction and will derive the statistics of the phase and amplitude of an optical wave at the pupil of a telescope or optical system. We will depict this model in Figure 2.1, where s is the source, r is the receiver, A_o is the amplitude of the optical wave at the source (with phase assumed to be zero), A and ψ are the amplitude and phase at the receiver, L is the optical path-length, d_i is the (random) width of the ith division of the
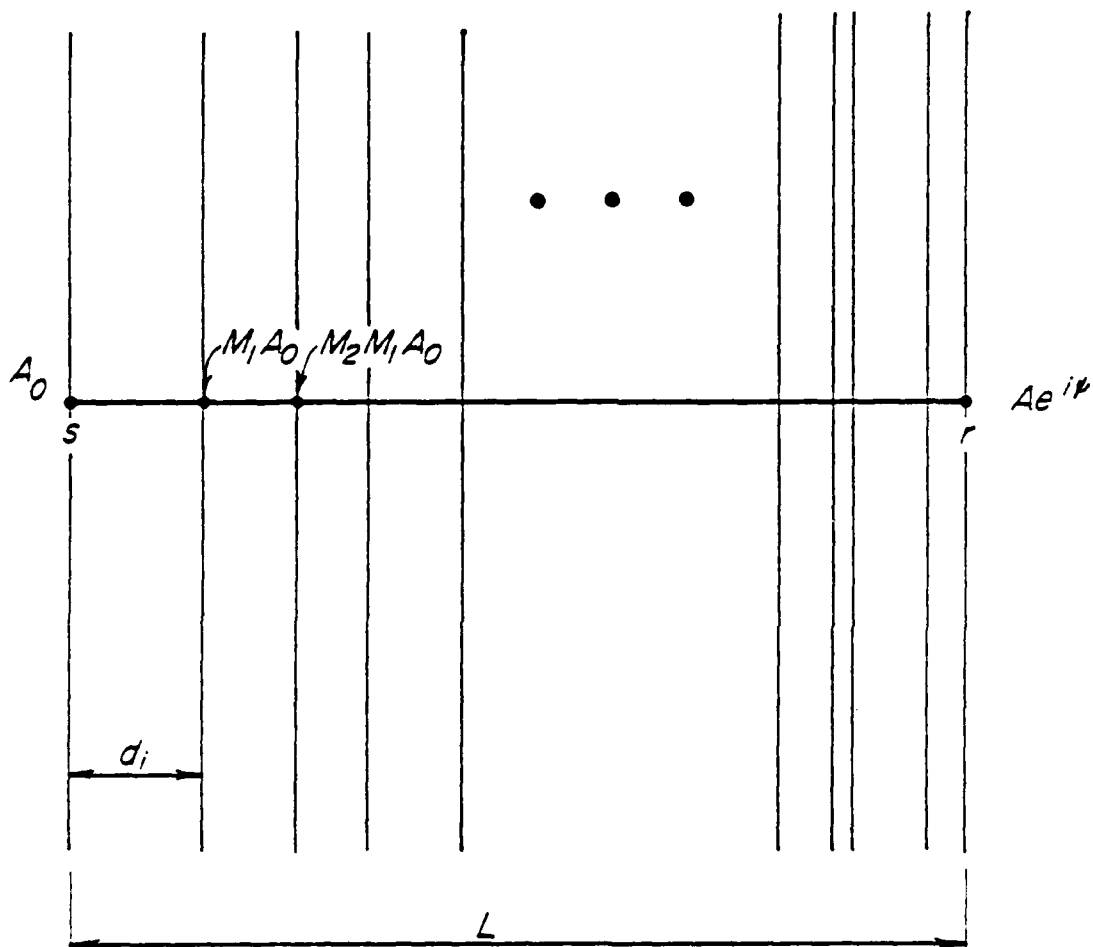
Figure 2.1. Laminar model of the turbulent atmosphere.

optical path, and n_i is the refractive index of the ith slab. The refractive index n_i is actually time dependent and may be written

$$n_i = n_o + \Delta n_i$$

where n_o is the mean of all the n_i, the refractive index of the atmosphere without turbulence, and Δn_i is the varying portion of n_i due to turbulence. Also, several assumptions are made. First, it is assumed that we are dealing with line of sight propagation with r located in the turbulent medium. This is the condition of ground-based astronomy as opposed to that of a satellite looking down through the atmosphere. Even stronger, we are considering only a straight line path from source to receiver; that is, ignoring contributions from scatter at the receiver. The second assumption is that the wavelength is much shorter than d_i for every i. This implies that we may use geometric optics. Third, we assume that Δn_i is very small compared to n_o. More specifically, $\Delta n_i / n_o$ is on the order of 10^{-6}. The fourth assumption is that turbulence is homogeneous and isotropic, which allows us to use this essentially one-dimensional model.

We now consider the amplitude A at the receiver. The following derivation is extremely simplistic, and it is now thought that all distortions of the optical wavefront (including those which cause amplitude or intensity fluctuations) are due to random phase shifts. In the case of intensity or amplitude fluctuations, phase shifts which occur high in the atmosphere cause the various portions of the distorted wavefront to travel in slightly different directions, thus

resulting in interference. This interference results in the observed amplitude or intensity fluctuations (Lawrence, 1976). We shall, however, proceed with this simplistic view of amplitude or intensity.

First, we define R_i, the reflection coefficient for amplitude at the boundary between the $(i-1)^{th}$ and the ith slabs for normally incident light:

$$R_i = \frac{\text{reflected amplitude}}{\text{incident amplitude}}$$

$$= \frac{n_i - n_{i-1}}{n_i + n_{i-1}}$$

$$= \frac{n_o + \Delta n_i - n_o - \Delta n_{i-1}}{n_o + \Delta n_i + n_o + \Delta n_{i-1}}$$

$$= \frac{\Delta n_i - \Delta n_{i-1}}{2n_o + \Delta n_i + \Delta n_{i-1}}$$

which is very small due to the third assumption in our model, so subsequently we shall ignore all reflected light. Thus if A_{i-1} is the amplitude of the wavefront incident upon the boundary, the amplitude of the transmitted wave is

$$A_i = A_{i-1} - R_i A_{i-1}$$
$$= (1 - R_i)A_{i-1}$$

We shall denote

$$M_i = 1 - R_i$$

and recall tha M_i is random due to dependence on Δn_i and Δn_{i-1}. So if

we start at the source s with an amplitude of A_0, the light hits the

first slab, and the amplitude transmitted to the second slab is $M_1 A_0$.

This process continues for each slab so that the amplitude at the

receiver is

$$A = M_N \ldots M_1 A_0.$$

Taking the natural logarithm,

$$\log A = \log M_N + \ldots + \log M_1 + \log A_0$$

where we may, without loss of generality, assume $A_0 = 1$ and drop the

last term. We then assume that the $\log M_i$ meet the requirements for

application of the Central Limit Theorem. One such set of requirements

(Papoulis, 1965), although not the most general, is that if we let $x_i = \log M_i$

    a. The x_i are independent,

    b. $\sum_{i=1}^{N} \sigma_{x_i}^2 \to \infty$ as $N \to \infty$,

    c. $\int_{\infty}^{\infty} (x_i)^a p_i(x_i) dx_i$ is finite for some $a > 2$.

Therefore, for N very large, $\log A$ is (approximately) Gaussian, which

implies that A is lognormal. We are, however, primarily interested in

the statistics of intensity I, since that is the quantity typically

measured. Intensity is related to amplitude by

$$I = A^2$$

or

$$\log I = 2 \log A$$

so that $\log I$ is also (approximately) Gaussian, and I is lognormally distributed.

We now turn our attention to the statistical distribution of phase at the receiver. Since the phase at s is assumed to be 0, the phase ψ at r is simply the sum of contributions from each slab

$$\psi = \sum_{i=1}^{N} \psi_i$$

$$= 2\pi \sum_{i=1}^{N} d_i / \lambda_i$$

where λ_i is the wavelength in the ith interval which varies due to Δn_i, the fluctuating portion of the refractive index. We let λ_o be the wavelength for propagation in the atmosphere (refractive index n_o) in the absence of the turbulent layers. Then for the ith layer

$$n_i = \lambda_i / \lambda_o,$$

so

$$\psi = 2\pi \sum_{i=1}^{N} d_i / (n_i \lambda_o)$$

$$= \frac{2\pi}{\lambda_o} \sum_{i=1}^{N} d_i / n_i.$$

But $n_i = n_o + \Delta n_i$, so

$$\psi = \frac{2\pi}{\lambda_o} \sum_{i=1}^{N} \frac{d_i}{n_o + \Delta n_i}$$

$$= \frac{2\pi}{\lambda_o n_o} \sum_{i=1}^{N} \frac{d_i}{1 + \Delta n_i / n_o} \; .$$

From the third assumption in our model,

$$\frac{\Delta n_i}{n_o} \ll 1,$$

so

$$\frac{1}{1 + \Delta n_i / n_o} = 1 - \frac{\Delta n_i}{n_o} + \left(\frac{\Delta n_i}{n_o}\right)^2 \; \cdots$$

$$\approx 1 - \frac{\Delta n_i}{n_o} .$$

Thus

$$\psi \approx \frac{2\pi}{\lambda_o n_o} \sum_{i=1}^{N} d_i (1 - \Delta n_i / n_o)$$

$$= \frac{2\pi}{\lambda_o n_o} \sum_{i=1}^{N} d_i - \frac{2\pi}{\lambda_o n_o^2} \sum_{i=1}^{N} d_i \Delta n_i .$$

Now we let k_o be the wave number corresponding to λ_o and note that the sum of the d_i is equal to L, so

$$\psi \approx \frac{k_o L}{n_o} - \frac{k_o}{n_o^2} \sum_{i=1}^{N} d_i \Delta n_i .$$

The constant first term of this expression is always present due to propagation through the distance L whether or not one is dealing with atmospheric turbulence. The fluctuating (image degrading) portion of ψ, which we will denote by ϕ, is

$$\phi = \frac{-k_0}{n_0^2} \sum_{i=1}^{N} d_i \Delta n_i .$$

We again assume that we may apply the Central Limit Theorem to the random product $d_i \Delta n_i$, so that for N very large, ϕ is approximately Gaussian where

$$e^{i\psi} = e^{i(k_0 L/n_0 + \phi)} .$$

We have now completed our simplistic physical justification for assuming lognormal intensity statistics as well as our determination that the fluctuating portion of phase at the receiver is Gaussian, and we will now consider some of the relevant experimental results.

2.1.2 Experimental Confirmation of Lognormal Intensity Statistics

There has also been considerable effort to determine the correct statistical model for amplitude or intensity by experimental measurement. Summaries of these efforts are available in Fante (1975), Strohbehn (1971), and Roddier (1981). Strohbehn (1971) reports that one of the first careful experiments, a measurement of the variance of log-intensity, was made in the Soviet Union in 1965 by Gracheva and Gurvich. Their measurements agree well with those predicted theoretically using a lognormal model for small (< 1) values of σ_{logI}. Ochs and Lawrence (1969) later measured the variance of log-amplitude and concluded that their data were in better agreement with a lognormal model than with a Rayleigh model for amplitude, which would imply that intensity is better described by lognormal statistics than by negative exponential statistics. (This Rayleigh model is due to an assumption

that the real and imaginary parts of the electric field are bivariate Gaussian with zero covariance. See Goodman (1984) for a derivation of this result in the context of laser speckle.)

Unfortunately, as Heyde (1963) and Barakat (1976) have noted, the lognormal distribution has the unusual property of not being uniquely determined by its moments. (We have presented a proof of this property in Appendix A.) Therefore as Barakat (1976) notes, it is not valid to predict a lognormal probability density function for intensity or amplitude simply based on the measurement of moments such as variance. This casts much doubt on the experimental results reported above and also upon many of the others recorded in the literature.

More recently, careful measurements have been made of the combined telescope-atmosphere modulation transfer function (MTF) for the speckle interferometry process. This transfer function has also been theoretically obtained by Korff (1973) using the lognormal model (although considerable numerical evaluation of his result is necessary) and by Dainty (1973) using a Gaussian model for complex amplitude, an approach equivalent to assuming a negative exponential intensity distribution. Chelli et al. (1979) have presented experimentally obtained MTF's for infra-red stellar speckle interferometry and have found them to be in good agreement with Korff's model. Aime et al. (1979) have also experimentally determined the telescope-atmosphere MTF and have found their results to be in better agreement with Korff's model than with the Gaussian model. These experimental results point to the validity of assuming a lognormal distribution for the

without the problems inherent in an argument based on measurements of
moments, and we consider them to be the more relevant confirmation of
our decision to use the lognormal distribution in our modelling.

2.2 Justification for Use of the Negative
Exponential Distribution for Intensity

Although the lognormal distribution for intensity seems to have
more theoretical and experimental support, the negative exponential
distribution is still widely used in calculations appearing in the
literature. This is due in part to the fact that Goodman (1984) has
developed an extensive collection of analytical results using this
distribution in connection with laser speckle. Also, Dainty (1984) has
noted that the negative exponential distribution becomes a better
assumption as seeing deteriorates, and Lee, Holmes and Kerr (1976) have
claimed that it is a valid assumption at least in the absence of
turbulence. Some years earlier, Strohbehn (1968) commented that the
Rayleigh distribution for amplitude, and thus the negative exponential
distribution for intensity, is valid for "tropospheric beyond-the-
horizon propagation or in line-of-sight propagation when the turbulent
medium is a small slab and the receiver is far from the slab." This,
however, does not describe the situation for ground-based astronomy.
Certainly, the main advantage of using negative exponential statistics
rather than lognormal statistics is that it allows one to more easily
achieve analytic solutions to many of the problems arising in astronomi-
cal imaging. We shall, however with one exception, use the lognormal
distribution for all of our calculations in subsequent chapters.

CHAPTER 3

REVIEW OF SPECKLE IMAGING

At this point, we have stated that the atmosphere degrades images of objects viewed through it by distributing a point source such as a star into a speckle pattern, and we have determined a statistical model for the intensity of an optical wave which has passed through the atmosphere. We now wish to discuss the previous work that has been done on the problem of obtaining true images of objects viewed through the atmosphere.

This problem has received considerable attention, especially in the last fifteen years since the advent of speckle interferometry. In the remainder of this chapter, we will review some of the major advances in speckle imaging. In section 3.1, we will briefly discuss short exposure images followed by comments on conventional long exposure and speckle interferometry in sections 3.2 and 3.3. Then sections 3.4 through 3.8 will be devoted to short reviews of various techniques used to extract more information from the output of speckle interferometry or from the short exposure images themselves. There are, of course, many other techniques which will not be covered in this chapter, and we refer the reader to Dainty (1984) or to Bates (1982) for a more thorough review.

3.1 The Short Exposure Image

A short exposure or "instantaneous" image refers to an image
for which the fluctuations of the atmosphere may be considered to be
frozen; that is, the exposure time is on the order of a few hundredths
of a second. We shall consider such images in the context of a linear
systems model (Figure 3.1) and thus write the following equation

$$i(x,y) = o(x,y) ** t(x,y) \qquad (3.1)$$

where $i(x,y)$ is the short exposure image intensity, $o(x,y)$ is the
object intensity, $t(x,y) = a(x,y) ** p(x,y)$ is the combined
atmosphere/telescope point spread function, and ** denotes convolution.

This equation may be equivalently expressed in the Fourier
domain by

$$I(u,v) = O(u,v)T(u,v) \qquad (3.2)$$

where $I(u,v)$ and $O(u,v)$ are respectively the Fourier transforms of the
image and object intensities and $T(u,v)$ is the combined
atmosphere/telescope transfer function. Since we are dealing with
astronomical imaging, it should be noted here that although Equations
(3.1) and (3.2) are written in the spatial and spatial frequency
domains, it is more appropriate to interpret x and y as angles of arc
and u and v as angular frequency, that is, arc sec^{-1}.

Thus our problem is, given $i(x,y)$ (or equivalently, $I(u,v)$), to
determine $o(x,y)$ or the best possible image of $o(x,y)$ given our optical
system. In the short exposure case, one may not simply use the point

Point
Source
Object

Turbulence

Distorted
Wavefront

Optical
System

Image

(A)

$o(x,y) \longrightarrow$ Atmosphere
$psf : a(x,y)$

$\longrightarrow$ Optics
(Telescope)
$psf : p(x,y)$

$\longrightarrow i(x,y) = o(x,y)**$
$a(x,y)** p(x,y)$
$= o(x,y)** t(x,y)$

Object
Intensity

Image
Intensity

(B)
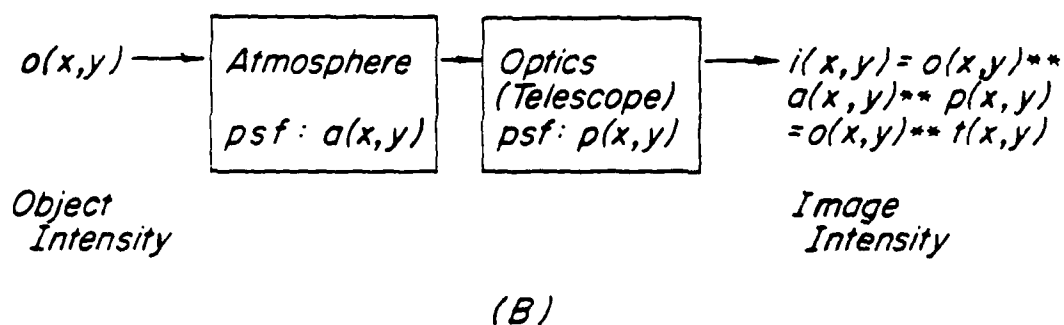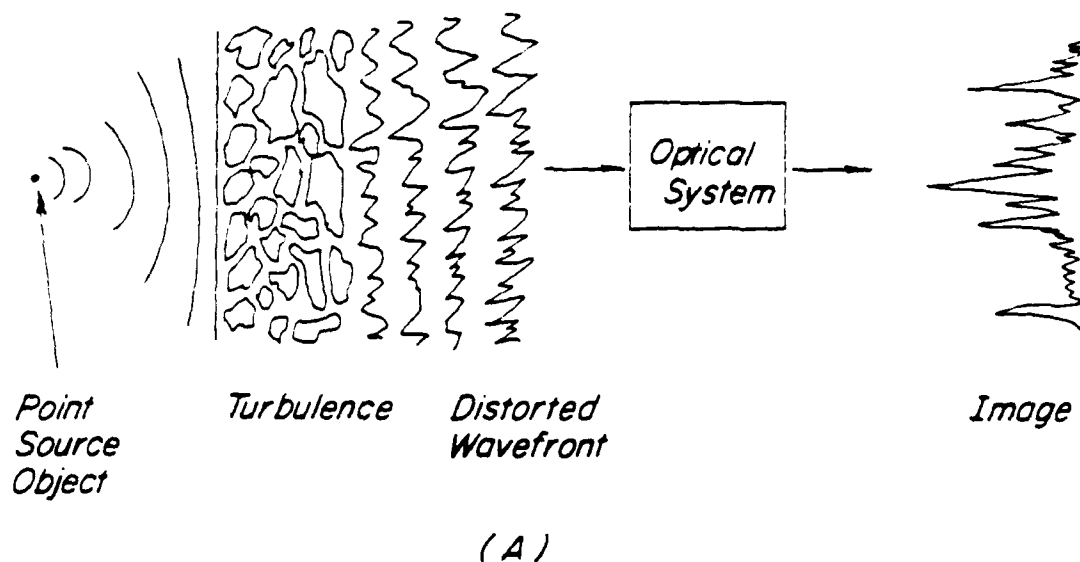
Figure 3.1. Linear system model of image formation through the atmos-
phere. -- (a) Pictorial description of image formation;
and (b) Block diagram of the linear systems model of image
formation.

spread function $t(x,y)$ or the transfer function $T(u,v)$ to restore the image because due to the action of the atmosphere, $t(x,y)$ and $T(u,v)$ are random, and information is available only for the average quantities, $\langle t(x,y) \rangle$ or $\langle T(u,v) \rangle$. This would imply that some form of averaging of the short exposure images is necessary. In section 3.2, we will discuss one form of averaging, the long exposure image, and see that it also has serious drawbacks in terms of loss of high frequency information. We will see that a better approach is the shift-and-add algorithm of section 3.8, which consists of averaging properly registered short exposure images and retains information out to the diffraction limit.

3.2 Long Exposure Imaging

Conventional long exposure imaging may be regarded as a sum of a series of short exposures, so the governing equation for this process in the Fourier domain is as follows

$$\langle I(u,v) \rangle = O(u,v)\langle T(u,v) \rangle \qquad (3.3)$$

where $\langle . \rangle$ denotes an ensemble average, $\langle I(u,v) \rangle$ is the Fourier transform of the long exposure image, and $\langle T(u,v) \rangle$ is the long exposure transfer function.

Earlier analyses of the long exposure transfer function were performed by Hufnagel and Stanley (1964) and Fried (1966), and Fried has shown that long exposure images retain substantially less high frequency information than do the individual short exposures, thus yielding a blurred or smoothed result. Intuitively, we may see this by

recalling that $T(u,v)$ is random due to atmospheric effects and may thus be positive or negative (or perhaps complex-valued) at high frequencies. Summing the individual $T(u,v)$'s, as in Equation (3.3), will then result in suppression of high frequencies, so that even if $\langle T(u,v)\rangle$ is known, one cannot adequately reconstruct $o(x,y)$ due to this lack of high frequency information in the image data.

For further discussion of the long exposure transfer function and determination of its functional form, see Fried (1966), or Hufnagel and Stanley (1964) or the review articles Dainty (1984) or Roddier (1981).

3.3 Speckle Interferometry

It was to combat this loss of high frequency information that Labeyrie (1970) introduced the technique which became known as speckle interferometry (Gezarie, Labeyrie, and Stachnik, 1972). Where long exposure imaging is equivalent to summing a series of short exposures and thus their Fourier transforms, speckle interferometry consists of the addition of the squared magnitudes of the short exposure image transforms (i.e., spatial power spectra) as follows

$$
\begin{aligned}
\phi_I(u,v) &= \langle |I(u,v)|^2 \rangle \\
&= |O(u,v)|^2 \langle |T(u,v)|^2 \rangle \\
&= \phi_0(u,v) \langle |T(u,v)|^2 \rangle
\end{aligned}
\tag{3.4}
$$

where $\phi_I(u,v)$ and $\phi_0(u,v)$ are respectively the image and object average (spatial) power spectra and $|.|^2$ denotes the squared magnitude of a complex-valued quantity. This averaging of $|T(u,v)|^2$, which is always

a non-negative quantity, prevents the loss of high frequencies, which was the main drawback of long exposure imaging.

Korff (1973) has derived an analytic expression for $\langle |T(u,v)|^2 \rangle$ based on lognormal intensity statistics, which agrees closely with Fried's results (Fried, 1966). However, this expression requires considerable numerical evaluation, which limits its usefulness. Dainty (1984) has shown that a good approximation for $\langle |T(u,v)|^2 \rangle$ is

$$\langle |T(u,v)|^2 \rangle \simeq |\langle T(u,v) \rangle|^2 + kT_D(u,v)$$

where $\langle T(u,v) \rangle$ is the long exposure transfer function, $T_D(u,v)$ is the diffraction-limited optical transfer function of the telescope, and $k < 1$ is a constant inversely related to the number of speckles in the image.

Now, assuming that information about the transfer function $\langle |T(u,v)|^2 \rangle$ is available, either from a reference star (point source) or from one the theoretical derivations mentioned above, $\Phi_0(u,v)$ may be recovered from Equation (3.4). Inverse transforming yields the average spatial autocorrelation

$$\langle R_s(x,y) \rangle = F^{-1}\{\Phi_0(u,v)\}$$
$$= \langle i(x,y) \ast\ast i(x,y) \rangle$$

where $\ast\ast$ denotes autocorrelation.

The limitation of this method is that one obtains only autocorrelation or power spectrum images rather than true images of the object. Phase information is lost, and as is noted in Oppenheim and

Lim (1974), this information is generally more important than amplitude information for signal reconstruction. Bates (1982) has presented a comprehensive review of what has become known as the "phase problem," the inability (in general) to uniquely determine an object $o(x,y)$ from its power spectrum. In certain special cases, however, such as a centro-symmetric object, the Fourier transform is purely real and determination of $o(x,y)$ is possible. Also, other useful object information, such as the distance between two point sources (e.g., double stars) or an estimate of the spatial extent of the object, may be recovered from the autocorrelation data.

Since the introduction of speckle interferometry in 1970, much effort has been centered on methods of recovering an object from its autocorrelation or power spectrum, and we will discuss several of these algorithms in the following sections.

3.4 Speckle Holography

The technique of speckle holography (Bates, Gough and Napier, 1973; Gough and Bates, 1974) demonstrates that the object $o(x,y)$ may be reconstructed from interferometry data, provided an unresolvable reference object (point source) such as a star is present. In this case, following the notation of Dainty (1984), the object may be represented as a sum of two parts

$$o(x,y) = \delta(x)\delta(y) + o_1(x-x_1, y-y_1)$$

where $\delta(x)\delta(y)$ is the Dirac delta function denoting the reference object and $o_1(x-x_1, y-y_1)$ centered at (x_1, y_1) is the object of interest.

If $x_1 > 3x_o/2$ and $y_1 > 3y_o/2$, where x_o and y_o are the extent of $o_1(x,y)$ in the x and y directions, respectively, then the spatial autocorrelation $R_o(x,y)$ separates into three distinct parts

$$R_o(x,y) = o_1(-(x+x_1),-(y+y_1)) +$$

$$[\delta(x)\delta(y)\circledast\circledast\delta(x)\delta(y) + o_1(x,y)\circledast\circledast o_1(x,y)] +$$

$$o_1((x-x_1),(y-y_1)) .$$

That is, the central component of $R_o(x,y)$ consists of the autocorrelations of the two parts of the object, and the outer components consist of their cross-correlations. One of these outer components will be the correctly oriented object of interest and the other will be a 180° rotation, so the object can be reconstructed within this rotational ambiguity.

Practically, the object may not always meet the separation requirements $x_1 > 3x_o/2$ and $y_1 > 3y_o/2$ even when a point source is present, so that the parts of $R_o(x,y)$ are not completely distinct. Liu and Lohmann (1973) have suggested a procedure similar to that of speckle holography in which they utilize the fact that the long exposure image does contain low frequency phase information. This information is incorporated into their algorithm by using the long exposure image as a mask to select the correct components of $R_o(x,y)$ and eliminate autocorrelation terms.

3.5 Speckle Masking

Related to speckle holography is the speckle masking technique developed by Weigelt (Weigelt, 1977; Weigelt and Wirnitzer, 1983), who has suggested that it may be especially useful for imaging double stars. The major difference between speckle holography and speckle masking is that in the former, an unresolvable reference object is required to be present while in the latter, each speckle image is preprocessed nonlinearly to create a synthetic reference object.

To implement this algorithm, one first calculates the average image triple correlation

$$\langle [i(x,y)i(x-m_x,y-m_y)] \circledast \circledast i(x,y) \rangle \qquad (3.5)$$

where (m_x,m_y) is the masking vector, e.g., in the case of imaging a double star, (m_x,m_y) is the separation which may be obtained from interferometry data. Weigelt has then computed a correction term (Weigelt and Wirnitzer, 1983), which allows the calculation of the object triple correlation

$$\langle [o(x,y)o(x-m_x,y-m_y)] \circledast \circledast o(x,y) \rangle$$

from Equation (3.5). The object $o(x,y)$ may then be reconstructed provided that (m_x,m_y) was properly chosen to give

$$[o(x,y)o(x-m_x,y-m_y)] = \delta(x)\delta(y).$$

3.6 Knox-Thompson Method

Knox and Thompson (1974) have proposed a method that involves the autocorrelation of the Fourier transform of the speckle images rather than the image power spectra. The algorithm calculates

$$\langle I(u_1,v_1)I^*(u_2,v_2)\rangle = O(u_1,v_1)O^*(u_2,v_2)\langle T(u_1,v_1)T^*(u_2,v_2)\rangle$$
$$= O(u,v)O^*(u+\Delta u,v+\Delta v)\langle T(u,v)T^*(u+\Delta u,v+\Delta v)\rangle$$

where $\Delta u = u_2-u_1$ and $\Delta v = v_2-v_1$ are small compared to the correlation length of $I(u,v)$. Denoting the phase of $O(u,v)$ by $\phi(u,v)$ and the phase of $T(u,v)$ by $\theta(u,v)$, we may write

$$\langle I(u_1,v_1)I^*(u_2,v_2)\rangle = |O(u,v)||O(u+\Delta u,v+\Delta v)|$$
$$* \exp(i[\phi(u,v) - \phi(u+\Delta u,v+\Delta v)])$$
$$* |T(u,v)||T(u+\Delta u,v+\Delta v)|$$
$$* \exp(i[\theta(u,v) - \theta(u+\Delta u,v+\Delta v)]).$$

$$(3.6)$$

Dainty (1984) has shown that the phase difference $[\theta(u,v)-\theta(u+\Delta u,v+\Delta v)] \approx 0$, so that the phase of the right-hand side of Equation (3.6) is approximately $[\phi(u,v) - \phi(u+\Delta u,v+\Delta v)]$. Thus we may generate a grid of phase differences for the object and may obtain the relative phase for each point in the Fourier transform of the object by summing the phase differences between it and an arbitrary reference, say, the origin. Since the modulus of the transform is available from the interferometry data, object reconstruction is then possible (within a position ambiguity since only relative phase may be computed).

3.7 Fienup's Iterative Algorithms

Fienup (1978, 1979) has suggested an iterative approach to obtain object phase information from the modulus of the Fourier transform $O(u,v)$, which is known from speckle interferometry. His approach, called the error reduction method (Figure 3.2) because the mean-squared error decreases at each iteration, is a modified version of the Gerchberg-Saxton algorithm (Gerchberg and Saxton, 1972) and consists of simply changing the object constraints in this well-known method.

Beginning at the kth iteration with the object estimate $\hat{o}_k(x,y)$, this estimate is Fourier transformed, yielding $\hat{O}_k(u,v) = |\hat{O}_k(u,v)|\exp[i\phi_k(u,v)]$. The Fourier domain constraint consists of replacing $|\hat{O}_k(u,v)|$ with the known modulus $|O(u,v)|$. The quantity $|O(u,v)|\exp[i\phi_k(u,v)]$ is then inverse Fourier transformed producing the image $\hat{o}_k'(x,y)$, which is then forced to obey the spatial domain constraints. The principal spatial domain constraint is non-negativity, although other a priori information about the object may also be included, e.g., we know the object autocorrelation from speckle interferometry and the object diameter cannot exceed half the extent of the autocorrelation. Thus the new object estimate

$$\hat{o}_{k+1}'(x,y) = \begin{cases} \hat{o}_k'(x,y), & \text{constraints satisfied} \\ \\ 0, & \text{constraints not satisfied} \end{cases}$$

$$\hat{o}_k(x,y) \longrightarrow \boxed{F\big\{ \quad \big\}} \longrightarrow \hat{O}_k(u,v) = |\hat{O}_k(u,v)| e^{i\phi_k(u,v)}$$

$$\boxed{\begin{array}{c} \textit{Satisfy} \\ \textit{Object} \\ \textit{Constraints} \end{array}} \qquad \boxed{\begin{array}{c} \textit{Satisfy} \\ \textit{Fourier} \\ \textit{Constraints} \end{array}}$$

$$\hat{o}_k{}'(x,y) \longleftarrow \boxed{F^{-1}\big\{ \quad \big\}} \longleftarrow \hat{O}_k{}'(u,v) = |O(u,v)| e^{i\phi_k(u,v)}$$
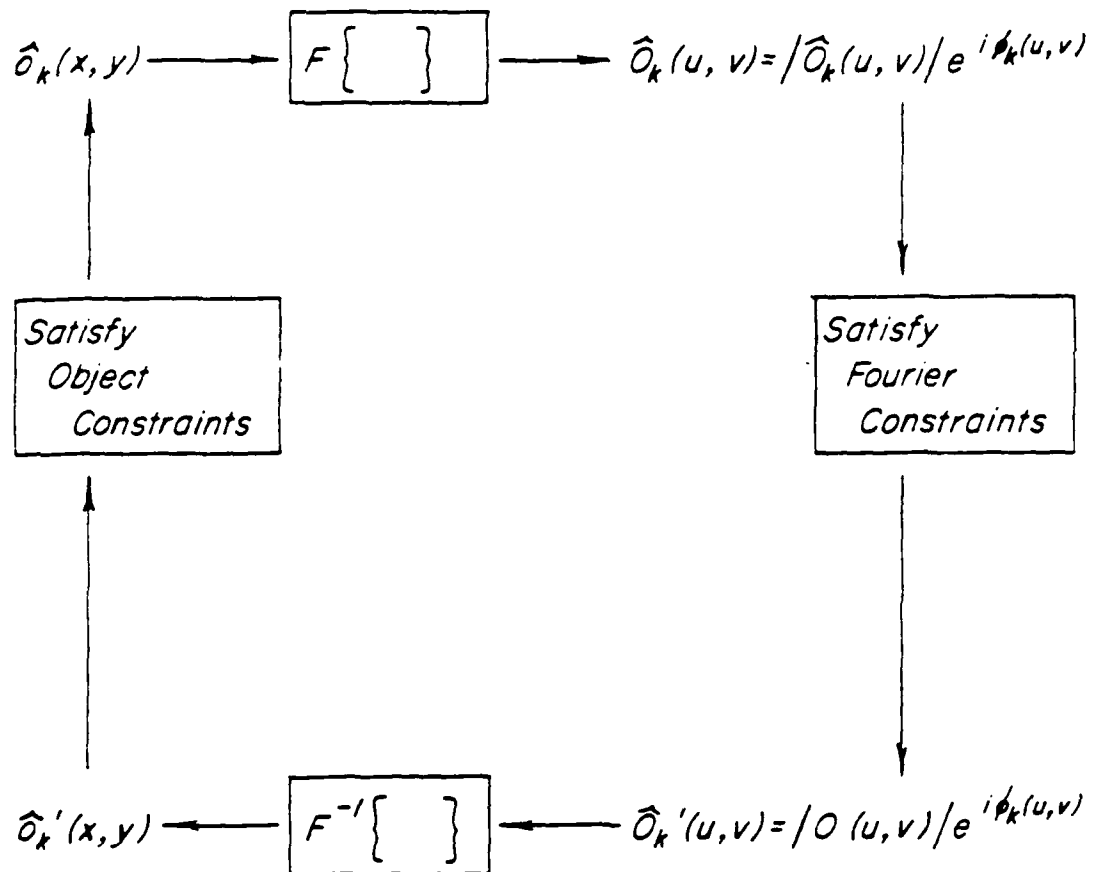
Figure 3.2. Fienup's error reduction method.

is formed. This entire procedure may be started with an estimate $\phi_1(u,v)$ or a random $\phi_1(u,v)$ if a better estimate is unavailable.

In practice, Fienup has found that although convergence is initially rapid, it soon becomes extremely slow, requiring an impractical number of iterations for a good reconstruction.

To combat this problem, he has developed the input-output approach (Figure 3.3) in which the new object estimate is a modification of the previous one

$$\hat{o}_{k+1}(x,y) = \begin{cases} \hat{o}_k(x,y), & \text{constraints satisfied} \\ \\ \hat{o}_k(x,y) - a\hat{o}_k'(x,y), & \text{constraints not satisfied} \end{cases}$$

where a is a constant. He has further found by experimentation that the swiftest convergence is achieved by periodically varying the method of forming $\hat{o}_{k+1}(x,y)$ after every few iterations.

3.8 Shift-and-Add

Unlike the methods previously discussed, the shift-and-add algorithm and the related method which will be examined in this section do not attempt to reconstruct the object from its power spectrum or autocorrelation or to use other information about the Fourier modulus, image separation, or image extent which are made available by speckle interferometry. Instead, they attempt to obtain a true image of the object directly from the short exposure images.

Shift-and-add is an extension of a method previously developed by Lynds, Worden and Harvey (1976) (or Worden, Lynds and Harvey, 1976),

$$\hat{O}_k(x,y) \longrightarrow \boxed{F\{\ \}} \longrightarrow \hat{O}_k(u,v) = |\hat{O}_k(u,v)| e^{i\sigma_k(u,v)}$$

Form New Input

Satisfy Fourier Constraints

$$\hat{O}_k'(x,y) \longleftarrow \boxed{F^{-1}\{\ \}} \longleftarrow \hat{O}_k'(u,v) = |O(u,v)| e^{i\sigma_k(u,v)}$$
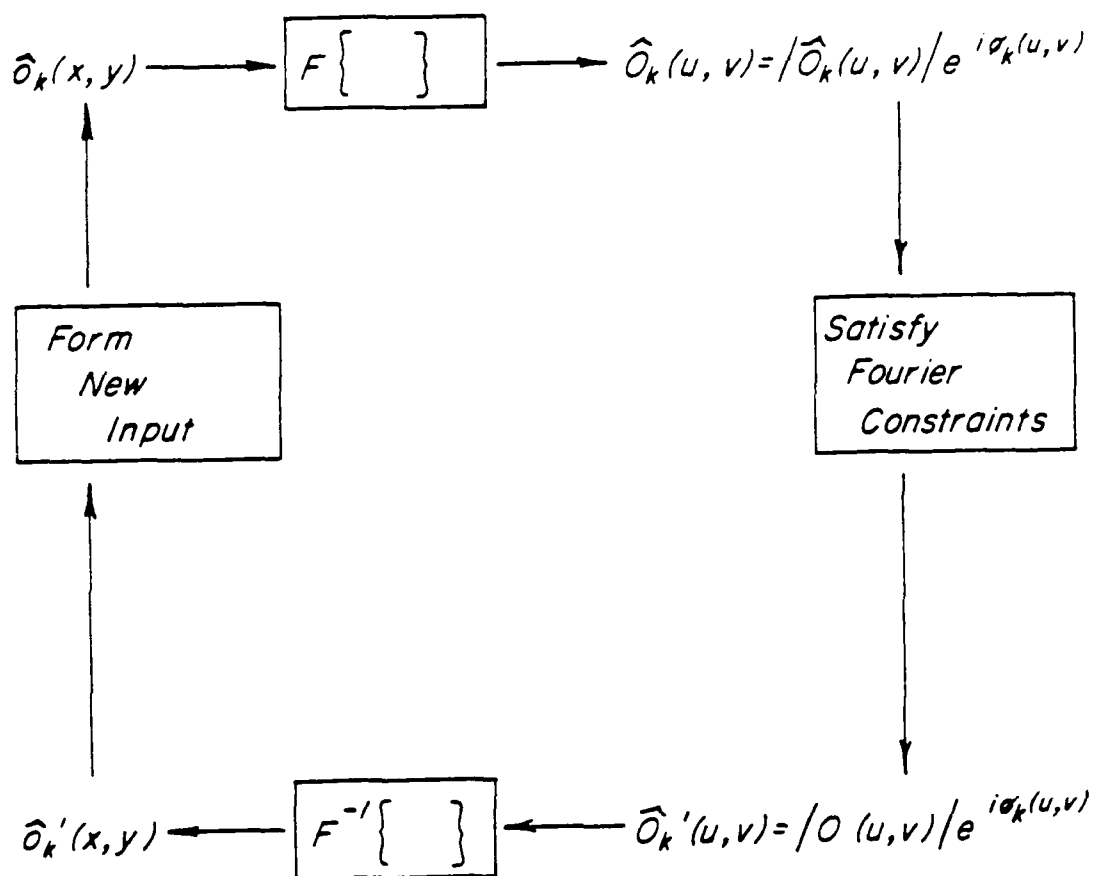
Figure 3.3. Fienup's input-output method.

who realized that each speckle of a short exposure image is itself a distorted image of the object. Their procedure involves the identification and superposition of the brightest speckles, thus creating an improved estimate of the object.

According to Bates (1982), this procedure is limited by the fact that many celestial objects are so faint that a typical short exposure image contains few speckles, and he and Cady (Bates and Cady, 1980; Cady and Bates, 1980) have extended the method to compensate for this problem. In their approach, each short exposure is shifted so that its brightest speckle is located at the origin, and all such shifted images are summed, thus the name shift-and-add. Assuming that this processing is also carried out for a reference star, the shift-and-add image of the object of interest may be deconvolved using the shift-and-add image of the reference star as a point spread function.

The beauty of this method is in its simplicity and ease of implementation as compared to the methods previously discussed, and according to Bates (1982), it may be digitally implemented in real time. Further improvement in the output image has been obtained (Bates, 1982) by a method called adjusted shift-and-add, in which each pixel is multiplied by the value of the brightest pixel before the summing operation, and Bates and Robinson (1982) have devised a slightly more complicated version of shift-and-add, which they have found useful in ultrasonic imaging.

We, however, will restrict ourselves to the original, simple version of the algorithm and will present a theoretical analysis of the method and various simulation results in the following chapters.

CHAPTER 4

ANALYSIS OF THE SHIFT-AND-ADD ALGORITHM
FOR LOGNORMAL INTENSITY STATISTICS

The simplicity of the shift-and-add algorithm described in section 3.8 leads us to ask why this method forms an improved estimate of the object. This question has previously been addressed in some detail by Hunt, Fright and Bates (1983) for negative exponential statistics. Here we shall present an analysis (which draws heavily on the earlier one for notation and modelling) using the lognormal intensity statistics which were justified in Chapter 2.

To facilitate our discussion, we will now adopt the standard mathematical model of the speckle process. We are changing notation from that of section 3.1 to be more consistent with existing shift-and-add literature. This model assumes that image exposure time is so short that the atmospheric amplitude and phase variations are essentially frozen and also makes the assumption of isoplanaticity, i.e., the assumption that the atmospheric point spread function is shift invariant. With no loss of generality and to simplify notation, we shall restrict our analysis to one dimension. We denote the mth speckle image of the object $f(x)$ by

$$s_m(x) = h_m(x)*f(x) + c_m(x) \qquad (4.1)$$

where m is a time index, $h_m(x)$ is the mth short exposure speckle point spread function, * indicates convolution, and $c_m(x)$ is a general contamination term that includes all other degradations, i.e., recording noise, system nonlinearities, photon noise.

Within this framework, the shift-and-add process is easily described. It consists of finding the maximum value of each spatial image and the spatial coordinate ξ_m at which it occurs, translating the image by ξ_m so that the maximum value is now located at the origin of coordinates, and summing all such translated images. For M speckle images, the shift-and-add result $s(x)$ is expressed by

$$s(x) = 1/M \sum_{m=1}^{M} s_m(x + \xi_m) \qquad (4.2)$$

With this model established, we proceed to explore our original question: why is $s(x)$ a better estimate of $f(x)$ than are any of the individual frames $s_m(x)$?

We first consider this question qualitatively. According to Bates and Cady (1980), the brightest portion of each speckle image $s_m(x)$ is likely to be a distorted version of the brightest portion of $f(x)$. Thus because of the linear nature of the degradation model and of the shift-and-add process, superposition of distorted versions of the brightest portions of $f(x)$ necessarily implies the correctly registered superposition of all other parts of $f(x)$.

4.1 Derivation of the Point Spread Function

Now we perform a more rigorous analysis of the shift-and-add method by considering the case of a single point source (Dirac delta

function) object and finding an overall point spread function for the degradation plus shift-and-add processing. We will at this point ignore the contamination term $c_m(x)$ so that Equation (4.1) becomes

$$s_m(x) = h_m(x).$$

Thus the overall point spread function $h(x)$ is

$$h(x) = s(x) = 1/M \sum_{m=1}^{M} s_m(x + \xi_m) = 1/M \sum_{m=1}^{M} h_m(x + \xi_m)$$

as is obvious from the linearity of the method.

Following the derivation in Hunt, Fright and Bates (1983), we introduce a change of notation

$$\sigma_m(x) = s_m(x + \xi_m),$$

i.e., the $\sigma_m(x)$ are simply the speckle images translated so that the maximum value is found at the origin. This leads to the shift-and-add result

$$s(x) = 1/M \sum_{m=1}^{M} \sigma_m(x).$$

At each fixed x, this is simply a sum of M random variables, where we note that for $|x|$ very small, correlation in the images necessitates that $\sigma_m(x) \simeq \sigma_m(0)$, while for $|x|$ larger than the correlation length of the speckle process, $\sigma_m(x)$ and $\sigma_m(0)$ are effectively independent.

Therefore, for large M,

$$\lim_{M \to \infty} s(x) = \lim_{M \to \infty} 1/M \sum_{m=1}^{M} \sigma_m(x) \; \to \; E[\sigma_m(x)|\sigma_m(0)]$$

where $E[\cdot]$ denotes expectation, and we will assume M large enough that

$$\lim_{M \to \infty} s(x) = E[\sigma_m(x) | \sigma_m(0)] \qquad (4.3)$$

in the following calculations. We also define for future use the quantity s_{max}:

$$s_{max} = 1/M \sum_{m=1}^{M} \sigma_m(0)$$

or for M large, we may assume $s_{max} = E[\sigma_m(0)]$.

Again, following the notation of Hunt, Fright and Bates (1983), we let

$$I_1 = \sigma_m(0)$$
$$I_2 = \sigma_m(x).$$

As we are assuming lognormal intensity statistics, I_1 is governed by the probability density function

$$p(I_1) = \frac{1}{I_1 \sigma_1 \sqrt{2\pi}} \exp\left\{ \frac{-[\log I_1 - \mu_1]^2}{2\sigma_1^2} \right\} ,$$

and similarly for I_2. In this expression, log denotes the natural logarithm (base e), and μ_1 and σ_1^2 are respectively the mean and variance of the normally distributed random variable $\log I_1$.

To calculate the expectation in Equation (4.3), we need the joint density function for I_1 and I_2, which we will assume to be jointly lognormal:

$$p(I_1, I_2) = \frac{1}{I_1 I_2 2\pi \sigma_1 \sigma_2 \sqrt{1-\rho^2}} \exp\left\{\frac{\left[\left(\frac{\log I_1 - \mu_1}{\sigma_1}\right)^2 + \left(\frac{\log I_2 - \mu_2}{\sigma_2}\right)^2 - 2\rho\left(\frac{\log I_1 - \mu_1}{\sigma_1}\right)\left(\frac{\log I_2 - \mu_2}{\sigma_2}\right)\right]}{2(1-\rho^2)}\right\}$$

(4.4)

where ρ is the correlation coefficient for the associated normal random variables $\log I_1$ and $\log I_2$. We have made such an assumption because it is necessary in order to achieve analytic results although we are well aware that it is not generally valid to do so simply given that the variables I_1 and I_2 are both marginally lognormal. Also we note that the x dependence of ρ and of μ_2 is not explicitly stated in Equation (4.4), and we will comment further on this later.

Then with our previous assumptions, we have

$$p(I_2|I_1) = \frac{p(I_2, I_1)}{p(I_1)}$$

$$= \frac{1}{I_2 \sigma_2 \sqrt{2\pi(1-\rho^2)}} \exp\left\{\frac{-\left[\left(\frac{\log I_1 - \mu_1}{\sigma_1}\right)^2 \rho^2 + \left(\frac{\log I_2 - \mu_2}{\sigma_2}\right)^2 - 2\rho\left(\frac{\log I_1 - \mu_1}{\sigma_1}\right)\left(\frac{\log I_2 - \mu_2}{\sigma_2}\right)\right]}{2(1-\rho^2)}\right\}$$

and we may write the desired expectation

$$E[I_2|I_1] = \int_0^\infty I_2 p(I_2|I_1) dI_2$$

$$= \frac{1}{\sigma_2 \sqrt{2\pi(1-\rho^2)}} \int_0^\infty \exp\left\{\frac{-\left[\left(\frac{\log I_1 - \mu_1}{\sigma_1}\right)^2 \rho^2 + \left(\frac{\log I_2 - \mu_2}{\sigma_2}\right)^2 - 2\rho\left(\frac{\log I_1 - \mu_1}{\sigma_1}\right)\left(\frac{\log I_2 - \mu_2}{\sigma_2}\right)\right]}{2(1-\rho^2)}\right\}$$

(4.5)

This integral is evaluated in Appendix B, giving

$$E[I_2 | I_1] = I_1^{\rho \sigma_2 / \sigma_1} \exp[\mu_2 - \rho \mu_1 \sigma_2 / \sigma_1 + \sigma_2^2 (1 - \rho^2)/2] \qquad (4.6)$$

To give some intuitive feel for the expression, we will evaluate it for some extreme values of the parameters. Also needed for this evaluation are the following relations (see Appendix A) for any lognormal random variable I:

$$\langle I \rangle = E[I] = e^{\mu + \sigma^2/2}$$

and

$$\sigma_I^2 = e^{2\mu + \sigma^2} (e^{\sigma^2} - 1)$$

$$= \langle I \rangle^2 (e^{\sigma^2} - 1)$$

where as before

$$\mu = E[\log I]$$

$$\sigma^2 = \text{var}[\log I].$$

First we consider the case where I_2 and I_1 are completely uncorrelated. Recalling that $I_1 = \sigma_m(0)$ and $I_2 = \sigma_m(x)$, this is simply the case of $|x| \gg 0$. This corresponds to the parameter value $\rho = 0$. Thus Equation (4.6) becomes

$$E[I_2 | I_1] = e^{\mu_2 + \sigma_2^2/2} = \langle I_2 \rangle$$

which is exactly what one intuitively expects.

Next we consider the case of I_2 and I_1 perfectly correlated.
i.e., $|x| = 0$. This corresponds to the parameter value $\rho = 1$. For
this case, it is also completely reasonable to make the further
assumption that $\mu_1 = \mu_2$ and $\sigma_1^2 = \sigma_2^2$. Then evaluation of Equation (4.6)
yields

$$E[I_2|I_1] = I_1$$

which accords exactly with intuition.

At this point we observe that Equation (4.6) is entirely
specified by parameters associated with the normal distributions of log
I_1 and log I_2. We shall assume that the speckle images are spatially
stationary, or at least wide-sense stationary, an assumption actually
valid only near the origin (or only locally), which implies a constant
mean and variance

$$\langle I_1 \rangle = \langle I_2 \rangle = \langle I \rangle$$

$$\sigma_{I_1}^2 = \sigma_{I_2}^2 = \sigma_I^2$$

which in turn implies

$$\mu_1 = \mu_2 = \mu$$

$$\sigma_1^2 = \sigma_2^2 = \sigma^2.$$

Having made this assumption, our further analysis will be strictly
valid only in the region of $|x| = 0$. Since we are particularly

interested in this region--to see how closely s(x) resembles the

original object $\hat{s}(x)$--our results should yield the desired information.

Returning to our notation of $\sigma_m(0)$ and $\sigma_m(x)$ rather than I_1 and I_2, we now have

$$E[\sigma_m(x) | \sigma_m(0)] = \sigma_m(0)^{\rho} \exp[\mu - \rho\mu + \sigma^2(1-\rho^2)/2]$$

$$= \sigma_m(0) \langle I \rangle^{1-\rho} \exp[\frac{\rho(1-\rho)}{2}\sigma^2] \qquad (4.7)$$

and our next step is to relate $\rho = \rho(x)$, the correlation coefficient of $\log \sigma_m(0)$ and $\log \sigma_m(x)$, to $r(x)$, the correlation coefficient of $\sigma_m(0)$ and $\sigma_m(x)$. By definition,

$$r(x) = \frac{\mathrm{cov}[I_2, I_1]}{\sigma_{I_2}\sigma_{I_1}}$$

$$= \frac{E[I_1 I_2] - E[I_1]E[I_2]}{\sigma_{I_1}\sigma_{I_2}}$$

so we will now determine the quantity $E[I_1 I_2]$. We make the same assumption that I_1 and I_2 are jointly lognormally distributed as was made in the calculation of $E[I_2 | I_1]$. Thus

$$E[I_1 I_2] = \int_0^\infty \int_0^\infty I_2 I_1 p(I_2, I_1) dI_2 dI_1$$

$$= \frac{1}{2\pi\sigma_1\sigma_2\sqrt{1-\rho^2}} \int_0^\infty \int_0^\infty \exp\left\{\frac{\left[\left(\frac{\log I_1 - \mu_1}{\sigma_1}\right)^2 + \left(\frac{\log I_2 - \mu_2}{\sigma_2}\right)^2 - 2\rho\left(\frac{\log I_1 - \mu_1}{\sigma_1}\right)\left(\frac{\log I_2 - \mu_2}{\sigma_2}\right)\right]}{2(1-\rho^2)}\right\} dI_2 dI_1$$

This integral is evaluated in Appendix B, giving

39

$$E[I_1 I_2] = \langle I_2 \rangle \langle I_1 \rangle e^{\rho(x)\sigma_1 \sigma_2}$$

so that

$$r(x) = \frac{\langle I_2 \rangle \langle I_1 \rangle [e^{\rho(x)\sigma_1 \sigma_2} - 1]}{\sigma_{I_1} \sigma_{I_2}}$$

$$= \frac{\langle I_2 \rangle \langle I_1 \rangle [e^{\rho(x)\sigma_1 \sigma_2} - 1]}{\langle I_2 \rangle \langle I_1 \rangle \sqrt{(e^{\sigma_1^2} - 1)(e^{\sigma_2^2} - 1)}} .$$

Making our same stationarity assumptions, which imply that $\sigma_1 = \sigma_2 = \sigma$, we obtain

$$r(x) = \frac{e^{\rho(x)\sigma^2} - 1}{e^{\sigma^2} - 1}$$

so that

$$\rho = \rho(x) = 1/\sigma^2 \log[1 + r(x)(e^{\sigma^2} - 1)]$$

Now

$$\sigma_I^2 = \langle I \rangle^2 [e^{\sigma^2} - 1].$$

so

$$\sigma^2 = \log[1 + \sigma_I^2/\langle I \rangle^2]$$

and after some algebraic manipulation

$$\rho = \rho(x) = \frac{\log R(x) - \log \langle I \rangle^2}{\log R(o) - \log \langle I \rangle^2}$$

where $R(x)$ denotes autocorrelation. Assuming ergodicity, $R(x) = R_s(x)$, the spatial autocorrelation of the speckle image.

Substitution in Equation (4.7) and further algebraic simplification yields

$$E[\sigma_m(x)|\sigma_m(0)] = \sigma_m(0)^{-\left[\dfrac{\log\langle I\rangle^2}{\log R_s(0)-\log\langle I\rangle^2}\right]}$$

$$\times\; R_s(x)^{\frac{1}{2}\left[\dfrac{2\log\sigma_m(0)+\log R_s(0)-\log R_s(x)}{\log R_s(0)-\log\langle I\rangle^2}\right]}$$

and since we are implying that $M \rightarrow \infty$ by using the expectation, we have the desired result

$$\lim_{M\to\infty} s(x) = E[\sigma_m(x)|\sigma_m(0)]$$

$$= s_{max}^{-\left[\dfrac{\log\langle I\rangle^2}{\log R_s(0)-\log\langle I\rangle^2}\right]}$$

$$\times\; R_s(x)^{\frac{1}{2}\left[\dfrac{2\log s_{max}+\log R_s(0)-\log R_s(x)}{\log R_s(0)-\log\langle I\rangle^2}\right]}.$$

$$(4.8)$$

The obvious question at this point is how to characterize $R_s(x)$ in order to give this complicated expression some meaning. There appear to be three options available. First, one may actually measure $R_s(x)$ from the speckle images. We had no real data available but have included plots of $s_m(x)$ and the corresponding $R_s(x)$ taken from images simulated by the method of section 5.1 in Figures 4.1 and 4.2.

Korff (1973) has developed an expression for $\langle|T(f)|^2\rangle$ which is the Fourier transform of $\langle R_s(x)\rangle$. Calculating $\langle|T(f)|^2\rangle$ and inverse Fourier transforming is our second option. Unfortunately, evaluation of $\langle|T(f)|^2\rangle$ requires extensive numerical computation and specific
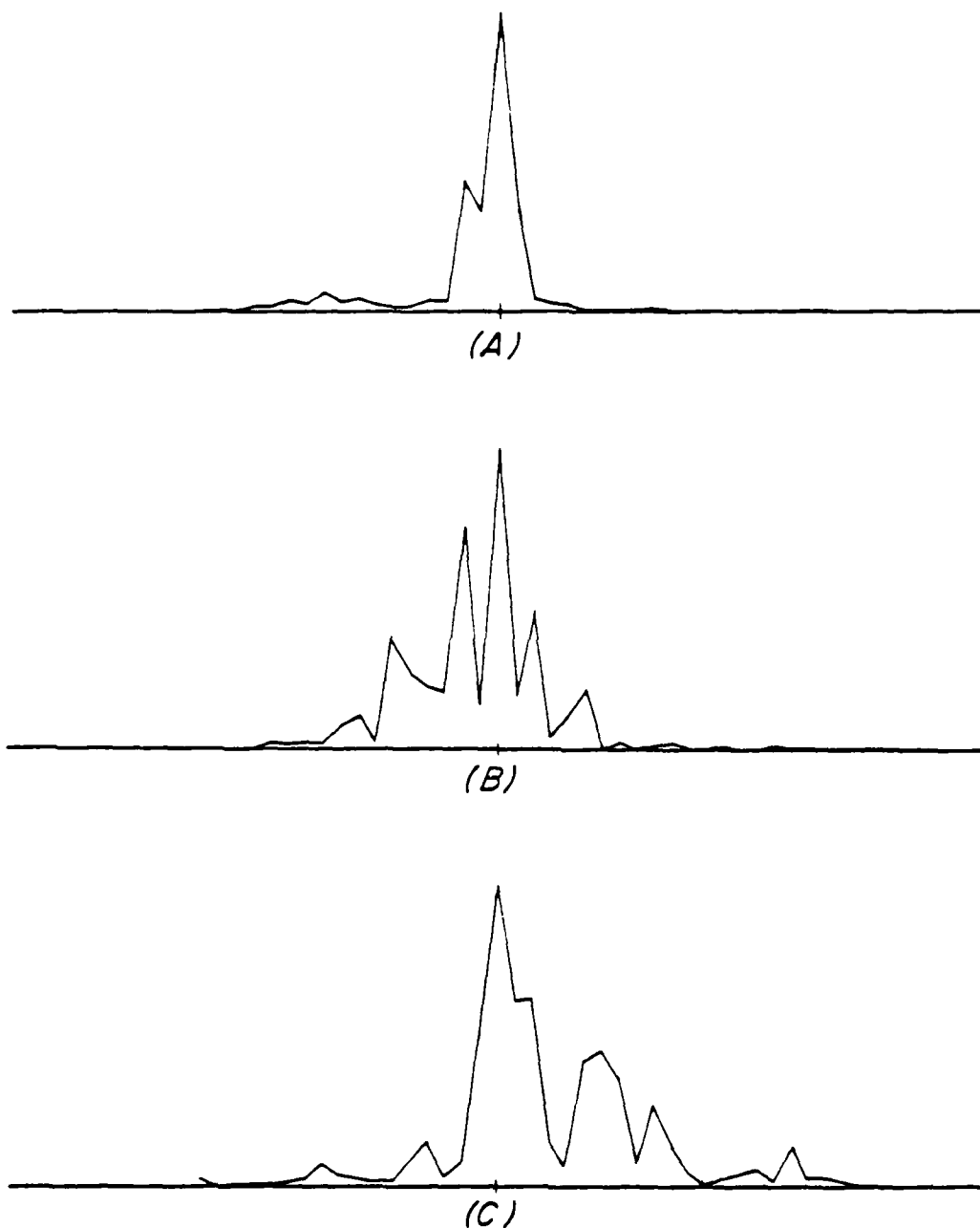
Figure 4.1. $s_m(x)$ for varying degrees of turbulence. — Taken from horizontal or vertical slices through the maximum of simulated images.

(A)

(B)

(C)
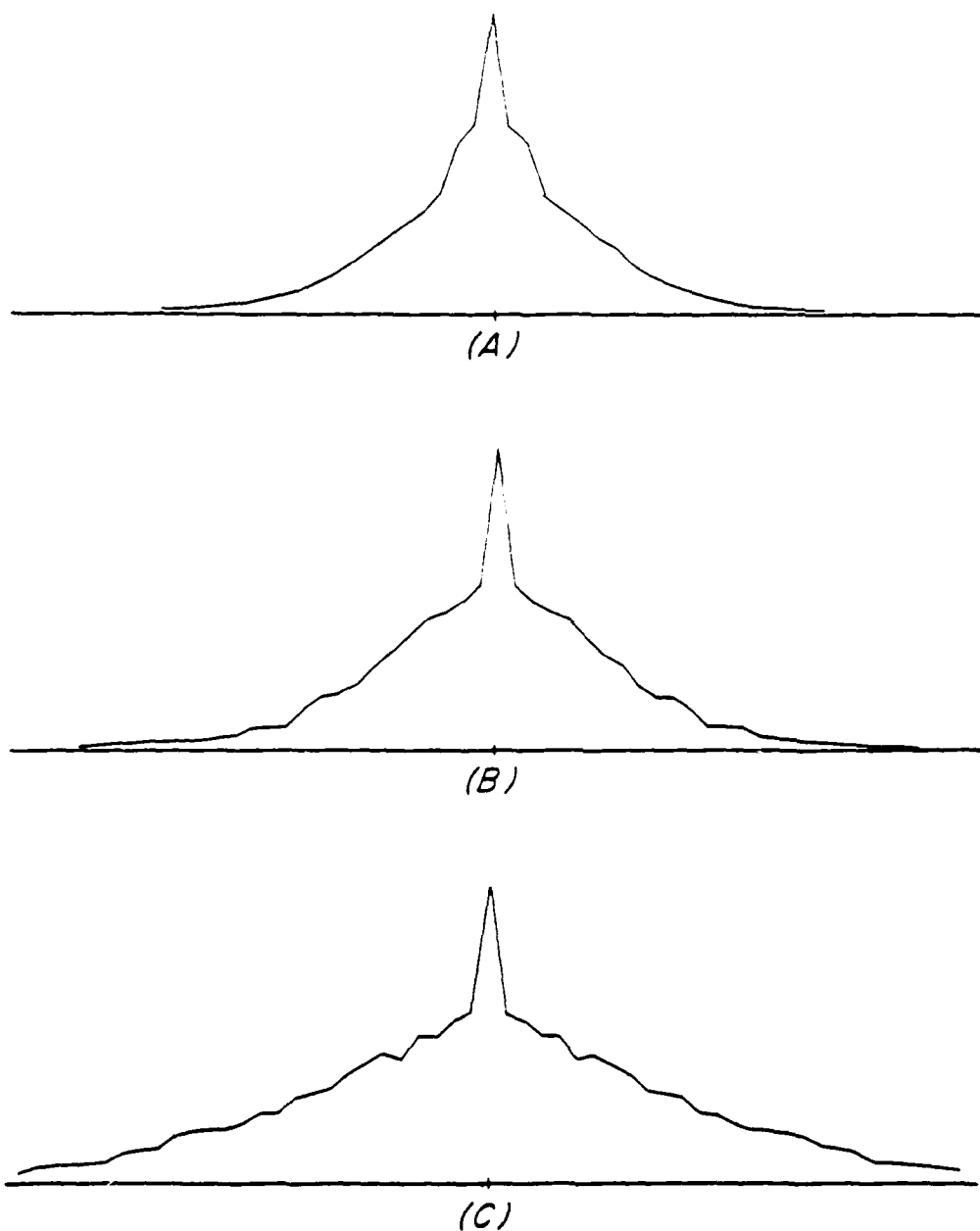
Figure 4.2. $P_s(x)$ for varying degrees of turbulence. -- Horizontal or vertical slices through the autocorrelation images corresponding to the $s_m(x)$ of Figure 4.1.

parameters for the atmosphere and optical system, so we shall consider our third possibility.

This third option for characterizing $R_s(x)$ is an approximation to Korff's result developed by Dainty (1975). Dainty has claimed that Korff's result is in "broad agreement" with that obtained by the simpler model

$$\langle |T(f)|^2 \rangle = |\langle T(f) \rangle|^2 + kT_D(f)$$

where $|\langle T(f) \rangle|^2$ is the squared modulus of the long exposure transfer function, $T_D(f)$ is the diffraction-limited transfer function, and $k < 1$ is a constant depending on atmospheric and telescope parameters. As in Hunt, Fright and Bates (1983), we inverse Fourier transform this equation, obtaining

$$\langle R_s(x) \rangle = l(x) + kKa(x)$$

where $l(x)$ is the long exposure component of $R_s(x)$, i.e., the autocorrelation of the seeing disc; $a(x)$ is the diffraction-limited component of $R_s(x)$, i.e., the Airy disc of the telescope; and K is a normalizing factor required to force $\langle R_s(0) \rangle = \langle I^2 \rangle$.

Then from Equation (4.8),

$$\lim_{M\to\infty} s(x) = s_{max} \left[\frac{\log<I>^2}{\log<I^2> - \log<I>^2} \right]$$

$$x \ [l(x) + kKa(x)]^{\frac{1}{2} \left[\frac{2\log s_{max} + \log<I^2> - \log[l(x)+kKa(x)]}{\log<I^2> - \log<I>^2} \right]} .$$

$$(4.9)$$

The first term of this expression is a constant, so diffraction-limited behavior will occur in the second term depending on the relative magnitudes of $l(x)$ and $kKa(x)$; that is, if the diffraction-limited $kKa(x)$ is large enough compared to the broad smooth function $l(x)$.

This discussion, together with Equation (4.9), completes our characterization of the point spread function of the shift-and-add process.

4.2 Analysis for Two Point Sources

The next degree of complication in this procedure is obviously to consider an object consisting of two point sources. The behavior of the shift-and-add process is unchanged although now the possibility of ghost peaks exists, and it is the probability of such an occurrence that will be the major focus of this section.

We first define our object

$$f(x) = a_1\delta(x-x_1) + a_2\delta(x-x_2) \qquad (4.10)$$

where $a_1 > a_2$. Then clearly each speckle image takes the form

$$s_m(x) = a_1 h_m(x-x_1) + a_1 h_m(x-x_2). \qquad (4.11)$$

where we are again ignoring the contamination term. Shift-and-add

processing will allow objects to be resolved, each with a profile of

the form of Equation (4.8), if the distance $|x_2-x_1|$ between the two

point objects is greater than the correlation length of the

diffraction-limited component of the speckle image. At this point we

define some notation

$$w = a_2/a_1$$

$$\langle I_1 \rangle = \text{mean value of } a_1 h_m(x-x_1)$$

$$\langle I_2 \rangle = \text{mean value of } a_2 h_m(x-x_2)$$

$$= w \langle I_1 \rangle$$

$$\sigma_{I_1}^2 = \text{variance of } a_1 h_m(x-x_1)$$

$$\sigma_{I_2}^2 = \text{variance of } a_2 h_m(x-x_2)$$

$$= w^2 \sigma_{I_1}^2$$

where of course we are concentrating our attention on the central

portion of each speckle pattern $a_i h_m(x-x_i)$ where the speckle image may

be treated as a stationary random process with constant mean. With

this notation established, we may use Equation (4.8) to define a

composite shift-and-add profile

$$s(x) = s_{max} \left[\dfrac{\log<I_1>^2}{\log<I_1^2>-\log<I_1>^2} \right]$$

$$\times\, R_s(x - x_1)^{\frac{1}{2}\left[\dfrac{2\log s_{max} + \log<I_1^2> - \log R_s(x-x_1)}{\log<I_1^2> - \log<I_1>^2} \right]}$$

$$+ (w s_{max})^{-\left[\dfrac{\log<I_2>^2}{\log<I_2^2> - \log<I_2>^2} \right]}$$

$$\times\, [w R_s(x - x_2)]^{\frac{1}{2}\left[\dfrac{2\log w + 2\log s_{max} + \log<I_1^2> - \log R_s(x-x_2)}{\log<I_1^2> - \log<I_1>^2} \right]}$$

This result is no longer valid when the point objects are separated by less than the correlation length of the diffraction-limited component of the speckle images. In this case, the point spread functions from the two objects overlap and the simple lognormal statistics used to derive Equation (4.3) are no longer valid. For the remainder of our discussion, we will assume that the two point sources are separated by more than the correlation length of the diffraction-limited component of the speckle images.

4.2.1 Analysis of Ghost Peaks

Under this assumption, we will now carry out the analysis of ghost peaks for the two point source object of Equation (4.10). As noted in Equation (4.11), the individual speckle images are of the form

$$s_m(x) = a_1 h_m(x-x_1) + a_2 h_m(x-x_2), \ a_1 > a_2.$$

For the shift-and-add process to be carried out correctly, the maximum value of $s_m(x)$ should be the maximum of $a_1 h_m(x-x_1)$. There are two ways that this may be prevented from occurring. First, the sum of any two speckles from $a_1 h_m(x-x_1)$ and $a_2 h_m(x-x_2)$ may exceed the sum of the maximum of $a_1 h_m(x-x_1)$ and any speckle from $a_2 h_m(x-x_2)$. Intuitively, one would not expect this to occur in any systematic fashion, since this would be completely unrelated to the maximum of $a_2 h_m(x-x_2)$. Thus if this error occurred repeatedly, it would result in a general randomness in $s(x)$ rather than in a false peak. The second way that an incorrect maximum may be chosen will result in a ghost peak if it occurs repeatedly. This happens when the maximum of $a_2 h_m(x-x_2)$ plus any speckle from $a_1 h_m(x-x_1)$ exceeds the sum of the maximum of $a_1 h_m(x-x_1)$ and any speckle from $a_2 h_m(x-x_2)$. The probability with which this occurs will determine the relative magnitude between correct and false peaks.

Therefore we will calculate this probability using the notation of Hunt, Fright and Bates (1983). We let

$z = $ maximum of $a_1 h_m(x-x_1)$

$$w = \frac{<I_2>}{<I_1>} = \frac{a_2}{a_1}$$

$wz = $ maximum of $a_2 h_m(x-x_2)$

$r.v.(1) = $ a random variable with probability density

$$p(I_1) = \frac{1}{I_1 \sigma_1 \sqrt{2\pi}} \exp \left\{ \frac{-[\log I_1 - \mu_1]^2}{2\sigma_1^2} \right\}$$

$$= \text{a speckle from } a_1 h_m(x-x_1),$$

and r.v.(2), likewise.

We then define

$$u = z + \text{r.v.}(2)$$

$$v = wz + \text{r.v.}(1)$$

The probability that the correct maximum of $s_m(x)$ will be chosen is $P[u>v]$ and the probability that the maximum of $a_2 h_m(x-x_2)$ will be chosen instead is $P[v>u] = 1 - P[u>v]$. (We are ignoring here the possibility of two speckles adding together to exceed either u or v.)

Now, for each speckle image, both the magnitudes and positions of z and wz are fixed. Also, given our assumption that the two point-source objects are separated by more than the correlation length of the diffraction-limited component of the speckle images, we may consider r.v.(1) and r.v.(2) to be independent but conditioned on z. Thus

$$p(u,v|z) = p(u|z)p(v|z)$$

which from simple probability is

$$p(u,v|z) = \frac{1}{2\pi\sigma_1\sigma_2} \frac{1}{(u-z)(v-wz)} \exp \left\{ \frac{-[\log(u-z)-\mu_2]^2}{2\sigma_2^2} - \frac{]\log(v-wz)-\mu_1]^2}{2\sigma_1^2} \right\}$$

We will now simplify this expression by recalling

$$\langle I_1 \rangle = \text{mean value of } a_1 h_m(x-x_1)$$

$$\langle I_2 \rangle = \text{mean value of } a_2 h_m(x-x_2) = w \langle I_1 \rangle$$

$$\sigma_{I_1}^2 = \text{variance of } a_1 h_m(x-x_1)$$

$$\sigma_{I_2}^2 = \text{variance of } a^2 h_m(x-x_2) = w^2 \langle I_2 \rangle$$

and for lognormal random variables

$$\langle I_1 \rangle = e^{\mu_1 + \sigma_1^2/2}$$

$$\sigma_{I_1}^2 = \langle I_1 \rangle^2 [e^{\sigma_1^2} - 1], \text{ likewise for } \langle I_2 \rangle, \sigma_{I_2}^2.$$

This leads to

$$c_2^2 = c_1^2$$

$$\mu_2 = \mu_1 + \log w,$$

so we set

$$\sigma_1 = \sigma_2 = \sigma^2$$

$$\mu_1 = \mu$$

$$\mu_2 = \mu + \log w$$

and

$$p(u,v \mid z) = \frac{1}{2\pi\sigma^2} \frac{1}{(u-z)(v-wz)} \exp\left\{ \frac{-[\log(\frac{u-z}{2})-u]^2 - [\log(v-w-z)-u]}{2\sigma^2} \right\}.$$

Then the probability integral of interest is

$$P[v>u] = \frac{1}{2\pi\sigma^2} \int_{wz}^{\infty} \int_{z}^{v} \frac{1}{v-wz} \exp\left\{ \frac{-[\log(v-wz)-u]^2}{2\sigma^2} \right\} \frac{1}{u-z} \exp\left\{ \frac{-[\log(\frac{u-z}{w})-u]^2}{2\sigma^2} \right\} du\,dv.$$

We first consider the case of $w = 1$, for which the integral is analytically evaluable. Then

$$P\,[v>u] = \frac{1}{2\pi\sigma^2} \int\limits_{z}^{\infty}\int\limits_{z}^{v} \frac{1}{v-z}\exp\left\{\frac{-[\log(v-z)-\mu]^2}{2\sigma^2}\right\}\frac{1}{u-z}\exp\left\{\frac{-[\log(u-z)-\mu]^2}{2\sigma^2}\right\}du\,dv$$

and we make the change of variable

$$s = \log(v-z)$$

$$t = \log(u-z)$$

to obtain

$$P\,[v>u] = \frac{1}{2\pi\sigma^2}\int\limits_{-\infty}^{\infty}\int\limits_{-\infty}^{s} e^{-\frac{[s-\mu]^2}{2\sigma^2}}\,e^{-\frac{[t-\mu]^2}{2\sigma^2}}\,dt\,ds$$

and using the evaluation of the normal probability integral from

Abramowitz and Stegun (1970)

$$P\,[v>u] = \frac{1}{2\sigma\sqrt{2\pi}}\int\limits_{-\infty}^{\infty} e^{-\frac{[s-\mu]^2}{2\sigma^2}}[1 + \mathrm{erf}(\frac{s-\mu}{\sigma\sqrt{2}})]\,ds$$

We now let

$$p = \frac{s-\mu}{\sigma\sqrt{2}}$$

and the integral becomes

$$P\,[v>u] = \frac{1}{2\sqrt{\pi}}\int\limits_{-\infty}^{\infty} dp\,e^{-p^2} + \frac{1}{2\sqrt{\pi}}\int\limits_{-\infty}^{\infty} dp\,e^{-p^2}\mathrm{erf}\,p.$$

The second integral is equal to zero because its integrand is odd, so

our result is $P\,[v>u] = 1/2$, which agrees entirely with our intuition.

The obvious question to address at this point is how fast this

probability decreases as w decreases from 1. Unfortunately, for values

of w other than 1, the integral is analytically intractable so we
resort to numerical integration. Numerical integration requires
calculation of this probability in the form $P[v>u] = 1 - P[u>u]$ to
avoid logarithms of negative numbers. Thus we are to calculate

$$P[u>v] = \frac{1}{2\pi\sigma^2} \int_{z}^{\infty} \int_{wz}^{u} \frac{1}{v-wz} \exp \frac{-[\log(v-wz)-\mu]^2}{2\sigma^2} \frac{1}{u-z} \exp -\frac{[\log(\frac{u-z}{w})-\mu]^2}{2\sigma^2} dv\, du$$

and making the usual change of variable

$$s = \log(v-wz)$$

$$t = \log(\frac{u-z}{w}),$$

the integral becomes

$$P[u>v] = \frac{1}{2\pi\sigma^2} \int_{-\infty}^{\infty} \int_{-\infty}^{\log(we^t+(1-w)z)} \exp\left\{\frac{-[s-\mu]^2}{2\sigma^2}\right\} \exp\left\{\frac{-[t-\mu]^2}{2\sigma^2}\right\} ds\, dt.$$

Evaluation of the s integral yields

$$P[u>v] = \frac{1}{2\sigma\sqrt{2\pi}} \int_{-\infty}^{\infty} \exp\left\{\frac{-[t-\mu]^2}{2\sigma^2}\right\} \left[1 + \operatorname{erf}\left(\frac{\log[we^t+(1-w)z]-\mu}{\sigma\sqrt{2}}\right)\right] dt$$

$$= \frac{1}{2\sigma\sqrt{2\pi}} \int_{-\infty}^{\infty} e^{-\frac{[t-u]^2}{2\sigma^2}} dt + \frac{1}{2\sigma\sqrt{2\pi}} \int_{-\infty}^{\infty} \exp\left\{\frac{-[t-u]^2}{2\sigma^2}\right\} \operatorname{erf}\left\{\frac{\log[we^t+(1-w)z]}{\sigma\sqrt{2}}\right\} dt$$

We let $p = \frac{t-u}{\sigma\sqrt{2}}$ and obtain

INTENTIONAL LEFT OUT

To avoid evaluation of a double integral, we have used the following expression from Abramowitz and Stegun (1970) as an approximation for erf x:

$$\text{erf } x = 1 - (a_1 t + a_2 t^2 + a_3 t^3 + a_4 t^4 + a_5 t^5)e^{-x^2} + e(x)$$

where

$$t = \frac{1}{1+px}$$

$$|e(x)| \leq 1.5 \times 10^{-7}$$

$$p = .3275911$$

$$a_1 = .254829592$$

$$a_2 = -.284496736$$

$$a_3 = 1.421413741$$

$$a_4 = -1.453152027$$

$$a_5 = 1.061405429$$

The integrand of Equation (4.12) is plotted in Figure 4.3, and the integration results for three sets of parameters are summarized in Tables 4.1 through 4.3.

The probabilities of selecting the wrong maximum seem unrealistically low, although they may indeed be realistic given the relatively large separation between the original point sources that we assumed in the modelling. However, we do in part attribute the low probabilities to the absence of noise and nonlinearities in the derivation and possibly to our assumption of constant means and variances $\langle I_1 \rangle$, $\langle I_2 \rangle$, σ_{I_1}, σ_{I_2}. This essentially is an assumption of

INTENTIONAL LEFT OUT

Table 4.1. Probability of selecting wrong maximum: average parameter values. -- $\langle I_1 \rangle = 12.6$; $\sigma_{I_1} = 27.1$; and $z = 243.55$. $\langle I_1 \rangle$ and σ_{I_1} for this table are the average values of the parameters (100 sets) supplied by Jon Freeman.

		$P\ (v > u)$	
w	Second Max wz	Simpson's Rule	7-Point Gaussian Quadrature
1	243.55	.500	.500
.99	241.11	.356	.356
.95	231.37	.052	.052
.9	219.19	.0035	.0035
.85	207.02	.0003	.0003
.8	194.84	.00003	.00004
.75	182.66	.000004	.00001
.5	121.78	.000001	.00001

Table 4.2. Probability of selecting the wrong maximum:
parameter values from a saturated frame. --
$\langle I_1 \rangle = 15.72$; $\sigma_{I_1} = 37.55$; and $z = 255$.

w	Second Max wz	$P\ (v > u)$ Simpson's Rule	7-Point Gaussian Quadrature
1	255.00	.500	.500
.99	252.45	.375	.375
.95	242.25	.075	.072
.9	299.59	.0063	.0063
.85	216.75	.0006	.00059
.8	204.00	.000064	.000072
.75	191.25	.0000089	.000017
.5	127.50	.000001	.0000099

Table 4.3. Probability of selecting the wrong maximum: parameter values from an unsaturated frame. -- $\langle I_1 \rangle = 9.55$; $\sigma_{I_1} = 16.44$; and $z = 218.00$.

		P (v > u)	
w	Second Max wz	Simpson's Rule	7-Point Gaussian Quadrature
1	218.00	.500	.500
.99	215.82	.334	.334
.95	207.17	.0342	.0342
.9	196.20	.00166	.00166
.85	185.30	.0001	.0001
.8	174.40	.00001	.00002
.75	163.50	.000002	.00001
.5	109.00	.000001	.00001

stationarity which is in actuality valid only in a small region about the maxima z and wz.

In spite of these unrealistically low probabilities, we may still draw the important conclusion that the correct maximum will be chosen in the majority of frames and the shift-and-add process carried out correctly even when the original point sources do not differ greatly in magnitude.

4.3 Analysis of the Extended Object Case

We now address the case of most practical interest, the case of an extended object rather than a set of isolated point sources. We then rewrite Equation (4.1) for this case

$$s_m(x) = \int_{-\infty}^{\infty} f(x-x_1) h_m(x_1) dx_1 + c_m(x) \qquad (4.13)$$

as a convolution integral, again following the notation of Hunt, Fright and Bates (1983). Ignoring the contamination term, $s_m(x)$ is, for fixed x, an integral of lognormal random variables $h_m(x_1)$ weighted by the object itself, $f(x-x_1)$. Digitally, of course, this becomes a weighted sum of lognormal random variables, or just a sum of nonidentically distributed lognormal random variables.

Thus the relevant question is: what are the statistics of sums of lognormal random variables? For the case of N independent random variables, the sum tends to become Gaussian distributed as N approaches infinity by the Central Limit Theorem. Barakat (1976) has investigated this case, with the added assumption that the random variables are identically distributed. His approach, as summarized below, is a

specific case of a result obtained earlier by Cramér (1951). We consider the sum

$$X = \sum_{k=1}^{N} X_k$$

where X_k are i.i.d. (independent identically distributed) random variables, each with the probability density function

$$p(x_k) = \begin{cases} \dfrac{1}{x_k \sigma \sqrt{2\pi}} \exp\left\{\dfrac{-[\log x_k - \mu]^2}{2\sigma^2}\right\} , & x > 0 \\ \\ 0, & \text{otherwise.} \end{cases}$$

Because the X_k are independent, we have

$$E[X] = NE[X_k]$$

$$\text{var}[X] = N\text{var}[X_k]$$

and for convenience we rescale as follows

$$Z_k = \frac{(X_k - E[X_k])}{\sqrt{\text{var}X}}$$

$$Z = \frac{(X - E[X])}{\sqrt{\text{var}X}}$$

so that

$$E[Z] = 0 \text{ and var}Z = 1.$$

Also due to independence, the characteristic function of Z is

$$E[e^{itz}] \equiv \phi_z(t) = [\phi_{z_k}(t)]^N$$

where

$$\phi_{z_k}(t) = \int_{-\infty}^{\infty} e^{iz_k t} \, p(z_k) dz_k$$

$$= \sum_{n=0}^{\infty} \frac{(it)^n <(X_k - E[X_k])>}{(varX)^n n!} \ .$$

Thus, with μ_i representing the ith central moment of Z,

$$\phi_z(t) = (1 - \frac{t^2}{2N} - \frac{it^3 \mu_3}{6\sigma^3 N^{3/2}} + \frac{t^4 \mu_4}{24\sigma^4 N^2} + O(N^{-5/2}))^N,$$

so taking the logarithm off both sides and using the expansion

$$\log(1+s) = \sum_{k=1}^{\infty} (-1)^{k+1} \frac{s^k}{k}, \qquad -1 < s \leq 1$$

$$\approx s - 1/2 \ s^2 + 1/3 \ s^3,$$

we obtain

$$\log \phi_z(t) \approx -\frac{t^2}{2} - \frac{i\mu_3 t^3}{6\sigma^2 N^{1/2}} + \frac{\mu_4 - 3\sigma^4}{24\sigma^4 N} t^4 + O(N^{-3/2})$$

and

$$\phi_z(t) \approx e^{-t^2/2}(1 - \frac{i\gamma_1 t^3}{6N^{1/2}} + O(N^{-1}))$$

where

$$\gamma_1 = \frac{\mu_3}{\mu_2^{3/2}} \text{ is the coefficient of skewness.}$$

Fourier transforming yields

$$p_N(z) \approx \frac{1}{\sqrt{2\pi}} e^{-z^2/2}(1 + \frac{\gamma_1}{6N^{1/2}} h_3(z) + O(N^{-1})) \qquad (4.14)$$

where $h_3(z)$ denotes the Hermite polynomial z^3-3z. Thus for large finite N, sums of independent lognormal random variables converge to a Gaussian probability density function only as $N^{-1/2}$. This result should also hold qualitatively for non-identically distributed random variables as long as the Central Limit Theorem conditions are met (see Section 2.1.1).

Our problem is complicated further by the fact that our lognormal random variables, $h_m(x)$, are weakly correlated as was illustrated in Figure (4.2). We see from this figure that the diffraction-limited portion of the autocorrelation is quite narrow; indeed the width of the base of the narrow peak is only twice the extent of a speckle. Since Barakat's result is based on use of the Central Limit Theorem, we assume that it would also apply (perhaps with even slower convergence) for random variables which are only weakly correlated. This is due to the fact that variations of the Central Limit Theorem do exist for dependent random variables (Loève, 1950; Serfling, 1968; Hoeffding and Robbins, 1948). According to Serfling (1968), the assumptions required for these Central Limit Theorems are in practice, not amenable to proof. It is further stated that many experimenters feel that the Gaussian approximation is valid for stationary processes which are observed for time (in our case spatial) intervals, which are long in comparison to the correlation length of the process.

We have assumed that our images are stationary, at least locally, and have noted that the diffraction-limited correlation length

Implicit in this calculation is the assumption of stationarity of the speckle point spread function and the integrated speckle images, which we continue to emphasize is valid only near the origin.

Inverse Fourier transforming Equation (4.16) yields the autocorrelation function $R_e(x)$ in terms of the previously discussed (section 4.2) $R_s(x) = R_h(x)$ and the autocorrelation of the object

$$R_e(x) = R_f(x)*R_h(x). \qquad (4.17)$$

As we noted, $R_h(x)$ may be decomposed into a low frequency and a diffraction-limited component

$$R_h(x) \approx 1(x) + kKa(x)$$

and we now suppose that the object power spectrum may also be decomposed into low frequency and diffraction-limited components

$$|F(u)|^2 = |F_l(u)|^2 + |F_d(u)|^2$$

or in the spatial domain

$$R_f(x) = R_l(x) + R_d(x).$$

Substituting in Equation (4.17) gives us

$$R_e(x) \approx 1(x)*[R_l(x)+R_d(x)] + kKa(x)*R_l(x) + kKa(x)*R_d(x).$$

$$(4.18)$$

Thus if the object contains a spatial frequency component out to the diffraction limit, the profile of $s(x)$ in Equation (4.15) may also

contain a diffraction-limited component provided that the magnitude of $k\bar{K}a(x)*R_d(x)$ is large enough relative to the remainder of Equation (4.18). Addition of the correlation component due to the contamination term $c_m(x)$ may further obscure the diffraction-limited information.

Now we return to the case of a large object $f(x)$ and assume a Gaussian distribution for the speckles of $s_m(x)$. The analysis for this case has been presented by Hunt, Fright and Bates (1983). As in section 4.1, the conditional expectation $E[I_2|I_1]$ is calculated; however, the conditional density function now takes the form

$$p(I_2|I_1) = \frac{1}{\sigma_e\sqrt{2\pi(1-r)^2}} \exp\left\{\frac{-1}{2\sigma_e^2(1-r^2)} [(I_2-\langle I_e\rangle)-r(I_1-\langle I_e\rangle)]^2\right\}$$

$$(4.19)$$

where $\langle I_e\rangle$ and σ_e^2 are respectively the mean and variance of the integrated speckle pattern and

$$r = r(x) = \frac{R_e(x)}{\sigma_e^2}$$

is the normalized correlation of the integrated speckle pattern. We further note that $r(x)$ is a zero mean correlation coefficient with $r(x) \leq 1$, and that the usual stationarity properties are assumed. Evaluation of $E[I_2|I_1]$ gives

$$\lim_{M\to\infty} s_e(x) = \langle I_e\rangle + \frac{R_e(x)}{\sigma_e^2} [s_{max} - \langle I_e\rangle] \qquad (4.20)$$

where $R_e(x)$ is characterized as in Equation (4.18) but with the quantity $\langle I_e\rangle^2$ subtracted because the correlation is required to be zero mean. Thus

$$R_e(x) = 1(x)*[R_1(x)+R_d(x)]+k\bar{K}a(x)*R_1(x)+k\bar{K}a(x)*R_d(x)-<I_e>^2. \quad (4.21)$$

and if desired, one may also include the autocorrelation of the

contamination term $R_c(x)$. As before, we will obtain diffraction-

limited resolution if the magnitude of $k\bar{K}a(x)*R_d(x)$ is large enough

relative to the other components of Equation (4.21). In both Equations

(4.18) and (4.21), $1(x)*[R_1(x)+R_d(x)]$ and $k\bar{K}a(x)*R_1(x)$ are smooth

functions and the useful information $k\bar{K}a(x)*R_d(x)$ will thus be found

riding on a broad background.

So, as noted by Hunt, Fright and Bates (1983), if $R_e(x)$

possesses a large enough diffraction-limited component and $f(x)$

contains a strong point source, the linearity of the shift-and-add

process will reconstruct the extended object (on a background). Also,

a very strong point source should ensure that the maximum value is

correctly chosen for each $s_m(x)$. Such sources may be expected to occur

often in natural imagery, e.g., an unresolvable star near an

astronomical object of interest or a glint on the wing of an airplane.

In Chapter 6, we present supporting simulation results for

shift-and-add processing of a simulated astronomical object with a

nearby "star" and demonstrate that further improvement may be obtained

by Wiener filtering of the shift-and-add result.

4.4 Miscellaneous Results

In the remainder of this chapter we will examine other results

on the shift-and-add algorithm. In section 4.4.1, we will analyze the

question of convergence which is of considerable interest. Following

this, we will discuss some of the work of Bagnuolo (1984) in which he examines the effect of nonisoplanaticity (i.e., lack of shift invariance over the entire image) on the shift-and-add method.

4.4.1 Convergence of the Shift-and-Add Algorithm

In sections 4.1 through 4.3 we have analyzed the shift-and-add method and found that it may produce an image containing diffraction-limited information. In all of this analysis, it was effectively assumed that an infinite number of images was summed which is, of course, not feasible in practice. Thus we are led to inquire just how fast the shift-and-add algorithm converges--does it require five or five thousand summations?

To answer this question, we recall that for each fixed x shift-and-add consists of summing M lognormally distributed random variables, where M is the number of frames processed. These random variables are independent, since they occur in different frames; and since we are considering a fixed spatial position, we will also assume that they are identically distributed. Hence, Barakat's (1976) results (as discussed extensively in section 4.3) apply directly. That is, the sum of random variables approaches its limiting distribution as $M^{-1/2}$. We stress, as does Barakat, that this conclusion is valid only for large M. We have observed in our simulations that convergence is more rapid for small M, say < 10. However, this would be true even if $M^{-1/2}$ convergence is valid.

We may see this same result another way, by considering a "noise-to-signal ratio" for the sum of independent identically

distributed lognormal random variables at fixed spatial position x.
That is, we are constructing a ratio of the spread about the mean to
the mean of the sum. For convergence, we wish this ratio to decrease
to zero. Following the notation of section 4.1 and ignoring
contamination effects, we have the sum

$$s(x) = \sum_{m=1}^{M} \sigma_m(x)$$

which has mean and variance

$$E[s(x)] = ME[\sigma_m(x)] = M\langle\sigma_m(x)\rangle$$

$$var[s(x)] = Mvar[\sigma_m(x)] = M\langle\sigma_m(x)\rangle^2[e^{\sigma^2}-1]$$

where $\sigma^2 = var[\log \sigma_m(x)]$. Then our noise-to-signal ratio for the sum
is

$$\frac{N}{S} = \frac{\sqrt{var(s(x))}}{E(s(x))} = \frac{\sqrt{M}\langle\sigma_m(x)\rangle\sqrt{e^{\sigma^2}-1}}{M\langle\sigma_m(x)\rangle} = \frac{\sqrt{e^{\sigma^2}-1}}{\sqrt{M}}.$$

The numerator of this quantity is constant, so the noise-to-signal
ratio decreases as $M^{-1/2}$, which agrees with our prior conclusion.

Thus we have determined that convergence of the shift-and-add
algorithm is slow; however, in our simulations (Chapter 6), notable
improvement has been achieved with sequences of only twenty frames. An
important conclusion suggested by this slow convergence is that it may
well be advantageous to average fewer frames and achieve further
deblurring by other techniques; for example, Wiener filtering, rather
than simply continuing to increase M.

4.4.2 Effect of Nonisoplanaticity on Shift-and-Add

For the entire preceding analysis, we have made the assumption of isoplanaticity. That is, we have assumed that the image was formed by passage of wavefronts from the entire object through one statistically homogeneous portion of the atmosphere, giving us a shift-invariant point spread function. According to Dainty (1975), it has been found experimentally that this assumption is invalid for star fields or larger objects.

In this case, Equation (4.13) becomes

$$s_m(x) = \int_{-\infty}^{\infty} f(x')h_m(x;x')dx' \qquad (4.22)$$

where we have ignored the contamination term $c_m(x)$. The intuitive approach is to decompose $h_m(x;x')$ into a spatial sum of shift invariant point spread functions

$$h_m(x) = \sum_{j=1}^{K} h_{mj}(x-x_j)$$

where K is the number of isoplanatic patches through which the object wavefronts pass. One would then make convergence arguments allowing the change of order of summation and integration in (4.22), yielding

$$s_m(x) = \sum_{j=1}^{K} s_{mj}(x-x_j).$$

Then shift-and-add gives

$$s(x) = \frac{1}{M} \sum_{m=1}^{M} s_m(x)$$

$$= \frac{1}{M} \sum_{m=1}^{M} \sum_{j=1}^{K} s_{mj}(x-x_j).$$

At this point the analysis becomes intractable because K is a random variable depending on the step m. Therefore, another approach should be taken in order to achieve any results.

Bagnuolo (1984) has addressed this problem for the specific case of the shift-and-algorithm applied to imaging of double stars. In an earlier paper (Bagnuolo, 1982), he has presented a slightly modified shift-and-add algorithm and a method for calculating the intensities of the background, the two valid peaks representing the double star, and the accompanying ghost peak. Ratios of these intensities are then used to compute the true intensity ratio for the two components of the double star. In his later publication (Bagnuolo, 1984), he has shown that his method is invariant to the degree of isoplanaticity. This is by no means a general theoretical result, but it may indicate that nonisoplanaticity is not a serious problem in shift-and-add processing.

CHAPTER 5

COMPUTER SIMULATION OF TURBULENCE DEGRADATIONS

In order to test the effectiveness of the shift-and-add
algorithm, especially for the case of extended object imaging, we next
performed simulations of the image degradations produced by atmospheric
turbulence. Series of point spread functions have been computed, both
for an algorith. developed by McGlamery (1976) that considers only
phase perturbations of the optical wave and for a modified version of
this algorithm, which also includes amplitude perturbations. These
point spread functions were then convolved with a simulated object, and
the resulting series of degraded object frames were subjected to
shift-and-add processing and other restoration techniques, as discussed
in Chapter 6. In this chapter, we will examine the two algorithms for
computing point spread functions that we mentioned above.

5.1 Point Spread Function Simulation
for Phase Perturbations Alone

The first algorithm that we used for point spread function
simulation was one developed by McGlamery (1976). In this algorithm,
he has considered only phase perturbations of the optical wavefront
since he claims that these are the dominant factor in image degrada-
tion. He also assumes, as is common (Strohbehn, 1968) that the
Kolmogorov spectrum

70

$$\phi(f) = Cf^{-11/3}$$

is a valid description of the spatial power spectrum of the phase at
the receiver, where C is a constant related to turbulence strength and
wavelength and f denotes spatial frequency. With these preliminary
assumptions noted, we now summarize the algorithm.

Step one consists of generating a complex array of Gaussian
random numbers that are to represent the spatial frequency domain for
the phase of the wavefront. (Phase is assumed to be Gaussian
distributed, as discussed in Chapter 2, which necessarily implies that
it is also Gaussian in the frequency domain.) In step two, we multiply
the array by $f^{-11/6}$, the square root of the Kolmogorov spectrum. This
factor introduces correlation into the point spread function, for
without it, one produces a random noise field rather than a speckle
pattern. The third step consists of Fourier transforming the array and
separating the result into its real and imaginary parts. Each of these
arrays represents a map of phase at the pupil of the optical system,
which we denote by $\phi(u,v)$. In step four, we form the path length
difference map

$$d(u,v) = \frac{\phi(u,v)\lambda}{2\pi}$$

where λ denotes wavelength, and we note that this step is unnecessary
if one is considering monochromatic illumination. The intensity point
spread function is calculated in step five as follows

$$h(x,y,\lambda) = |F\{p(u,v)\exp(i2\pi d(u,v)/\lambda)\}|^2$$

where $p(u,v)$ is the pupil function of the telescope, $|\cdot|^2$ denotes the squared magnitude of a complex quantity, and $F\{\cdot\}$ refers to the Fourier transform. The final step six is not computed in the monochromatic case. It involves forming the polychromatic point spread function

$$h(x,y) = k \sum_{\lambda} F(\lambda)h(x,y,\lambda)$$

where k is a normalizing factor required so that the value of the transfer function at zero frequency is unity, and $F(\lambda)$ is a weighting function which depends on spectral distributions of source power, atmospheric transmittance, and the image sensor. McGlamery (1976) also discusses other factors necessary for scaling in computations of the polychromatic point spread function.

In our simulations, we omitted steps four and six, and we varied the standard deviation of the Gaussian iterates in step one in order to vary the strength of the turbulence, rather than changing the constant C of the Kolmogorov spectrum. Furthermore, we ignored the effects of the telescope pupil and set $p(u,v)$ identically equal to unity. Examples of point spread functions simulated in this manner are shown in Figure 5.1. It should be observed that these point spread functions are of greater spatial extent than they appear in this figure. The outer edges do not appear because of a lack of dynamic range in the photographic process.
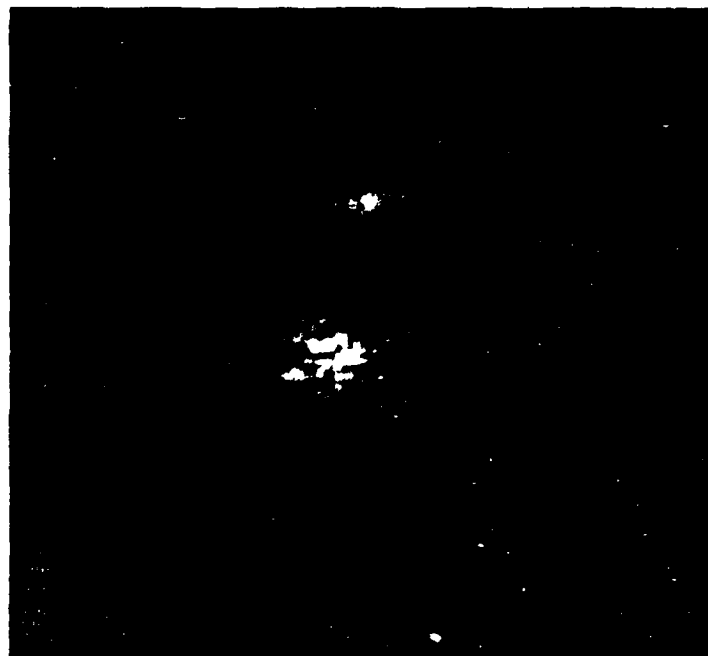
Figure 5.1a. Standard deviation σ from step one of the algorithm is 2.5.

Figure 5.1b. σ is 3.5.

5.2 Point Spread Function Simulation Including
Both Phase and Amplitude Effects

For the sake of completeness and also because amplitude perturbations are important in the assumption of lognormal intensity statistics (see Chapter 2), we modified McGlamery's algorithm (McGlamery, 1976) to include the effect of amplitude perturbations. According to Strohbehn (1968), the log-amplitude spatial power spectrum is also proportional to the Kolmogorov spectrum $f^{-11/3}$, and we know from Chapter 2 that log-amplitude is also governed by a Gaussian probability distribution. Therefore, simulation of amplitude effects proceeds in much the same manner as the simulation of phase effects in section 5.1.

Step one consists of generating a complex array of Gaussian ran numbers that represents the spatial frequency domain for log-amplitude. In step two, the array is multiplied by $f^{-11/6}$, the square root of the Kolmogorov spectrum, in order to introduce correlation. We then Fourier transform the array and separate the result into its real and imaginary parts for step three. Each of these arrays represents a map of log-amplitude, denoted logA, at the telescope pupil. Using the phase map $\Phi(u,v)$, which is generated by the method of section 5.1 and assuming monochromatic light, we complete the fourth and final step of the algorithm, the formation of the intensity point spread function

$$h(x,y) = \left| F\{p(u,v)\exp(\log A + i\phi(u,v))\} \right|^2$$

where as before, $F\{\cdot\}$ denotes Fourier transform, $|\cdot|^2$ indicates squared magnitude of a complex-valued quantity, and $p(u,v)$ is the pupil function of the telescope which was set identically equal to unity in all of our simulations.

Examples of the point spread functions simulated by this procedure are presented in Figure 5.2. The phase variations in this figure are statistically the same as those of Figure 5.1, so any difference is due to amplitude effects. As we see from Figure 5.2, the main effect that the amplitude perturbations have is a general blurring of the point spread function, and therefore, of any image convolved with it. This will be more clearly seen in Figure 6.3 of the next chapter.

5.3 Effect of Setting One Pixel
Equal to One Speckle

The simulation of point spread functions discussed in sections 5.2 and 5.3 results in speckle patterns in which each speckle is represented by a single pixel. In reality each speckle has a spatial extent on the order of the size of the Airy disc of the telescope (Dainty, 1975), so what one is actually simulating by the above algorithms is integrated or averaged speckle. As we have assumed throughout that the intensity at each point of the speckle pattern is distributed lognormally, we have a sum of partially correlated lognormal random variables. This is exactly the situation of section 4.4, where the weighting function is equal to one. As in this previous

Figure 5.2.   Point spread functions including both phase and amplitude
              degradations. -- Phase is statistically identical to that
              of Figures 5.1a and 5.1b.

a.   Phase corresponds to that of Figure 5.1a with severe amplitude
     degradation.

b.   Phase corresponds to that of Figure 5.1b with less severe ampli-
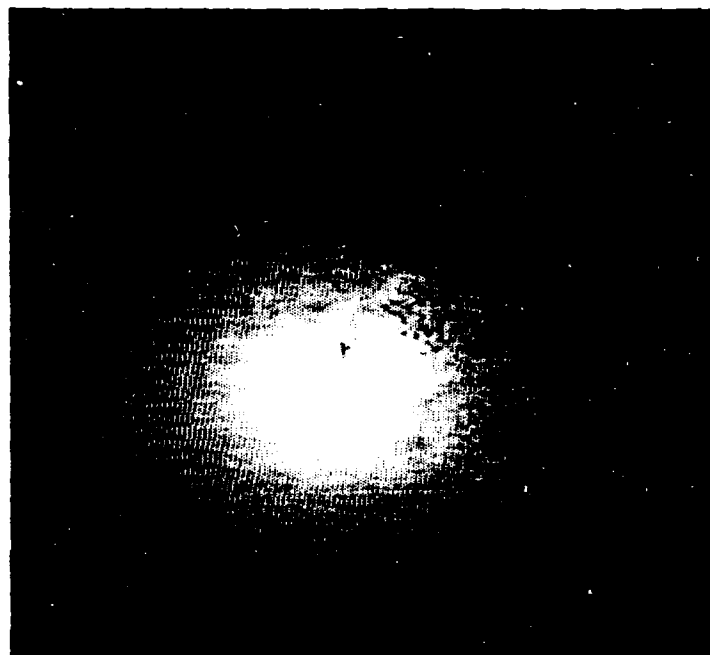   tude degradation.

Figure 5.2a. Phase corresponds to that of Figure 5.1a with severe
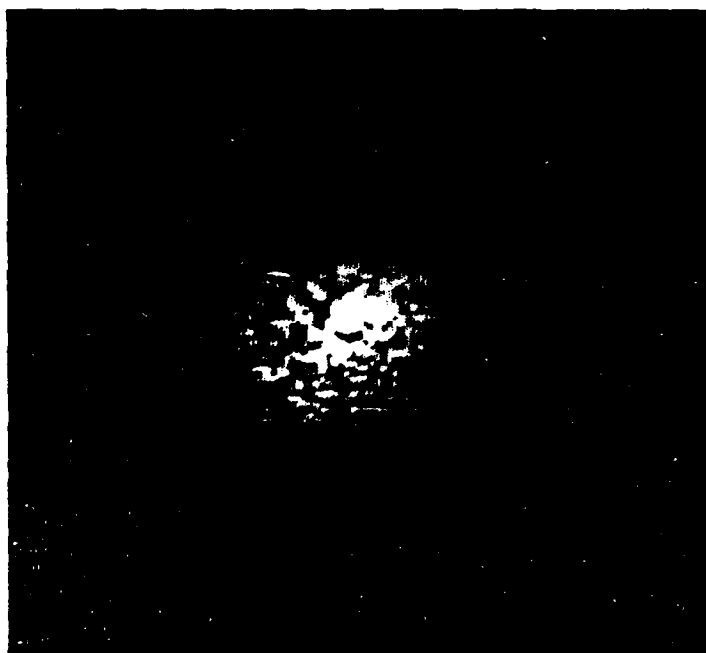amplitude degradation.

Figure 5.2b. Phase corresponds to that of Figure 5.1b with less severe
amplitude degradation.

analysis, we expect that this integrated or averaged speckle will be approximately Gaussian distributed when the number of random variables averaged is large (Barakat, 1976), but will be better described by a lognormal distribution when fewer random variables are averaged (Mitchell, 1968). As we are averaging over an area the size of the Airy disc in this case, we would expect relatively few pixels to be averaged, implying that a lognormal distribution is appropriate. In our simulations, telescope effects were ignored, which is equivalent to assuming an infinite pupil and thus a point source Airy disc. For this case, one pixel actually represents one speckle; but in more realistic cases, statistics of integrated speckle rather than simple speckle should be used in simulations.

CHAPTER 6

RESTORATION OF SIMULATED IMAGES

In this chapter we shall attempt to restore images degraded by
atmospheric turbulence using shift-and-add processing alone and then
combining shift-and-add processing and Wiener filtering (actually
pseudo-inverse filtering in the absence of noise) in order to confirm
our previously obtained theoretical results. Restoration will be
possible only if the derivations of Chapter 4 are correct, that is,
only if diffraction-limited information is indeed preserved by
shift-and-add. Otherwise, residual blur will be apparent in the final
results because of loss of high frequency information.

Using the methods described in Chapter 5, we have generated
series of twenty point spread functions (psf's) for varying degrees of
turbulence and have convolved these psf's with an undegraded image. We
emphasize that in these simulations, no other degradations (e.g.,
photon noise, sensor noise) have been introduced, although they are
certainly present in actual imagery.

In a previous study (Hunt, Morgan and West, 1983), we have
described the simulation and restoration of degraded images using a
simulated silhouette of an airplane as the original image. However,
Bates pointed out that the use of such a large object with a small psf
is a contradiction of reality. In order to simulate a more realistic

78

situation, we have used for our undegraded image a small circle at gray

level 110, with a dark (gray level 0) and a bright (gray level 192)

spot in the interior. The circle is of approximately the same spatial

extent as the smallest psf considered, and we added the interior spots

in order to test the ability of our processing to restore detail other

than the object outline. The undegraded image is intended to represent

a fairly large astronomical object, and therefore, we have also inclu-

ded a "star" (point source) at gray level 255 in the frame in order to

allow us to estimate the overall psf of atmospheric degradation plus

shift-and-add processing. This psf is used in further deblurring after

shift-and-add. Our undegraded image is pictured in Figure 6.1; a

series of degraded images with only phase perturbations (corresponding

to the psf's of Figure 5.1) is shown in Figure 6.2; and both phase and

amplitude variations (corresponding to the psf's of Figure 5.2) are

included in the degraded images of Figure 6.3.

6.1 Shift-and-Add Processing

With series of degraded images at our disposal, our next step

is restoration, which will first be attempted by shift-and-add

processing alone. Figure 6.4 depicts the results of shift-and-add of

twenty images (corresponding to Figure 6.2), which have been distorted

by phase variations alone, and the shift-and-add results for both phase

and amplitude degradations (corresponding to Figure 6.3) are shown in

Figure 6.5. We note that there is comparable improvement in the case

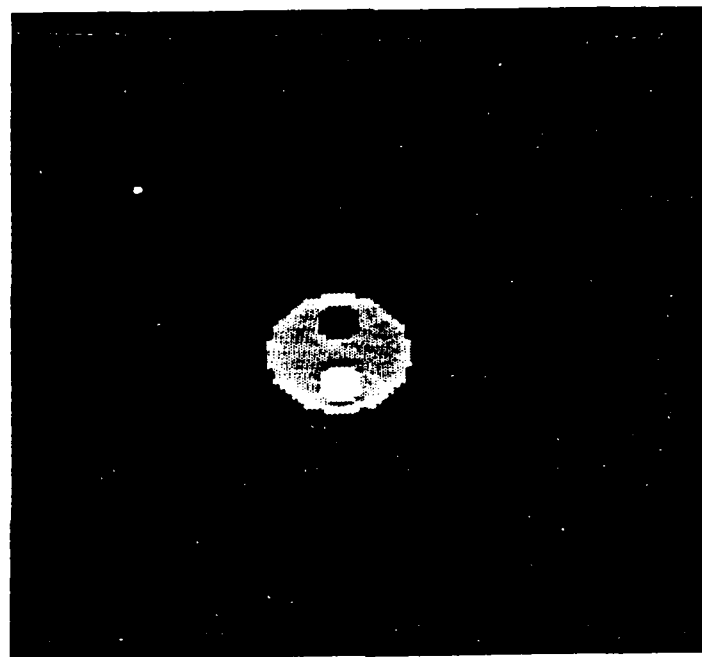of both phase and amplitude corruptions relative to the phase

Figure 6.1.   Original undegraded image.

Figure 6.2. Object blurred by convolution with psf's containing phase
degradations only.

a. Blur produced by psf of Figure 5.1a.

b. Blur produced by psf of Figure 5.1b.
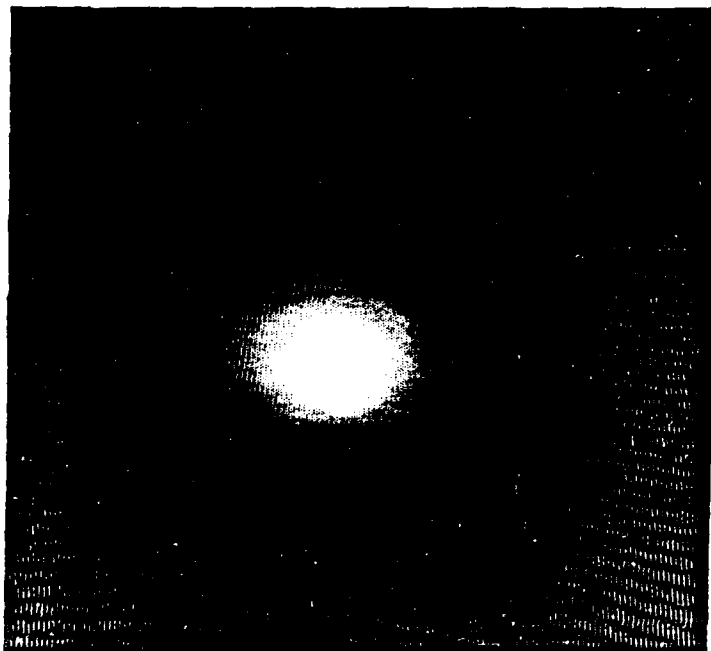
Figure 6.2a. Blur produced by psf of Figure 5.1a.

Figure 6.2b. Blur produced by psf of Figure 5.1b.

Figure 6.3. Object degraded by convolution with psf's containing both phase and amplitude degradations.

a. Blur produced by psf of Figure 5.2a.

b. Blur produced by psf of Figure 5.2b.

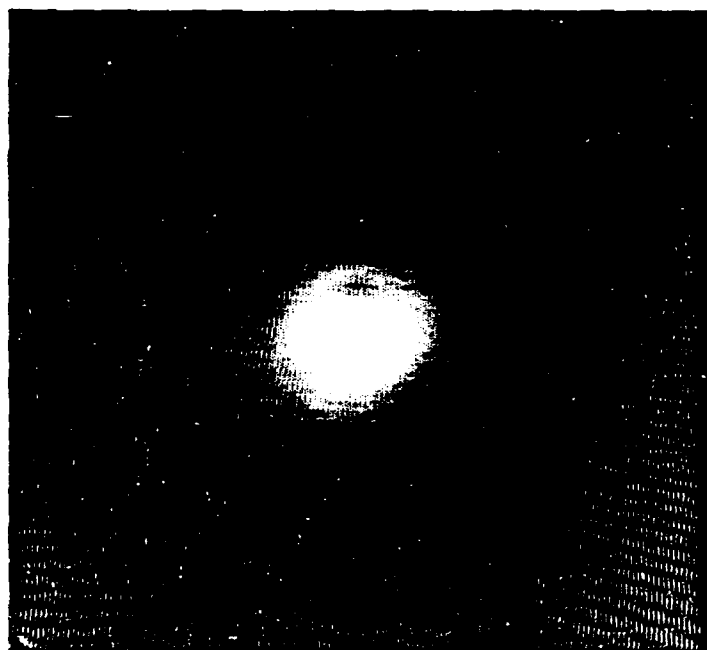Figure 6.3a. Blur produced by psf of Figure 5.2a.

Figure 6.3b. Blur produced by psf of Figure 5.2b.

Figure 6.4. Shift-and-add results for the averaging of 20 images degraded by phase perturbations alone.

a. Shift-and-add result for images degraded as in Figure 6.2a.

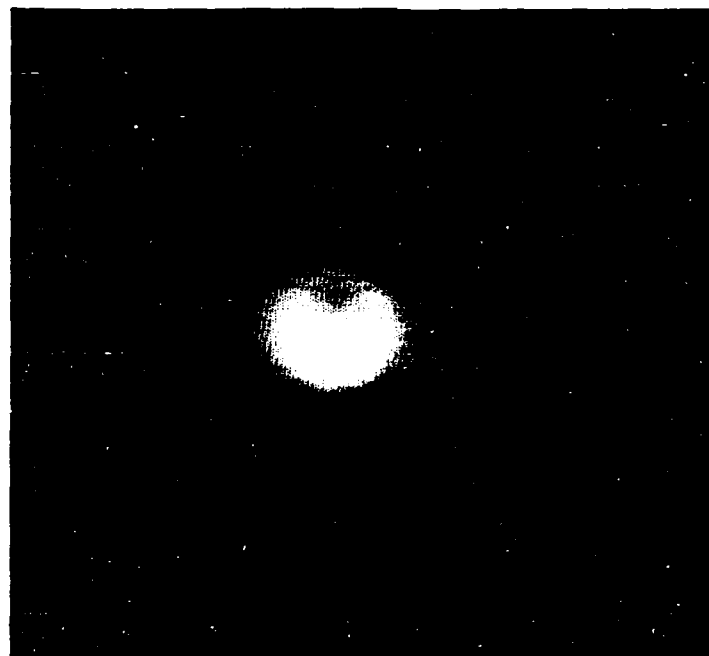b. Shift-and-add result for images degraded as in Figure 6.2b.

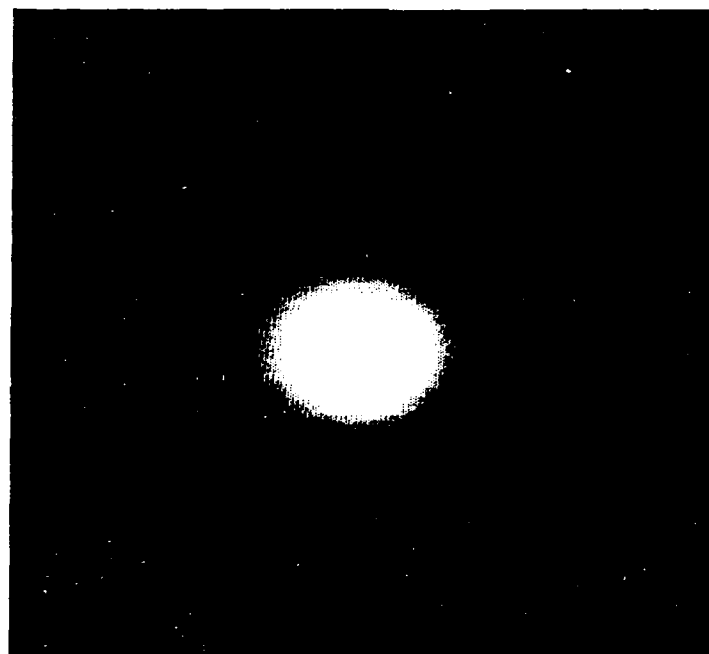Figure 6.4a. Shift-and-add result for images degraded as in Figure
6.2a.

Figure 6.4b. Shift-and-add result for images degraded as in Figure
6.2b.

Figure 6.5. Shift-and-add results for the averaging of 20 images degraded by both phase and amplitude perturbations.

a. Shift-and-add result for images degraded as in Figure 6.3a.

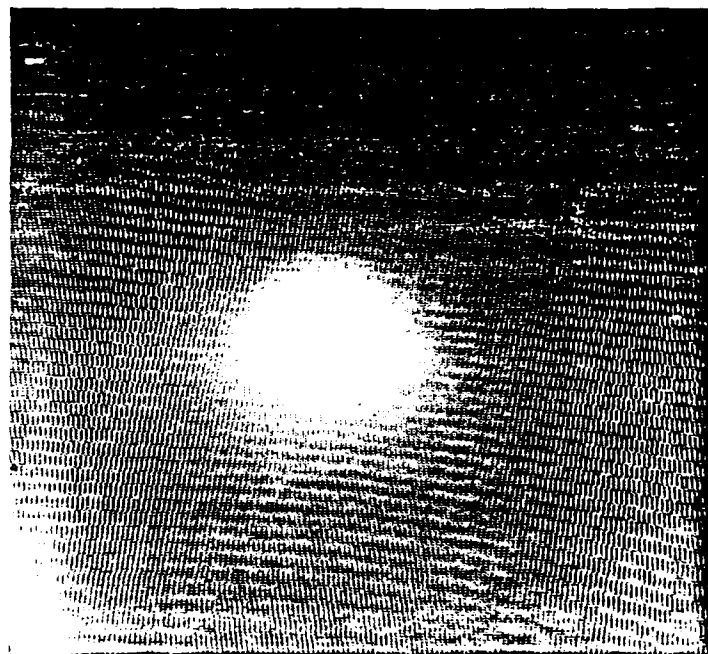b. Shift-and-add result for images degraded as in Figure 6.3b.

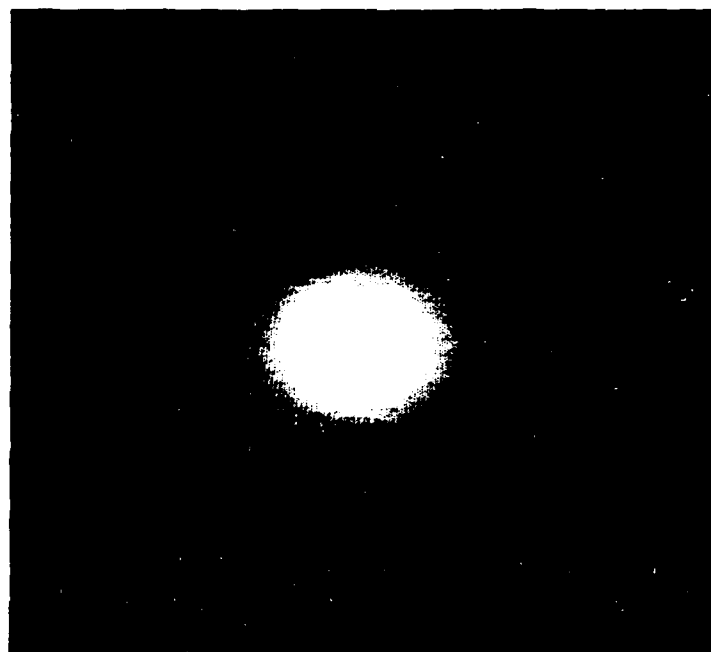Figure 6.5a. Shift-and-add result for images degraded as in Figure 6.3a.

Figure 6.5b. Shift-and-add result for images degraded as in Figure 6.3b.

degradation only case; and just as one would expect, the restoration is better for milder turbulence.

It is worthwhile at this point to note that although the gray level of the "star" or point source is higher than that of the bright interior spot in the object, the bright spot is larger in area, and the maximum value chosen from each frame by shift-and-add is a speckle generated by the bright spot. This observation implies that shift-and-add processing may well lead to a substantially improved estimate of the object as long as there is a relatively small bright area, not necessarily a point source, present in the object. Thus shift-and-add may be useful processing for a larger class of natural imagery than simply images of astronomical objects. One would expect the registration of the images to be less accurate in such cases, resulting in a more blurred shift-and-add image; however, as seen in the following sections, the overall point spread function of the blur may be estimated or measured and then removed by Wiener filtering.

We have further noted confirmation of our estimates of the convergence of this algorithm as discussed in section 4.4. In a prior report (Hunt, Morgan and West, 1983), we noted a comparison of shift-and-add results for twenty and fifty frames in which we observed no visible improvement in the fifty-frame result over the twenty-frame result. This accords well with our determination that the algorithm converges as $M^{-1/2}$ (where we recall that M is the number of frames averaged).

Finally, we note that while there is considerable improvement
in the shift-and-add results over a single short exposure frame or over
a simulated long exposure image (Figure 6.6), there is still a sizable
amount of blur present. The following sections are devoted to removal
of this residual blur.

6.2 Determination of the Overall Point Spread
Function for Atmospheric Degradations
Plus Shift-and-Add Processing

In order to apply further restoration techniques to the
shift-and-add image, we must measure or estimate the point spread
function (psf) for the entire process. If a point source such as our
simulated "star" is included in the original object, the psf may simply
be extracted from its shift-and-add image. This is the approach we
have used in our restorations; however, in cases of severe degradation,
subtraction of background blur from the psf is necessary.

We also used a Gaussian least-squares fit to the point spread
function in some restorations. This is because, in the limit of large
M, we expect the point spread function to approach a Dirac delta
function (or very narrow function) riding on a broad, smooth function
as in Equations (4.18) or (4.21) and the following discussion. Thus we
are assuming a Gaussian form for this smooth function. This may be a
useful approach for estimation of the psf when an auxiliary point
source is not present in the object if one can find a valid method of
determining the variance of the Gaussian.

If there is no point source present in the object, it may also
be possible to estimate the psf from the edge response of the object

Figure 6.6. Comparison of shift-and-add and simulated long exposure
images. -- Both were generated from a series of 20 images
degraded by phase perturbations alone.

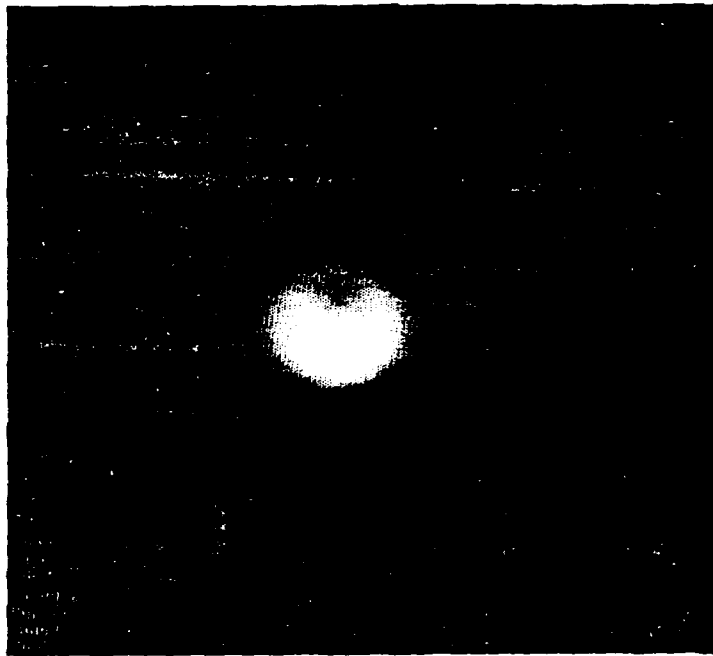a.   Shift-and-add.

b.   Long exposure.
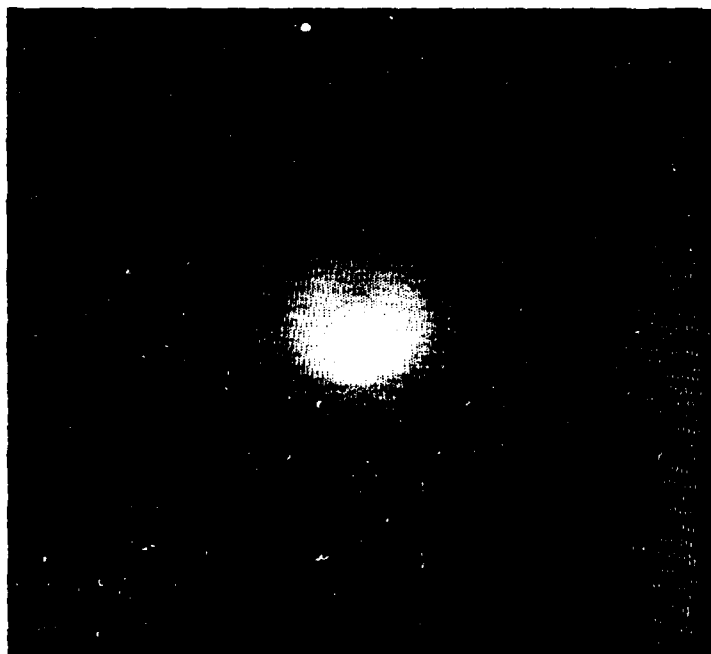
Figure 6.6a. Shift-and-add.

Figure 6.6b. Long exposure.

(Tatian, 1965; Tescher and Andrews, 1972). This type of procedure will
work best if the object is fairly large, containing large sharp edges,
a fact which will limit its usefulness in astronomy. However, in this
case a nearby star is often present, as was assumed in our simulations.

6.3 Wiener Filter Restoration

We now assume that we have obtained our desired point spread
function, whether measured or estimated, and proceed with the
deblurring. In our previous work (Hunt, Morgan and West, 1983), we
used both the Wiener and Cannon filters (Andrews and Hunt, 1977) but
subjectively determined that better results were achieved with the
Wiener filter. Therefore, we shall use the Wiener filter in our
present restorations and shall employ the following form of the filter

$$W(u,v) = \frac{H^*(u,v)}{|H(u,v)|^2 + \sigma n^2 / \Phi_f(u,v)}$$

where $H(u,v)$ is the Fourier transform of the psf, $*$ denotes complex
conjugation, $|.|$ indicates the modulus of a complex-valued function,
$\Phi_f(u.v)$ is the object power spectrum, and σ_n^2 is noise variance. We
have not actually measured or estimated a value for σ_n^2 but have simply
considered a constant which is varied to achieve the best restoration.
Also, we used the actual $\Phi_f(u,v)$ which we determined from the
undegraded image although in practice, this is not known and must be
estimated from the degraded image. Often, one would have some
information such as the expected object shape that will help in these
estimations.

Now, letting $S(u,v)$ represent the Fourier transform of the shift-and-add image, our estimate $\hat{f}(x,y)$ of the object is

$$\hat{f}(x,y) = F^{-1}\{S(u,v)W(u,v)\}$$

where as usual, $F^{-1}\{\cdot\}$ denotes the inverse Fourier transform. In order to achieve good results in cases of severe degradation, i.e., minimize "ringing," we were forced to smooth the sharp edges between the images and the zero backgrounds which were added as padding for the Fourier transforms. We found this to be necessary both in the shift-and-add image and the measured psf, and it was accomplished by multiplying the images by wide Gaussians.

These restorations have been performed for the shift-and-add images depicted in Figures 6.4 and 6.5, and the results are shown in Figures 6.7 and 6.8. From these figures we can see that the Wiener filter has done an excellent job of removing blur left in the shift-and-add images--the outlines of the object are sharp, and the interior spots have been well-reconstructed. It is important to note here that this ability to reconstruct the original object may be regarded as confirmation of the theoretical results of Chapter 4-- diffraction-limited information is indeed preserved by shift-and-add, at least in the absence of noise.

We have also performed Wiener filtering in a few cases with a Gaussian least-squares fit to the measured point spread function (as discussed in section 6.2), and one such outcome is shown in Figure 6.9. Some blur still remains in these images, and we attribute this to the

Figure 6.7.   Wiener filter restorations of the shift-and-add images
              depicted in Figure 6.4. -- Original image was degraded by
              phase perturbations alone.

a.   Wiener filter restoration of the image in Figure 6.4a.

b.   Wiener filter restoration of the image in Figure 6.4b.

Figure 6.7a. Wiener filter restoration of the image in Figure 6.4a.

Figure 6.7b. Wiener filter restoration of the image in Figure 6.4.b.

Figure 6.8. Wiener filter restorations of the shift-and-add images of Figure 6.5. -- Original image was degraded by both phase and amplitude perturbations.

a. Wiener filter restoration of the image in Figure 6.5a.

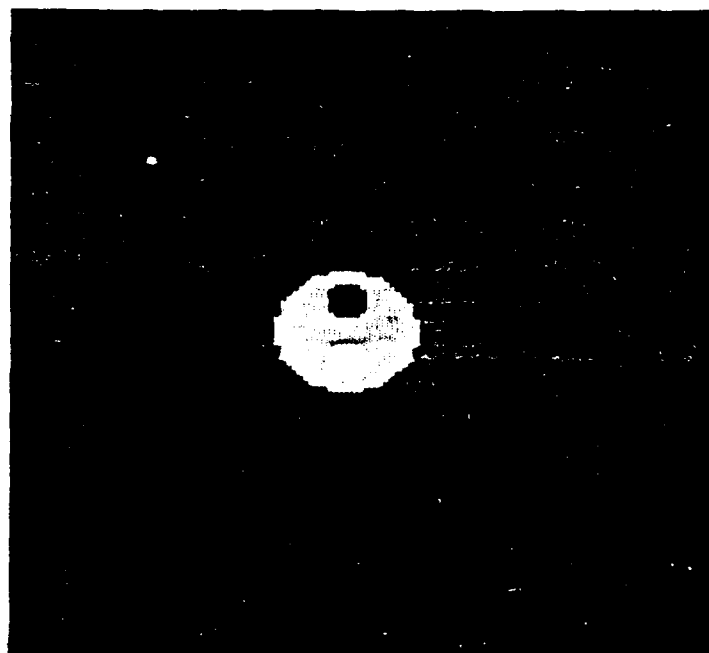b. Wiener filter restoration of the image in Figure 6.5b.

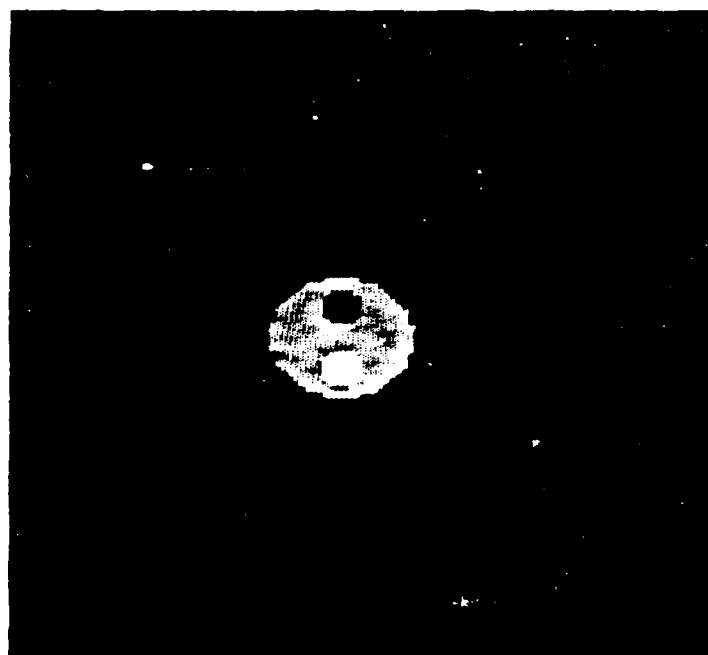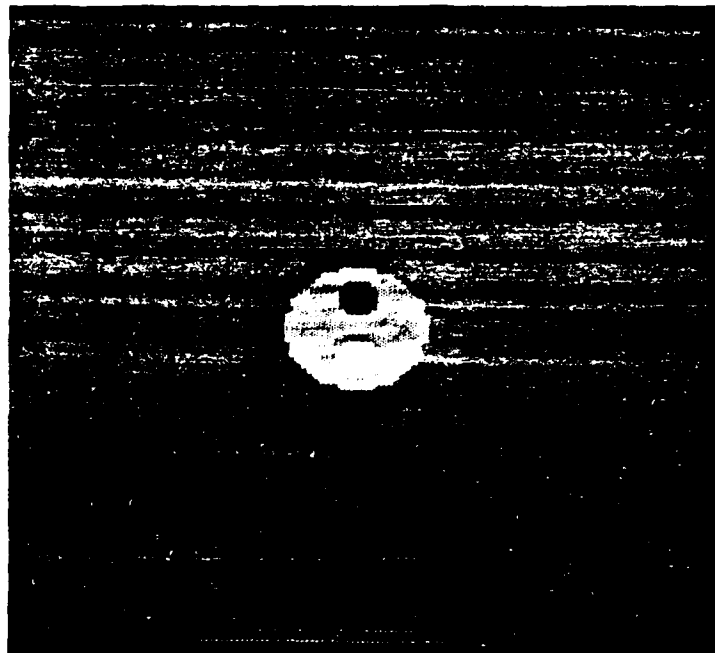Figure 6.8a.   Wiener filter restoration of the image in Figure 6.8a.
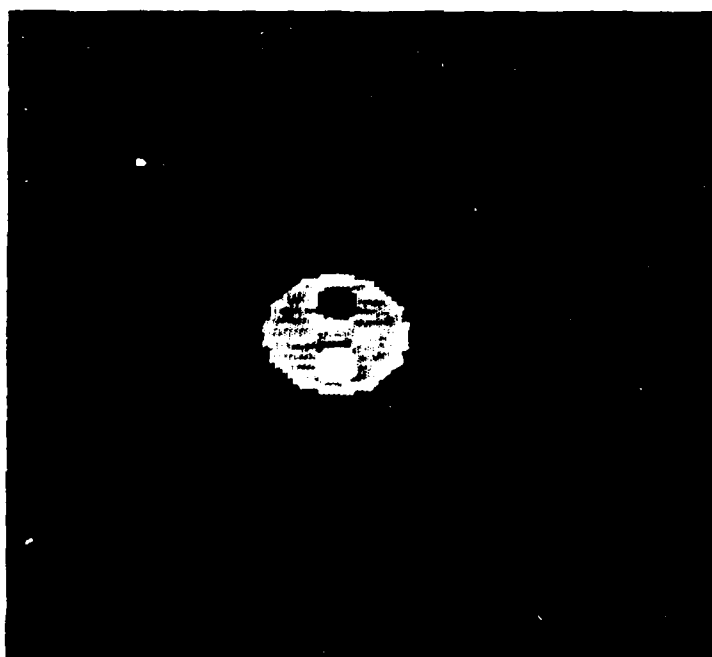
Figure 6.8b.   Wiener filter restoration of the image in Figure 6.8b.

Figure 6.9. Comparison of Wiener filter restorations of a shift-and-add result for the cases of measured psf and a Gaussian least-squares fit to the psf.

a. Wiener filter restoration with measured psf.

b. Wiener filter restoration with a Gaussian least-squares fit to the psf.
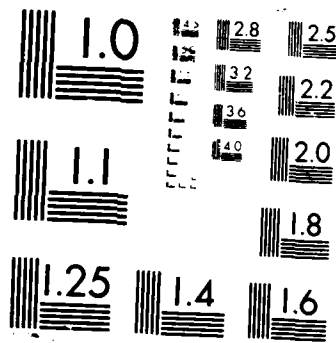
MICROCOPY RESOLUTION TEST CHART
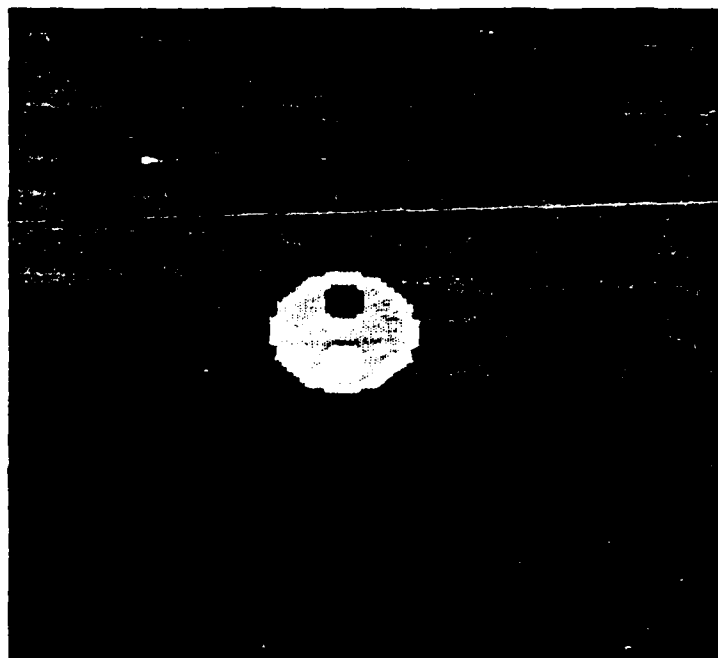
Figure 6.9a. Wiener filter restoration with measured psf.
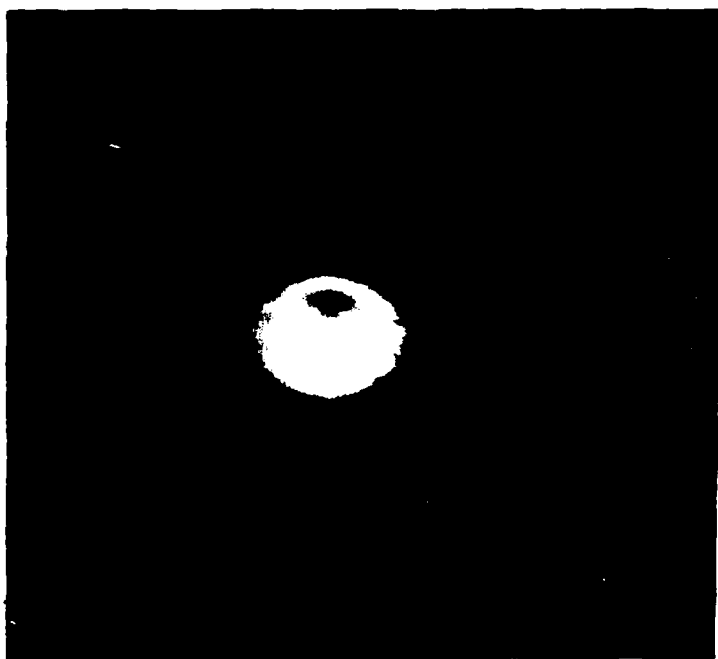
Figure 6.9b. Wiener filter restoration with a Gaussian least-squares
fit to the psf.

fact that only twenty images were processed by shift-and-add. As noted in section 6.2, this Gaussian approximation should improve as the number of frames processed increases. Even with this remaining blur, the interior spots are clearly visible, and we have observed some improvement over shift-and-add alone.

In practice, one would not expect such good results as obtained in Figures 6.7 and 6.8 because of noise, lack of information about the exact form of the object power spectrum $\Phi_f(x,y)$, possible "ghosts" in the shift-and-add image and possible problems in obtaining the overall psf; nevertheless, Figures 6.7 through 6.9 indicate that shift-and-add processing plus Wiener filtering shows promise for restoring images degraded by atmospheric turbulence or other random media.

CHAPTER 7

CONCLUSION

In this dissertation, the task was undertaken to analyze the
shift-and-add method in order to provide a better understanding of why
it creates improved versions of images degraded by atmospheric
turbulence.

We first provided the necessary statistical framework and image
model for this analysis along with a brief summary of other imaging
methods employed in the presence of turbulence. Then, in Chapter 4, we
demonstrated that the result of shift-and-add processing of a series of
short exposure images may contain diffraction-limited information, both
in the point source object and in the extended object cases. We also
showed that the probability of error in such processing is relatively
low, although the results were obtained for a noise-free case.
Further, we presented a convergence rate for this algorithm which is
initially fairly rapid, but which slows considerably as the number of
images processed increases. This result suggested the restoration
method applied in Chapter 6: use shift-and-add to average relatively
few images and achieve further improvement by another method.

In support of this analysis, we presented simulation results
which demonstrated the effectiveness of the shift-and-add method,
especially when combined with Wiener filtering. When one considers

94

that these results were obtained by processing only twenty images, the performance of the algorithm becomes even more impressive.

As a further note in support of shift-and-processing, our previous work (Hunt, Morgan and West, 1983) indicated that it is of value in reducing the error in features extracted from turbulent images. The specific feature extraction algorithm considered was invariant moments (Hu, 1962), and in almost all cases we found that the moments of the shift-and-add processed images were lower in error than were the moments of the unprocessed speckle images.

7.1 Suggested Extensions of this Work

The most important theoretical extensions to this work would be to remove the assumptions of isoplanaticity and stationarity, and rederive the point spread function under these new conditions. However, due to the extreme difficulty (or even impossibility) of achieving an analytic result when these assumptions are removed, this might well be a point of diminishing returns.

A further theoretical extension would be to repeat the analysis with the addition of noise; however, in this case one runs into the problem of determining the probability density function of speckles plus noise. The speckles are lognormally distributed, and the lognormal distribution does not possess an analytic characteristic function, so the density function of speckles plus noise would necessarily be an approximation.

It is likely that effort would be better spent extending this algorithm to deal with practical problems facing its use in specific applications, since the major theoretical results have been determined. One such practical problem is that of obtaining a good estimate of $\hat{\phi}_f(u,v)$ for the Wiener filter, and it might well be worthwhile to investigate the dependence of restoration quality on the accuracy of such estimates. Another problem is found in astronomy, where one may face extremely low light levels, say a photon or two per frame. Therefore, in conclusion, we emphasize that such difficulties are likely to be the most fruitful avenues for research on shift-and-add processing.

APPENDIX A

THE LOGNORMAL DISTRIBUTION

In this appendix, we present some of the basic properties of the lognormal distribution, as it appears to be generally unfamiliar, and comment further on the property that the lognormal probability density function is not uniquely determined by its moments. For further information on the lognormal distribution, the reader is referred to Aitchison and Brown (1957) or Johnson and Kotz (1970).

The two-parameter probability density function of a lognormal random variables X takes the form

$$p(x) = \frac{1}{x\sigma\sqrt{2\pi}} \exp\left\{-\frac{[\log x - \mu]^2}{2\sigma^2}\right\}, \quad (x > 0) \qquad (A-1)$$

where log X is normally distributed, log denotes the natural logarithm (base e), μ is the expected value or mean of log X, and σ^2 is the variance of log X. Following Johnson and Kotz (1970), the nth moment of X is

$$m_n' = E[X^n] = e^{n\mu + 1/2n^2\sigma^2} \qquad (A-2)$$

so that the mean is

$$E[X] = m_1' = e^{\mu + 1/2\sigma^2}.$$

The central moments may be computed from the general formula

$$m_n = \frac{m_2^{n/2}}{(w-1)^{n/2}} \sum_{j=0}^{n} (-1)^j \binom{n}{j} w^{1/2(n-j)(n-j-1)} \tag{A-3}$$

where

$$w = e^{\sigma^2}$$

The distribution is unimodal, with

$$mode(X) = e^{\mu - \sigma^2}$$

and

$$median(X) = e^{\mu}.$$

Also, as $\sigma \to 0$, the distribution tends to a normal distribution.

Analogs to the Central Limit Theorem also exist for products of random variables. Just as sums of independent random variables are approximately normally distributed under certain conditions, so under similar conditions are products of independent random variables approximately lognormally distributed. For more specific statement of the lognormal Central Limit Theorem and for extensive results on estimation of parameters for a lognormally distributed population or data set, see Aitchison and Brown (1957).

We now address the property that the lognormal distribution is not uniquely determined by its moments, a property of interest in Chapter 2. In the usual case (Papoulis, 1965), if we know the moments m_n of a random variable, we may determine its characteristic function $\phi(u)$ by the following expression.

$$\phi(u) = 1 + ium_1 + \ldots + \frac{(iu)^n}{n!} m_n + \ldots$$

where i denotes the square root of -1. Inverse Fourier transforming then yields the probability density function. However, Heyde (1963) and later Barakat (1976) have proved that this result is not unique for the lognormal distribution. Heyde (1963) has presented another distribution with density function

$$f(x) = \frac{1}{\sigma x \sqrt{2\pi}} \exp \left\{ - \frac{[\log x - \mu]^2}{2\sigma^2} \right\} \left\{ 1 + \epsilon \sin\left[\frac{2\pi k}{\sigma^2}(\log x - \mu)\right] \right\} , \quad x > 0$$

$$(A-4)$$

where $0 < \epsilon < 1$ and k is a positive integer, which he claims has the same moments as the lognormal random variable X with the density function p(x) of Equation (A-1).

To see this result, we consider the difference in moments of the two distributions

$$I = \int_0^\infty x^n p(x)dx - \int_0^\infty x^n f(x)dx \quad n = 0, 1, 2, \ldots$$

$$= \frac{-\epsilon}{\sigma\sqrt{2\pi}} \int_0^\infty x^{n-1} \exp\left\{ - \frac{[\log x - \mu]^2}{2\sigma^2} \right\} \sin\left[\frac{2\pi k}{\sigma^2}(\log x - \mu)\right] dx.$$

We make the change of variable

$$y = \frac{\log x - \mu}{\sigma}$$

giving

$$I = \frac{-\varepsilon e^{n\mu}}{\sqrt{2\pi}} \int_{-\infty}^{\infty} e^{-1/2 y^2 + n\sigma y} \sin[\frac{2\pi k}{\sigma} y] dy$$

$$= \frac{-\varepsilon e^{n\mu + 1/2 n^2 \sigma^2}}{\sqrt{2\pi}} \quad e^{-1/2(y-n\sigma)^2} \sin[\frac{2\pi k}{\sigma} y] dy$$

$$= 0$$

because the integrand is odd. Therefore both distributions (where actually f(x) determines a whole family of distributions by varying the parameters ε and k) have the same moments.

APPENDIX B

EVALUATION OF INTEGRALS

In this appendix, we evaluate two integrals from Chapter 4 which arise in the determination of the overall point spread function of the shift-and-add process.

We will first evaluate the following integral

$$E[I_2|I_2] = \int_0^\infty I_2 p(I_2|I_1)dI_2$$

$$= \frac{1}{\sigma_2 \sqrt{2\pi(1-\rho^2)}} \int_0^\infty dI_2 \exp\left\{\frac{-\left[\left(\frac{\log I_1-\mu_1}{\sigma_1}\right)^2 \rho^2 + \left(\frac{\log I_2-\mu_2}{\sigma_2}\right)^2 - 2\rho\left(\frac{\log I_1-\mu_1}{\sigma_1}\right)\left(\frac{\log I_2-\mu_2}{\sigma_2}\right)\right]}{2(1-\rho^2)}\right\}$$

$$(B-1)$$

Expanding the exponent in Equation (B-1) gives

$$\rho^2\left(\frac{\log I_1-\mu_1}{\sigma_1}\right)^2 + \left(\frac{\log I_2-\mu_2}{\sigma_2}\right)^2 - 2\rho\left(\frac{\log I_1-\mu_1}{\sigma_1}\right)\left(\frac{\log I_2-\mu_2}{\sigma_2}\right)$$

$$= \left[\rho^2\left(\frac{\log I_1-\mu_1}{\sigma_1}\right)^2 + 2\rho\frac{\mu_2}{\sigma_2}\left(\frac{\log I_1-\mu_1}{\sigma_1}\right) + \frac{\mu_2^2}{\sigma_2^2}\right]$$

$$+ \left[\frac{1}{\sigma_2^2}(\log I_2)^2 - (2\mu_2/\sigma_2 + \frac{2\rho}{\sigma_1\sigma_2}(\log I_1-\mu_1))\log I_2\right]$$

101

where we have collected terms according to their dependence on $\log I_2$. Thus Equation (B-1) becomes

$$E[I_2|I_1] = \frac{1}{\sigma_2 \sqrt{2\pi(1-\rho^2)}} \exp\left\{\frac{-\left[\rho^2\left(\frac{\log I_1 - \mu_1}{\sigma_1}\right)^2 + 2\rho\frac{\mu_2}{\sigma_2}\left(\frac{\log I_1 - \mu_1}{\sigma_1}\right) + \mu_2^2 \sigma_2^2\right]}{2(1-\rho^2)}\right\}$$

$$X \int_0^\infty \exp\left\{\frac{-\left[\frac{1}{\sigma_2^2}(\log I_2)^2 - 2(\mu_2/\sigma_2^2 + \frac{\rho}{\sigma_1\sigma_2}(\log I_1 - \mu_1))\log I_2\right]}{2(1-\rho^2)}\right\} dI_2 .$$

$$(B-2)$$

We now consider the integral portion only of this expression and let

$$INT = \int_0^\infty \exp\left\{\frac{-\left[\frac{1}{\sigma_2^2}(\log I_2)^2 - 2(\mu_2/\sigma_2^2 + \frac{\rho}{\sigma_1\sigma_2}(\log I_1 - \mu_1))\log I_2\right]}{2(1-\rho^2)}\right\} dI_2 .$$

$$(B-3)$$

To evaluate this integral, we make the following change of variable in Equation (B-3):

$$t = \log I_2$$
$$dI_2 = e^t dt$$

Then

$$INT = \int_\infty^\infty \exp\left\{\frac{-t^2}{2\sigma_2^2(1-\rho^2)} + \frac{\left[\mu_2/\sigma_2 + \frac{\rho(\log I_1 - \mu_1)}{\sigma_1\sigma_2} + (1-\rho^2)\right]}{(1-\rho^2)} t\right\} dt$$

$$(B-4)$$

which we evaluate by using Gradshteyn and Ryzhik (1980, p. 307), where it is stated that

$$\exp[-p^2 x^2 \pm qx]dx = \exp[\frac{q^2}{4p^2}]\frac{\sqrt{\pi}}{p}, \qquad p > 0.$$

From Equation (B-4), we make the correspondences

$$p^2 = \frac{1}{2\sigma_2^2(1-\rho^2)}$$

$$q = \frac{\mu_2/\sigma_2 \; \rho\left(\dfrac{\log I_1 - \mu_1}{\sigma_1 \sigma_2}\right) + (1-\rho^2)}{(1-\rho^2)}$$

so that

$$1/p = \sigma_2\sqrt{2(1-\rho^2)}$$

$$\frac{q^2}{4p^2} = \frac{\dfrac{\mu_2^2}{\sigma_2^2} + 2\rho\dfrac{\mu_2}{\sigma_2}\left(\dfrac{\log I_1 - \mu_1}{\sigma_1}\right) 2\mu_2(1-\rho^2) + \rho^2\left(\dfrac{\log I_1 - \mu_1}{\sigma_1^2}\right) + 2\sigma_2\rho(1-\rho^2)\left(\dfrac{\log I_1 - \mu_1}{\sigma_1}\right) + \sigma_2^2(1-\rho^2)}{2(1-\rho^2)}$$

Thus we have

$$INT = \exp\left\{\frac{\dfrac{\mu_2^2}{\sigma_2^2} + 2\rho\dfrac{\mu_2}{\sigma_2}\left(\dfrac{\log I_1 - \mu_1}{\sigma_1}\right) 2\mu_2(1-\rho^2) + \rho^2\left(\dfrac{\log I_1 - \mu_1}{\sigma_1^2}\right) + 2\sigma_2\rho(1-\rho^2)\left(\dfrac{\log I_1 - \mu_1}{\sigma_1}\right) + \sigma_2^2(1-\rho^2)}{2(1-\rho^2)}\right\}$$

$$\times \; \sigma_2\sqrt{2\pi(1-\rho^2)}$$

and substituting this expression into Equation (B-2), we obtain

$$E[I_2 | I_1] = \exp\{\mu_2 + (\sigma_2/\sigma_1)\rho\log I_1 - (\sigma_2/\sigma_1)\rho\mu_1 + \sigma_2^2(1-\rho^2)/2\}$$

$$= I_1^{\rho\sigma_2/\sigma_1} \exp\{\mu_2 - \rho\mu_1\sigma_2/\sigma_1 - \sigma_2^2(1-\rho^2)/2\} .$$

We now evaluate the integral expression $E[I_2 I_1]$, which is needed in order to determine the correlation coefficient of I_1 and I_2. This expectation takes the form

$$E[I_2 I_1] = \int_0^\infty \int_0^\infty I_2 I_1 p(I_2, I_1) dI_2 dI_1$$

$$\cdot \frac{1}{2\pi\sigma_1\sigma_2\sqrt{1-\rho^2}} \int_0^\infty \int_0^\infty \exp\left\{-\frac{\left[\left(\frac{\log I_1-\mu_1}{\sigma_1}\right)^2 + \left(\frac{\log I_2-\mu_2}{\sigma_2}\right)^2 - 2\rho\left(\frac{\log I_1-\mu_1}{\sigma_1}\right)\left(\frac{\log I_2-\mu_2}{\sigma_2}\right)\right]}{2(1-\rho^2)}\right\}$$

$$(B-5)$$

We make the changes of variables

$$s = \frac{\log I_1-\mu_1}{\sigma_1}$$

and

$$t = \frac{\log I_2-\mu_2}{\sigma_2}$$

and obtain

$$E[I_2 I_1] = \frac{e^{\mu_1+\mu_2}}{2\pi\sqrt{1-\rho^2}} \int_{-\infty}^\infty \int_{-\infty}^\infty e^{\sigma_1 s+\sigma_2 t} \exp\left\{\frac{-[s^2+t^2-2\rho st]}{2(1-\rho^2)}\right\} dtds .$$

$$(B-6)$$

First we evaluate the t integral

$$I_t = \int_{-\infty}^{\infty} \exp\left\{\frac{-1}{2(1-\rho^2)}\, t^2 + \frac{\rho s + \sigma_2(1-\rho^2)}{(1-\rho^2)}\, t\right\} dt$$

by using the same formula from Gradshteyn and Ryzhik (1980)

$$\exp[-p^2 x^2 \pm qx]dx = \exp\frac{q^2}{4p^2}\, \frac{\sqrt{\pi}}{p}, \quad p > 0$$

In this case, we make the correspondences

$$p^2 = \frac{1}{2(1-\rho^2)}$$

$$q = \sigma^2 + \frac{\rho s}{(1-\rho^2)}$$

so that

$$\frac{\sqrt{\pi}}{p} = \sqrt{2\pi(1-\rho^2)}$$

$$\frac{q^2}{4p^2} = \frac{\sigma_2^2(1-\rho^2)}{2} + \sigma_2 \rho s + \frac{\rho^2 s^2}{2(1-\rho^2)},$$

Then

$$I_t = \sqrt{2\pi(1-\rho^2)}\, \exp\left\{\frac{\sigma_2^2(1-\rho^2)}{2} + \sigma_2 \rho s + \frac{\rho^2}{2(1-\rho^2)}\, s^2\right\}.$$

Substituting in Equation (B-6) yields

$$E[I_2 I_1] = \frac{\exp\{\mu_1 + \mu_2 + \sigma_2^2(1-\rho^2)/2\}}{\sqrt{2\pi}} \int_{-\infty}^{\infty} \exp\left\{\frac{-s^2}{2} + (\sigma_1 + \rho\sigma_2)s \quad ds\right\}$$

$$= \langle I_2 \rangle\, \frac{\exp\{\mu_1 - \rho^2\sigma_2^2/2\}}{\sqrt{2\pi}} \int_{-\infty}^{\infty} \exp\left\{-\frac{s^2}{2} + (\sigma_1 + \rho\sigma_2)s\right\} ds \qquad (B-7)$$

which is evaluated as was the t integral with

$$p^2 = 1/2$$

$$q = \sigma_1 + \rho\sigma_2$$

which implies that

$$\sqrt{\pi}/p = \sqrt{2\pi}$$

$$q^2/(4p^2) = \sigma_1^2/2 + \rho\sigma_1\sigma_2 + \rho^2\sigma_2^2/2$$

Then substituting in Equation (B-7) yields the desired result

$$E[I_2 I_1] = \langle I_2 \rangle \langle I_1 \rangle e^{\rho\sigma_1\sigma_2}.$$

LIST OF REFERENCES

Abramowitz, M., and I. Stegun, eds. (1970), <u>Handbook of Mathematical Functions</u>, Dover, New York.

Aime, C., S. Kadiri, G. Ricort, C. Roddier and J. Vernin (1979), "Measurements of Stellar Speckle Interferometry Lens-Atmosphere Modulation Transfer Function," Optica Acta, vol. 26, pp. 275-581.

Aitchison, J. and J. A. C. Brown (1957), <u>The Lognormal Distribution</u>, Cambridge University Press, London.

Andrews, H. C. and B. R. Hunt (1977), <u>Digital Image Restoration</u>, Prentice-Hall, Englewood Cliffs, New Jersey.

Apelblat, A. (1983), <u>Table of Definite and Infinite Integrals</u>, Elsevier Scientific Publishing Co., New York.

Bagnuolo, W. G. Jr. (1982), "The Application of Bates' Algorithm to Binary Stars," Monthly Notices of the Royal Astronomical Society, vol. 200, pp. 1113-1122.

Bagnuolo, W. G., Jr. (1984), "Effect of Nonisoplanaticity on the Shift-and-Add Algorithm," Optics Letters, vol. 9, pp 65-67.

Barakat, R. (1976), "Sums of Independent Lognormally Distributed Random Variables," JOSA, vol. 66, pp. 211-216.

Bates, R. H. T. (1982), "Astronomical Speckle Imaging," Physics Reports, vol. 90, pp. 203-297.

Bates, R. H. T. and F. M. Cady (1980), "Towards True Imaging by Wide-band Speckle Interferometry," Optics Communications, vol. 32, pp. 365-369.

Bates, R. H. T., P. T. Gough and P. J. Napier (1973), "Speckle Interferometry Gives Holograms of Multiple Star Systems," Astronomy and Astrophysics, vol. 22, pp. 319-320.

Bates, R. H. T. and B. S. Robinson (1982), "A Stochastical Imaging Procedure," in <u>Acoustical Imaging</u>, vol. 12, E. A. Ash and C. R. Hill, eds., Plenum Press, New York and London.

107

Cady, F. M. and R. H. T. Bates (1980), "Speckle Processing Gives Diffraction-Limited True Images of Severely Aberrated Instruments," Optics Letters, vol. 5, pp. 438-440.

Chelli, A., P. Lena, C. Roddier, F. Roddier and F. Sibille (1979), "Modulation Transfer Function for Infra-red Stellar Speckle Interferometry: Evidence for a Log-normal Statistic," Optica Acta, vol. 26, pp. 583-595.

Cramér, H. (1951), Mathematical Methods of Statistics, Princeton University Press, Princeton.

Dainty, J. C. (1973), "Diffraction-Limited Imaging of Stellar Objects Using Telescopes of Low Optical Quality," Optics Comm., vol. 7, pp. 129-134.

Dainty, J. C. (1975), "Stellar Speckle Interferometry," ch. 7 of Laser Speckle and Related Phenomena, J. C. Dainty, ed., Topics in Applied Physics, vol. 9, Springer-Verlag, Berlin.

Dainty, J. C. (1984), "Stellar Speckle Interferometry," ch. 7 of Laser Speckle and Related Phenomena, second enlarged edition, J. C. Dainty, ed., Topics in Applied Physics, vol. 9, Springer-Verlag, Berlin.

deWolf, D. A. (1969), "Are Strong Irradiance Fluctuations Log Normal or Rayleigh Distributed?", JOSA, vol. 59, pp. 1455-1460.

Fante, R. L. (1975), "Electromagnetic Beam Propagation in Turbulent Media," Proc. IEEE, vol. 63, pp. 1669-1691.

Fienup, J. R. (1978), "Reconstruction of an Object from the Modulus of Its Fourier Transform," Optics Letters, vol. 3, pp. 27-29.

Fienup, J. R. (1979), "Space Object Imaging Through the Turbulent Atmosphere," Optical Engineering, vol. 18, pp. 529-534.

Fried, D. L. (1966), "Optical Resolution Through a Randomly Inhomogenous Medium for Very Long and Very Short Exposures," JOSA, vol. 56, pp. 1372-1379.

Gerchberg, R. W. and W. O. Saxton (1972), "A Practical Algorithm for the Determination of Phase from Image and Diffraction Plane Pictures," Optik, vol. 35, pp. 237-246.

Gezarie, D. Y., A. Labeyrie and R. V. Stachnik (1972), "Speckle Interferometry: Diffraction-Limited Measurements of Nine Stars with the 200-Inch Telescope," The Astrophysical Journal, vol. 173, pp. L1-L5.

Goodman, J. W. (1984), "Statistical Properties of Laser Speckle Patterns," ch. 2 of Laser Speckle and Related Phenomena, second enlarged edition, J. C. Dainty, ed., vol. 9 of Topics in Applied Physics, Springer-Verlag, Berlin.

Gough, P. T. and R. H. T. Bates (1974), "Speckle Holography," Optica Acta, vol. 21, pp. 243-254.

Gradshteyn, I. S. and I. M. Ryzhik (1980), Table of Integrals, Series and Products, Academic Press, New York.

Heyde, C. C. (1963), "On a Property of the Lognormal Distribution," Journal of the Royal Statistical Society, series B, vol. 25, pp. 392-393.

Hoeffding, W. and H. Robbins (1948), "The Central Limit Theorem for Dependent Random Variables," Duke Mathematical Journal, vol. 15, pp. 773-780.

Hu, M. K. (1962), "Visual Pattern Recognition by Moment Invariants," IRE Trans. Information Theory, vol. IT-8, pp. 179-187.

Hufnagel, R. E. and N. R. Stanley (1964), "Modulation Transfer Function Associated with Image Transmission Through Turbulent Media," JOSA, vol. 54, pp. 52-61.

Hunt, B. R., W. R. Fright and R. H. T. Bates (1983), "Analysis of the Shift-and-Add Method for Imaging Through Turbulent Media," JOSA, vol. 73, pp. 456-465.

Hunt, B. R., K. Morgan and K. West (1983), "Pattern Recognition of Images in Atmospheric Turbulence," Technical Report DIAL-83-006, Engineering Experiment Station, University of Arizona, Tucson.

Johnson, N. L. and S. Kotz (1970), Continuous Univariate Distributions-1, Houghton Mifflin Company, Boston, Massachusetts.

Knox, K. T. and B. J. Thompson (1974), "Recovery of Images from Atmospherically Degraded Short-Exposure Photographs," The Astrophysical Journal, vol. 193, pp. L45-L48.

Korff, D. (1973), "Analysis of a Method for Obtaining Near-Diffraction-Limited Information in the Presence of Atmospheric Turbulence," JOSA, vol. 63, pp. 971-980.

Labeyrie, A. (1970), "Attainment of Diffraction Limited Resolution in Large Telescopes by Fourier Analyzing Speckle Patterns in Star Images," Astronomy and Astrophysics, vol. 6, pp. 85-87.

Lawrence, R. S. (1976), "A Review of the Optical Effects of the Clear
        Turbulent Atmosphere," Proc. SPIE, Vol. 75, pp. 2-7.

Lawrence, R. S. and J. W. Strohbehn (1970), "A Survey of Clear-Air
        Propagation Effects Relevant to Optical Communications," Proc.
        IEEE, vol. 58, pp. 1523-1545.

Lee, M. H., J. F. Holmes and J. R. Kerr (1976), "Statistics of Speckle
        Propagation Through the Turbulent Atmosphere," JOSA, vol. 66,
        pp. 1164-1172.

Liu, C. Y. C. and A. W. Lohmann (1973), "High Resolution Image Forma-
        tion Through the Turbulent Atmosphere," Optics Communications,
        vol. 8, pp. 372-376.

Loève, M. (1950), "Fundamental Limit Theorems of Probability Theory,"
        The Annals of Mathematical Statistics, vol. 21, pp. 321-338.

Lynds, C. R., S. P. Worden and J. W. Harvey (1976), "Digital Image
        Reconstruction Applied to Alpha Orionis," The Astrophysical
        Journal, vol. 207, pp. 174-180.

McGlamery, B. L. (1976), "Computer Simulation Studies of Compensation
        of Turbulence Degraded Images," Proc. SPIE, vol. 74, pp.
        225-233.

Mitchell, R. L. (1968), "Permanence of the Lognormal Distribution,"
        JOSA, vol. 58, pp. 1267-1272.

Ochs, G. R. and R. S. Lawrence (1969), "Saturation of Laser-Beam Scin-
        tillation under Conditions of Strong Atmospheric Turbulence,"
        JOSA, vol. 59, pp. 226-227.

Oppenheim, A. V. and J. S. Lim (1974), "The Importance of Phase in
        Signals," Proc. IEEE, vol. 69, pp. 529-541.

Papoulis, A. (1965), Probability, Random Variables and Stochastic Pro-
        cesses, McGraw-Hill Book Company, New York.

Roddier, F. (1981), "The Effects of Atmospheric Turbulence in Optical
        Astronomy," ch. 5 of Progress in Optics, vol. 19, E. Wolf, ed.,
        North-Holland Publishing Company, Amsterdam.

Serfling, R. J. (1968), "Contributions to Central Limit Theory for
        Dependent Variables," The Annals of Mathematical Statistics,
        vol. 39, pp. 1158-1175.

Strohbehn, J. W. (1968), "Line-of-Sight Wave Propagation Through the
        Turbulent Atmosphere," Proc. IEEE, vol. 156, pp. 1301-1318.

Strohbehn, J. W. (1971), "Optical Propagation Through the Turbulent
    Atmosphere," ch. 3, in Progress in Optics, vol. 9, E. Wolf,
    ed., North-Holland Publishing Company, Amsterdam.

Tatarski, V. I. (1961), Wave Propagation in a Turbulent Medium, trans-
    lated from the Russian by R. A. Silverman, McGraw-Hill Book
    Company, New York.

Tatian, B. (1965), "Method for Obtaining the Transfer Function from the
    Edge Response Function," JOSA, vol. 55, pp. 1014-1019.

Tescher, A. G. and H. C. Andrews (1972), "Data Compression and Enhance-
    ment of Sampled Images," Applied Optics, vol. 11, pp. 919-925.

Weigelt, G. P. (1977), "Modified Astronomical Speckle Interferometry
    'Speckle Masking'," Optics Comm., vol. 21, pp. 55-59.

Weigelt, G. P. and B. Wirnitze (1983), "Image Reconstruction by the
    Speckle-Masking Method," Optics Letters, vol. 8, pp. 389-391.

Worden, S. P., C. R. Lynds and J. W. Harvey (1976), "Reconstructed
    Images of Alpha Orionis Using Stellar Speckle Interferometry,"
    JOSA, vol. 66, pp. 1243-1246.

END

DATE
FILMED

DEC.
1987